UNIVERSITY OF OKLAHOMA

GRADUATE COLLEGE

EXAMINING THE VERTICAL STRUCTURE OF HURRICANE LAURA (2020) USING AZIMUTHAL-MEAN VERTICAL PROFILES AND AN EOF ANALYSIS

A THESIS

SUBMITTED TO THE GRADUATE FACULTY

in partial fulfillment of the requirements for the

Degree of

MASTER OF SCIENCE

By

EMILY BLUMENAUER
Norman, Oklahoma
2023

EXAMINING THE VERTICAL STRUCTURE OF HURRICANE LAURA (2020) USING AZIMUTHAL-MEAN VERTICAL PROFILES AND AN EOF ANALYSIS

A THESIS APPROVED FOR THE
SCHOOL OF METEOROLOGY

BY THE COMMITTEE CONSISTING OF

Dr. Michael Biggerstaff (Chair)

Dr. David Bodine

Dr. Benjamin Schenkel

Dr. Addison Alford

Acknowledgments

I would like to thank my parents, John and Sallie, for always supporting me—even if that means helping me move halfway across the country during a pandemic. I would also like to thank my siblings, Rob and Meg, for being my best friends and for always being a source of laughter in my life. And thank you to my boyfriend, Jonah Pehl, for being a constant source of encouragement and for the sanity checks when I forget how meteorology works.

I want to thank my advisor, Dr. Mike Biggerstaff, for this research opportunity and for the field work experience. I would also like to thank Dr. Addison Alford for answering my countless questions with enthusiasm and helping me with the logistics of this project. I am looking forward to continuing my graduate student career with you as my advisor. Thank you to the SMART-R research group for all of your support—especially to Gordon Carrie for fixing everything I've inevitably messed up on my computer. I would also like to thank committee members Dr. David Bodine and Dr. Ben Schenkel for teaching me about radar meteorology (METR 5673 was very helpful) and for always listening to me.

Of course, thank you to the friends I have made during my time at OU. Laura Shedd, Angela Mose, Brandon Cohen, Alec Prosser, and Jason Chiappa—our game nights have always been fun and have been super helpful for getting my mind off of things when life gets stressful. I look forward to all of the memories yet to be made.

I would lastly like to thank the National Institute of Standards and Technology for funding this project with grant 70NANB19H056. Without this funding, none of this work would be possible.

Table of Contents

List Of Tables

List Of Figures

Abstract

The eyewall, inner rainband, and outer rainband regions of tropical cyclones (TCs) have been extensively studied, resulting in numerous conceptual models. While these conceptual models are insightful regarding basic-state kinematics in TCs, they do not detail kinematic variability. Therefore, kinematic perturbations within TCs are not well documented.

One of the University of Oklahoma Shared Mobile Atmospheric Research and Teaching Radars (SRs) was deployed near the Louisiana coast at the time Hurricane Laura made landfall on the Louisiana coast early on 27 August 2020. The SR and the Lake Charles, LA WSR-88D (KLCH) sampled the northeast quadrant of Laura in their collective dual-Doppler lobe from 0000 UTC until KLCH sustained substantial damage at around 0550 UTC. With a 1-km x 1-km x 0.5-km spatial resolution and a temporal resolution of 5-10 minutes, the dual-Doppler analyses (DDAs) captured the eyewall, inner rainband, and outer rainband regions of the hurricane. This dataset therefore provides an opportunity to study the kinematic variability of all three TC regions.

This research serves to validate the conceptual models of previous literature using DDA-mean azimuthal-mean vertical profiles. It also aims to uncover the vertical structure of kinematic variability across the TC using an empirical orthogonal function (EOF) analysis. Additionally, this EOF analysis quantifies the amount of variance explained by each perturbation profile. The results of this research largely agree with the conceptual models, though some features are not supported and others are found to not represent the majority of the variance.

Chapter 1

Introduction

Landfalling tropical cyclones (TCs) and their associated hazards (i.e., flooding from heavy rain and storm surge, strong winds, and tornadoes) pose an undeniable risk to life and property. In fact, TCs are responsible for an average of 50 deaths per year in the United States (Rappaport 2014). In the United States, Hurricane Laura (2020) directly caused 7 fatalities, indirectly caused 34 fatalities, and was responsible for damage totaling $19 billion (Pasch et al. 2020). Thus, documenting the kinematic processes in TCs and ensuring their accurate depiction in conceptual models is critical for mitigating loss and improving forecasts.

Producing conceptual models, several studies have investigated the kinematics of the TC eyewall region (Jorgensen 1984; Marks and Houze 1987; Willoughby 1998), inner rainband region (Didlake and Houze 2013a; Barron et al. 2022), and outer rainband region (Barnes et al. 1983; Powell 1990; Hence and Houze 2008; Didlake and Houze 2009; 2013b). These schematics detail the radial and vertical layout of features such as the reflectivity field, draft locations, and the primary and secondary circulations (Houze 2010). However, because many of these conceptual models are a result of composite analyses, they typically represent basic-state kinematics rather than kinematic variability. Therefore, kinematic perturbations within TCs are not well documented.

The first objective of this research is to validate the conceptual models using observational data from Hurricane Laura. These data are acquired from both the University of Oklahoma Shared Mobile Atmospheric Research and Teaching Radars (SMART-Rs;

Biggerstaff et al. 2005) and the Lake Charles, LA radar of the Weather Surveillance Radars–1988 Doppler (WSR-88D; Crum and Alberty 1993) System. Dual-Doppler analyses (DDAs) are computed from these data and DDA-mean azimuthal-mean vertical profiles are subsequently generated for different variables within Laura's eyewall, inner rainband, and outer rainband region. For the first part of this analysis, to validate the conceptual models, the vertical profiles and conceptual models are compared. This comparison will show large agreement for the eyewall region, minimal agreement for the inner rainband region, and moderate agreement for the outer rainband region.

The second objective is to identify kinematic variability in each region of Laura and to quantify its corresponding variance explained. This is accomplished by performing an EOF analysis on the anomaly data for each variable in each TC region, which outputs peturbation structures and assigns percentages according to the total variance they represent. In addition to being identified, the perturbations are compared to the conceptual models in an effort to verify features that are otherwise undetected in the azimuthal-mean vertical profiles. The results will show that some of the features not resolved by the azimuthal-mean vertical profiles appear in the EOF analyses as perturbations, while others remain absent.

The following paragraph outlines the organization of this thesis. Chapter 2 describes background information relating to the general layout of TCs, TC conceptual models, and EOF analyses. Chapter 3 provides a general overview of Hurricane Laura, information about the datasets being used, and the methodology for this work. Chapters 4 and 5 discuss the results from the DDA-mean azimuthal-mean vertical profiles and the EOF analysis. Lastly, Chapter 6 provides a discussion of the results, conclusions, and recommendations for future work.

Chapter 2

Background

2.1 Tropical Cyclone Formation and Structure

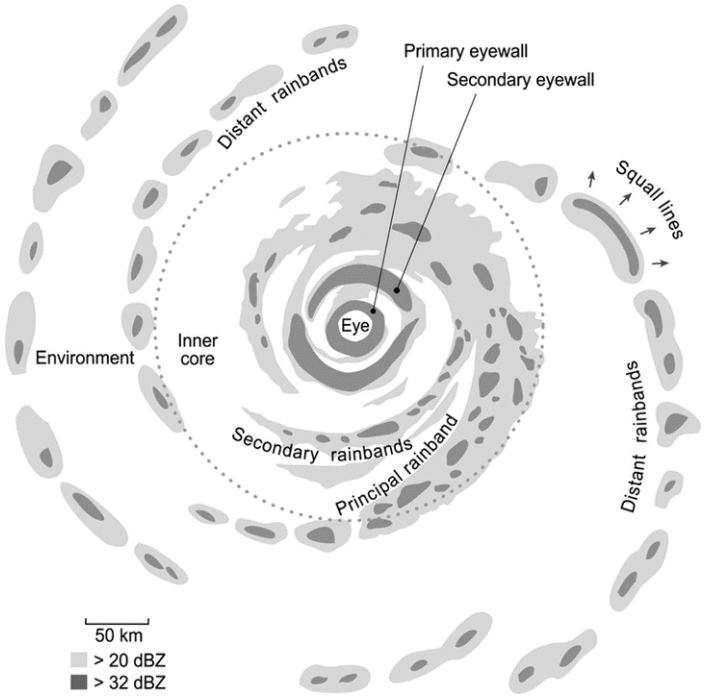

Figure 1: Figure 30 from Houze (2010), adapted from Willoughby (1988). General hurricane plan view depicting the eye, eyewalls, secondary rainbands, principal rainband, and distant rainbands.

From an environmental perspective, TCs have been observed to form where there is >26°C sea surface temperature (e.g., Palmen 1948), minimal vertical wind shear (e.g., McBride and Zehr 1981), and sufficient low-to-midlevel moisture (e.g., Bister and Emanuel 1997). Additionally, the Coriolis force should be nonzero and there should

be sufficient low-level relative vorticity (Gray 1968). Under these conditions, tropical systems can form from varying levels of synoptic influence (e.g., troughs) and varying levels of low-level baroclinity (e.g., isentropic ascent) (McTaggart-Cowan et al. 2008). As a tropical depression, various stages of mesoscale convective vortices (MCVs) and vortical hot towers (VHTs) circulate around a broader area of low pressure (Houze 2010). Eventually, a recognizable TC structure forms after localized vorticity maxima associated with VHTs become axisymmetrized, thus producing a radius of maximum wind (RMW) (Montgomery et al. 2006).

Willoughby (1988) conceptualized the general mature hurricane layout and Houze (2010) later expanded the layout, depicted in Figure 1. From this schematic, the hurricane is divided into the eye, primary and secondary eyewalls, secondary rainbands, the principal rainband, and the distant rainbands. The eyewalls and rainbands of TCs have been extensively studied to document their mean vertical structure, identify important processes, and determine the impact of those processes on the overall storm. Several observational studies have created conceptual models detailing the general kinematic structures within TCs. While these conceptual models were not intended to represent all processes within hurricanes, they can be used to gain a general idea of hurricane structure.

2.1.1 Eyewall

Being a low-pressure system, TCs have a primary circulation of cyclonic flow around the eye. A secondary circulation, consisting of low-level inflow that turns upward and eventually outward at upper levels, exists to keep the primary circulation in gradient wind balance (Houze 2010). Houze (2010) emphasized the outward slanted nature of the TC eyewall, which differs from conventional convective clouds. He noted that

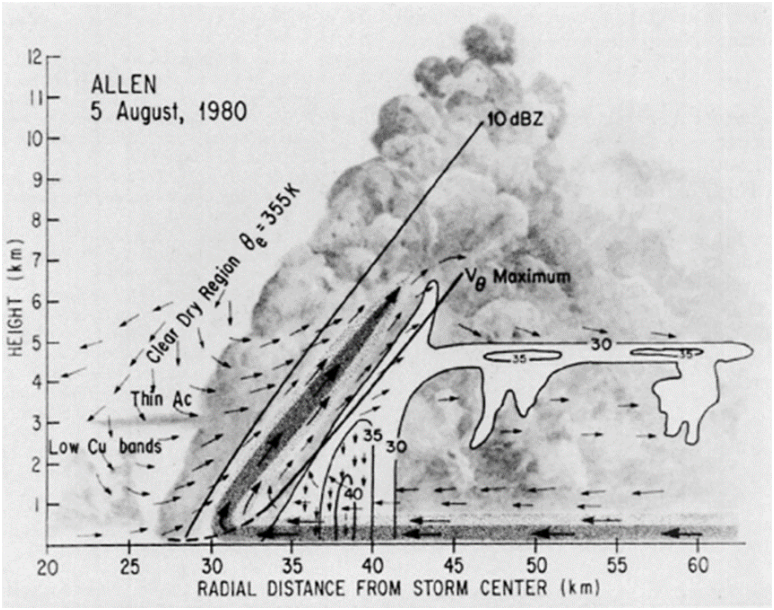

Figure 2: Figure 19 from Jorgensen (1984), conceptualizing the eyewall of Hurricane Allen (1980). Notable features include an outwardly slanted RMW, a secondary circulation, and a stratiform region outside of the eyewall.

while convective clouds typically form via buoyantly unstable vertical motion, the eyewall typically forms via slantwise convection and later achieves mostly conditional symmetric neutrality. As the low-level inflow travels across the ocean surface, it intakes sensible and latent heat and increases θ_e, which leads to instability (Emanuel 1986; Montgomery et al. 2006; Houze 2010). This instability, paired with outwardly acting inertia, causes the slanted structure.

Jorgensen (1984), Marks and Houze (1987), and Willoughby (1998) created TC eyewall schematics which are detailed in Figures 2–4, respectively. All figures detail the secondary circulation. Other notable features include an outwardly tilted reflectivity tower, a stratiform region radially outside of the convective core, mesoscale vertical motion atop and beneath the bright band, downdrafts beneath the updraft from evaporation of hydrometeors, and the trajectories of advected hydrometeors. Marks and Houze (1987) and Houze et al. (1992) explained the hydrometeor advection trajectories

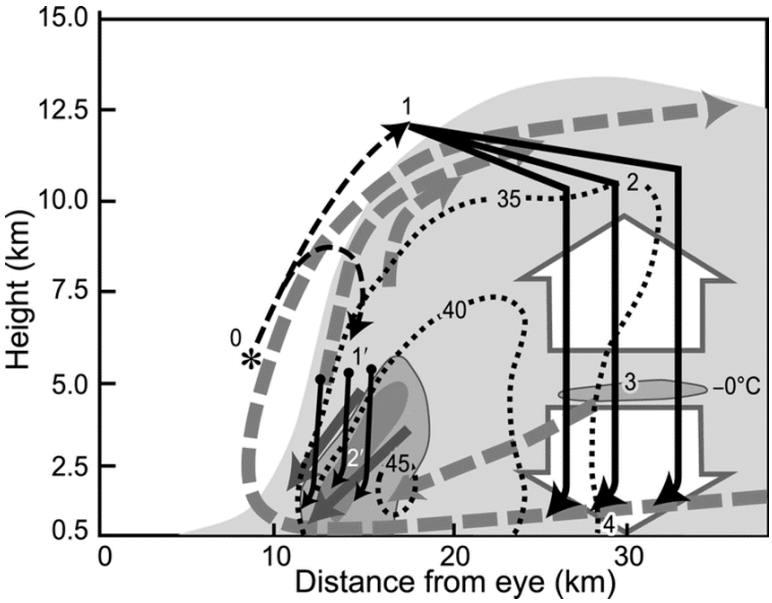

Figure 3: Figure 25 from Houze (2010) adapted from Marks and Houze (1987). Notable features include an outwardly slanted RMW (dotted contours), a secondary circulation (dashed lines), and a stratiform region outside of the eyewall. Additionally, mesoscale and convective-scale processes are included.

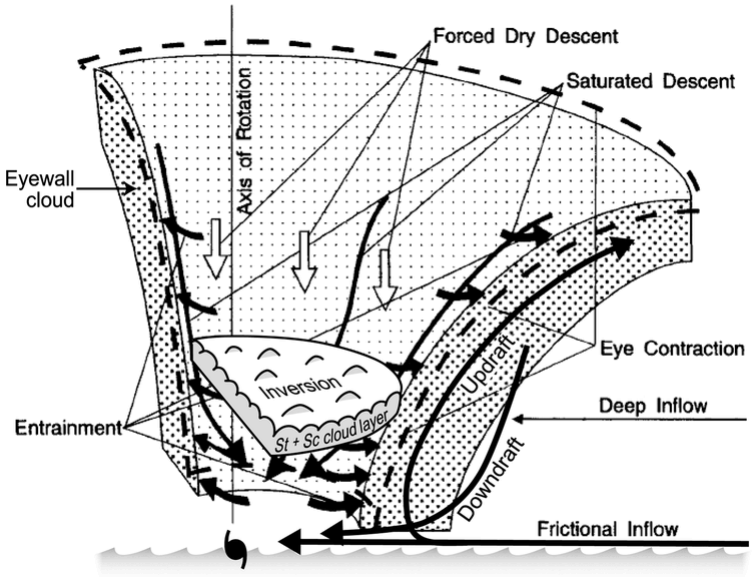

Figure 4: Figure 9 from Houze (2010) adapted from Willoughby (1998). Depicts the eyewall secondary circulation (solid line), a convective downdraft (labeled, solid line), eye subsidence (white arrows), and a low-level cloud layer.

depict size sorting, as larger hydrometeors (i.e., graupel) were observed to fall within the eyewall and smaller hydrometeors (i.e., aggregates) were observed to fall in the outer stratiform region.

2.1.2 Inner Rainbands

Inner rainbands are located outside of the eyewall within the inner core. Several studies have identified a connection between inner rainbands and vortex Rossby waves (VRWs). Hurricane-scale Rossby-like waves were first suggested by MacDonald (1968) as he compared TC eddies to planetary-scale Rossby waves. He confirmed the existence of asymmetries within hurricanes and suggested they have a role in the transport of angular momentum. Using f-plane shallow water equations, Guinn and Schubert (1993) hypothesized that, in response to potential vorticity (PV) asymmetries, TCs undergo processes like wave breaking and merging in an effort to restore the symmetrical PV structure. As a result of this restoration process, spiral bands with enhanced PV develop outside of the TC center. These previously observed spiral bands were later named VRWs by Montgomery and Kallenbach (1997) and were described as propagating radially outward, propagating azimuthally slower than the mean tangential flow, and undergoing shearing by the TC's radially varying rotation. Using a Wenzel-Kramers-Brillouin (WKB) analysis, Montgomery and Kallenbach (1997) derived a dispersion relation for VRWs in TCs and concluded that simulated waves agreed with this relation, as they were shown to be dispersive and controlled by the vorticity gradient.

Several modeling studies support VRW theory in TCs (e.g., Chen and Yau 2001a; Wang 2002a; Chen and Yau 2003; Li and Wang 2012b) and others confirm PV and angular momentum transport by VRWs (e.g., Chen and Yau 2001a; Wang 2002b). Moon and Nolan (2015), however, disagreed with VRW theory because they found the

inner rainbands were correlated with PV anomaly couplets, rather than just positive PV anomalies. Also, their radial movement was not associated with the anticipated PV features based on VRW theory. They provided a counter theory, stating that inner rainbands are essentially convection that has been sheared into spirals. The outward movement of the rainbands was explained to be from low-level outflow associated with the secondary circulation resulting from vertical wind shear. Despite this counter theory, several observational studies noted spiral bands of reflectivity that were associated with wavenumber 2 asymmetries and exhibited other VRW characteristics (e.g., Reasor et al. 2000; Corbosiero et al. 2006; Guimond et al. 2020). Therefore, VRW theory has been observationally supported.

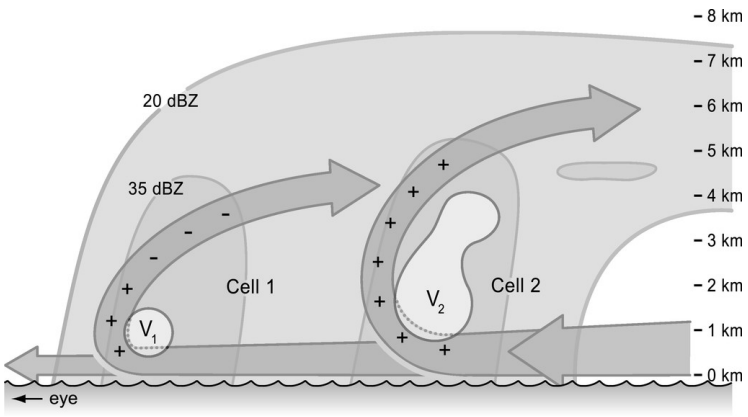

Figure 5: Figure 18 from Didlake and Houze (2013a), depicting convective cells at varying radii. Compared to cells at larger radii, cells at smaller radii are shown to have weaker and shallower vertical motion, a weaker tangential jet, and shallower radial inflow.

Didlake and Houze (2013a) identified differences in the vertical structure between the inner and outer rainband regions. Namely, shown in Figure 5, the inner rainband has a shallower secondary circulation (i.e., up to 4-5 km) with a weak updraft, shallower low-level inflow, and a weaker tangential jet. The weaker features have been suggested to be from less convective available potential energy (CAPE) at smaller radii (e.g.,

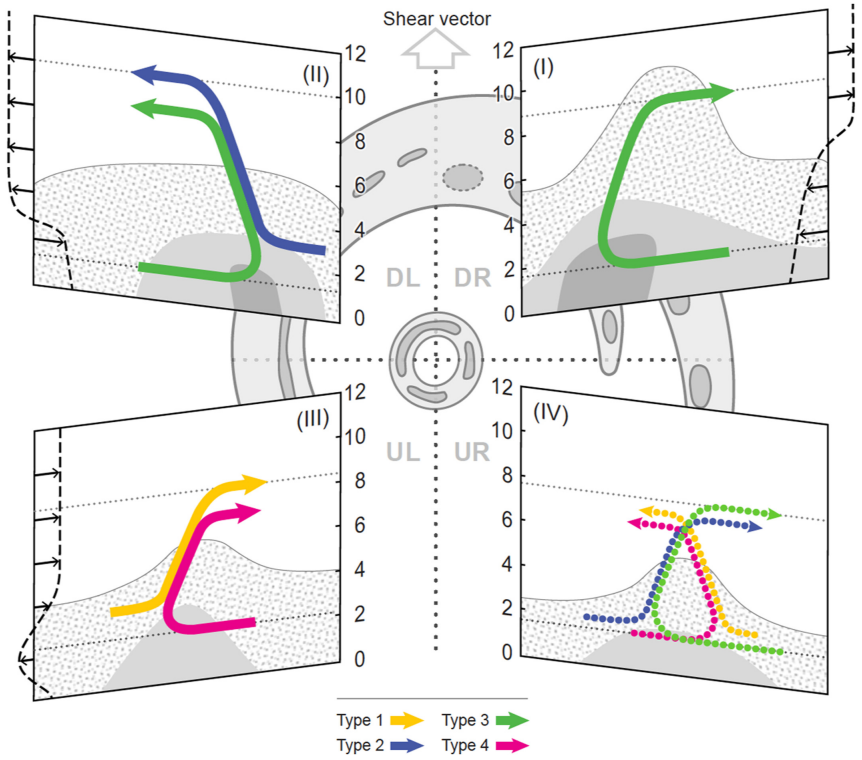

Figure 6: Figure 11 from Barron et al. (2022), detailing the typical updraft circulations for each shear-relative quadrant of a TC. Each quadrant also depicts reflectivity contours (20, 30, and 35 dBZ). The updrafts and reflectivity contours collectively show that the downshear quadrants tend to be more strongly convective than the upshear quadrants.

Bogner et al. 2000), entrainment from enhanced shear (e.g., Eastin et al. 2005), and outflow associated with the slanted structure of the secondary circulation (e.g., Didlake and Houze 2013a). Regarding the azimuthal asymmetry introduced by environmental vertical wind shear (e.g., Chen et al. 2006), they found the most convection in the downshear-left quadrant of the inner rainbands. Similarly, Barron et al. (2022) found the most robust convection in the downshear quadrants and, shown in Figure 6, identified the different secondary circulations associated with updrafts in each quadrant. They found the "in-up-out" circulation to be the most frequent, particularly in the downshear quadrants. Additionally, the downshear left quadrant exhibited the "out-up-out" circulation as a result of both an increase in evaporational cooling-induced

downdrafts from decaying convective cores and shear-related asymmetries that erode the depth of the inflow layer.

2.1.3 Outer Rainbands

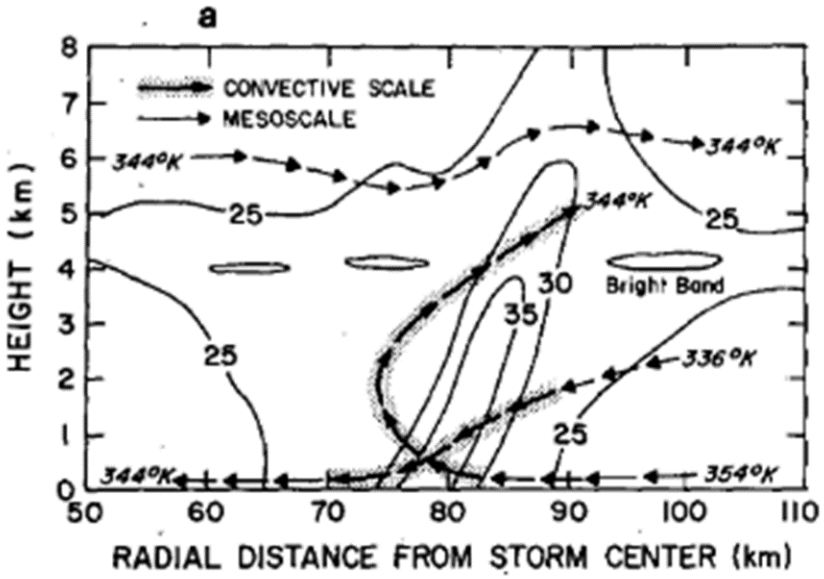

Figure 7: Figure 18a from Barnes et al. (1983). Depicts the vertical structure of a TC outer rainband. Notable features include an outwardly tilted reflectivity core, a secondary circulation radially inside of the enhanced reflectivity, a low-level downdraft, and stratiform precipitation on either side of the convective core.

Outer rainbands can be defined as existing outside of the VRW stagnation radius. There are still questions relating to how outer rainbands, or the principal rainbands from Figure 1, form. Theories such as inertia-gravity waves (e.g., Kurihara and Tuleya 1974), cold pools from evaporative cooling (e.g., Sawada and Iwasaki 2010a;b), the role of inner rainbands (e.g, Li and Wang 2012a; Li et al. 2017), and diurnal pulses (e.g., Ditchek et al. 2020) have been suggested.

Some outer rainband studies (i.e., Barnes et al. 1983; Powell 1990; Hence and Houze 2008; Didlake and Houze 2009; 2013a) have created schematics depicting the structure

and kinematics of these bands, shown in Figure 5 and Figures 7–10. Most of the schematics depict an outwardly tilted reflectivity core of >35 dBZ, which Houze (2010) dynamically compared to the slanted eyewall. All figures also capture low-level inflow, shown to be deeper and weaker than that of the inner rainband region in Figure 5. The increase in θ_e via the low-level inflow leads to an increase in instability which contributes to a slanted updraft, albeit less slanted than in the inner rainband region (Houze 2010; Didlake and Houze 2013a). Eventually, the updraft transitions into upper-level outflow. In Figures 7 and 9–10, a low-level downdraft was widely observed to enter the reflectivity as inflow before being pushed downward by precipitation drag and subsequent evaporative cooling (Didlake and Houze 2009; Houze 2010).

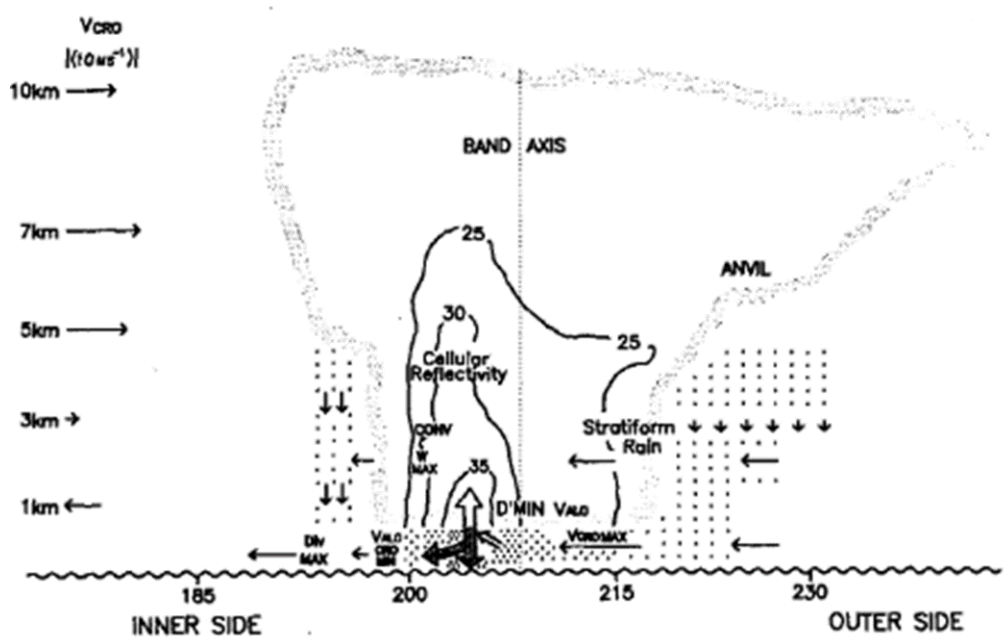

Figure 8: Figure 16 from Powell (1990), displaying the processes occurring within TC outer rainbands. Specifically, there is low-level inflow, upper-level outflow, an updraft collocated with enhanced reflectivity, and stratiform precipitation radially inside and outside of the updraft.

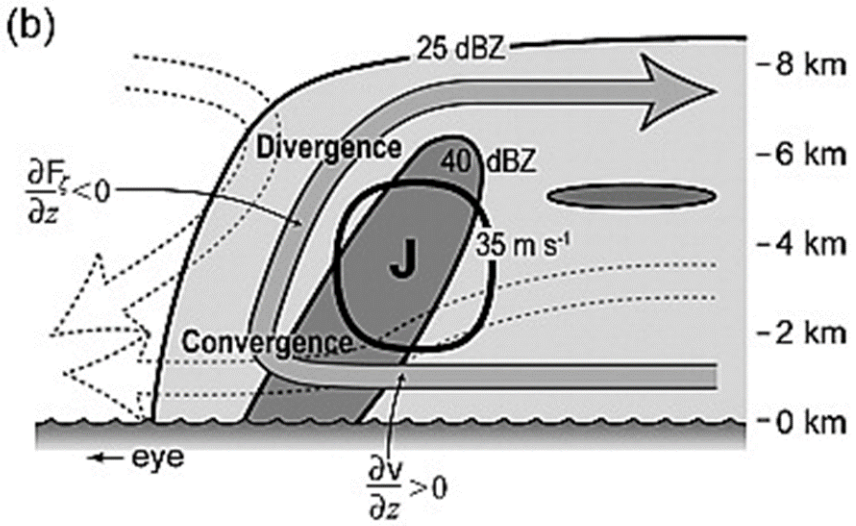

Figure 9: Figure 13b from Hence and Houze (2008), showing the cross section of the middle sector of an outer rainband. Low-level inflow, a robust updraft, and upper-level outflow are all evident. An outwardly tilted reflectivity core exists radially outside of the updraft with a collocated SHWM. A low-level downdraft intersects the convective core and an upper-level downdraft exists on the inner edge of the updraft. Stratiform precipitation is also drawn radially outside of the convective cell.

The conceptual models have also been expanded over time. For example, Figures 5 and 9 feature a secondary horizontal wind maximum (SHWM) radially outside of the updraft. This jet initiates from conservation of angular momentum and vertical advection in response to the formation of the updraft (Didlake and Houze 2013a) and is further strengthened by the concentration of positive vorticity from the tilting and stretching of shear-induced horizontal vorticity (Hence and Houze 2008; Houze 2010). Another addition is an upper-level downdraft located on the reflectivity gradient of the rainband's inner edge, shown in Figures 9–10. Around the updraft, a buoyancy-induced pressure gradient acceleration (BPGA) field is formed, inducing this downdraft where the largest vertical velocity horizontal gradient exists (Didlake and Houze 2009). Depending on the intensity of the BPGA field, the parcels in the downdraft can achieve negative buoyancy if they are forced into an area of precipitation and

undergo evaporative cooling (Didlake and Houze 2009). Lastly, Figure 10 features a low-level wind maximum (LLWM). Didlake and Houze (2009) explained that the vorticity couplet, from the tilting of horizontal vorticity, is positioned so that the negative vorticity component overlaps the upper-level downdraft. The downdraft transports the negative vorticity to the lower levels, forming a negative vorticity local maximum and strengthening the tangential winds (i.e., producing the LLWM) radially inside of the local maximum.

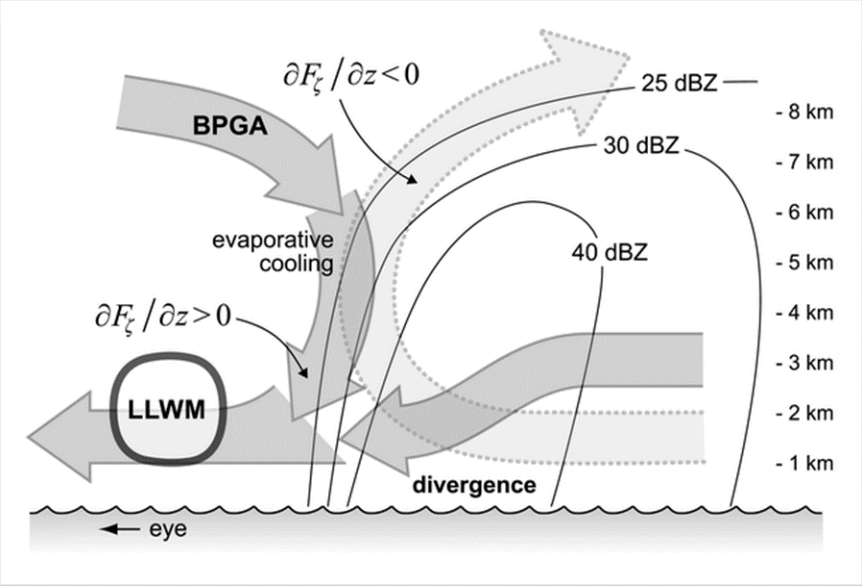

Figure 10: Figure 19 from Didlake and Houze (2009). There is an evident secondary circulation radially inside of outwardly tilted enhanced reflectivity. A low-level downdraft through the localized enhanced reflectivity is also evident, in addition to an upper-level downdraft on the inner edge of the updraft. A LLWM is also drawn radially inside of the upper-level downdraft.

The above schematics are mostly representative of convective processes. Therefore, a conceptual model for the outer rainband stratiform region has been created by Didlake and Houze (2013b), shown in Figure 11. Figure 11a depicts the general layout of stratiform and convection within a TC, where upwind convection moves downwind and ultimately decays into stratiform. Figure 11b conceptualizes a vertical cross section

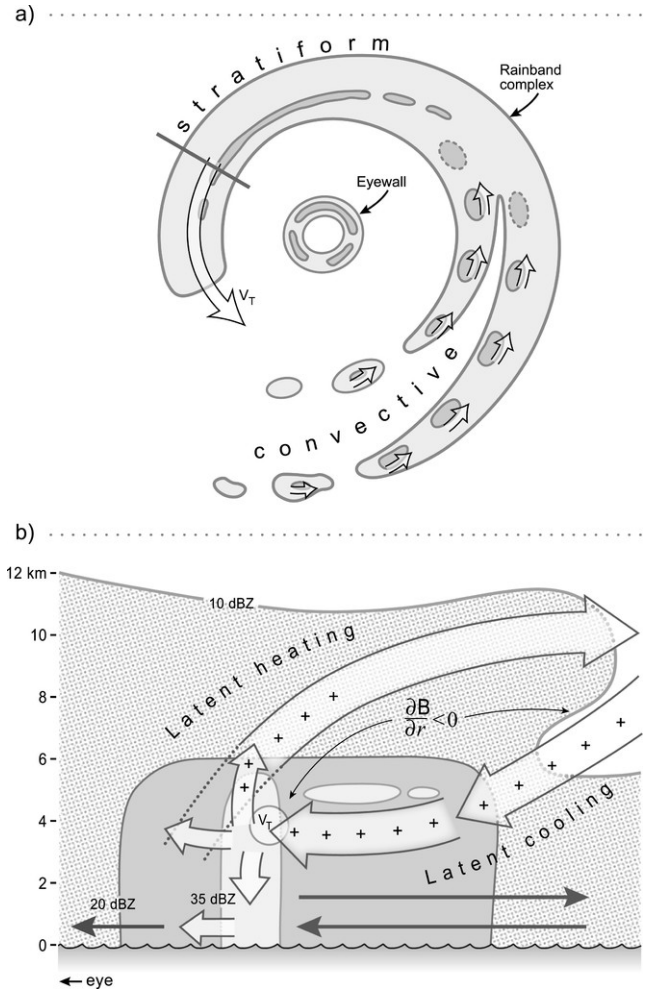

Figure 11: Figure 17 from Didlake and Houze (2013b). **a)** Depicts the plan view of a mature TC. The upwind sector shows forming convective cells that propagate downwind and eventually decay into stratiform precipitation. Tangential jets within the TC are depicted by arrows. **b)** A vertical cross section taken along the line in the stratiform region in panel a). Notable features include mid-level inflow, upper-level outflow, and a stacked downdraft and updraft. The decaying convection is also depicted by reflectivity contours.

through the stratiform region, consisting of broad low reflectivity values with a column of higher reflectivity and a 5-km bright band (i.e., melting layer). The updraft, from decaying convection, rises along angular momentum contours, produces latent heat, and ultimately forms an anvil. In response, horizontal vorticity is produced, which leads to mid-level inflow. In the mid-levels of the higher reflectivity core, convergence

exists where the mid-level inflow splits into the updraft, downdraft, and part of it continues as inflow.

2.2 Empirical Orthogonal Function (EOF) Analysis

Empirical orthogonal function (EOF) analysis, also referred to as a principal component analysis (PCA), is a statistical method performed to linearly recombine a data set into another data set, known as principal components (PCs), that represents the majority of the variance (Ringnér 2008; Abdi and Williams 2010; Wilks 2011). Before starting the analysis, the data are typically converted to anomalies via Equation 2.1 and sometimes standardized, depending on the desired outcome and whether the analyzed variables have the same units (Ringnér 2008; Abdi and Williams 2010; Wilks 2011).

$$\mathbf{X}' = \mathbf{X} - \overline{\mathbf{X}} \tag{2.1}$$

The covariance matrix of the anomaly data is defined by Equation 2.2,

$$\mathbf{C}_{\mathbf{X}'} = \frac{1}{n-1}\mathbf{X}'^{\mathrm{T}}\mathbf{X}', \tag{2.2}$$

where n represents the number of samples (Wilks 2011). While there are different ways to conduct a PCA, one common method is by using a singular value decomposition (SVD) algorithm of the form

$$\mathbf{X}' = \mathbf{U}\Sigma\mathbf{V}^{\mathrm{T}}, \tag{2.3}$$

where $\mathbf{U}$ represents the left singular vectors, Σ represents the singular values, and $\mathbf{V}$ represents the right singular vectors (Abdi and Williams 2010). Substituting Equation 2.3 into Equation 2.2 yields

$$\mathbf{C_X} = \frac{1}{n-1}\mathbf{V}\Sigma(\mathbf{U}^{\mathrm{T}}\mathbf{U})\Sigma\mathbf{V}^{\mathrm{T}} = \mathbf{V}\frac{\Sigma^2}{n-1}\mathbf{V}^{\mathrm{T}}, \tag{2.4}$$

where $\mathbf{V}$ consists of the eigenvectors and $\frac{\Sigma^2}{n-1}$ consists of the eigenvalues (Wilks 2011). If the anomaly data set is larger than one dimension, the eigenvectors can be visualized on a scatter plot (e.g. Figure 12), where each variable is represented on each axis (Ringnér 2008; Abdi and Williams 2010; Wilks 2011). So long as all eigenvectors are orthogonal to each other, they are drawn in the direction of the most variance for each axis. Each eigenvector has a corresponding eigenvalue, where the eigenvalue linked to the first eigenvector has the largest magnitude (Wilks 2011). While eigenvectors typically have a unit length of 1, they can be scaled by the square root of their respective eigenvalue for ease of interpretation (Wilks 2011).

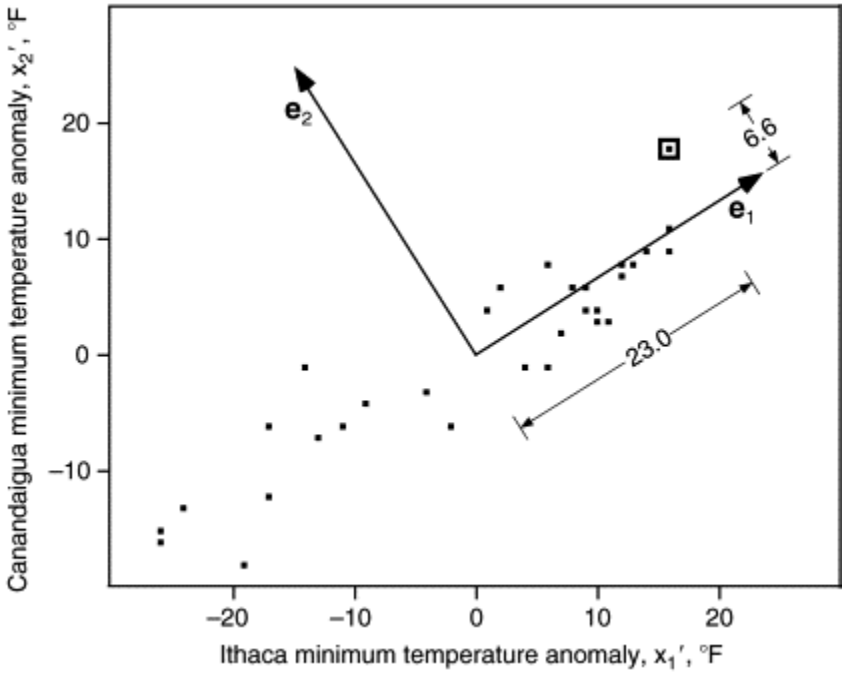

Figure 12: Figure 12.1 from Wilks (2011). Scatterplot displaying minimum temperature data for two different locations. The first eigenvector ($\mathbf{e}_1$) is drawn in the direction of the largest variance in the data. The second eigenvector ($\mathbf{e}_2$) is drawn orthogonally to $\mathbf{e}_1$, so that it represents the second largest variance in the data while fulfilling the orthogonality requirement.

PCs, which represent the anomaly data in the coordinate system defined by the eigenvectors, can be obtained by projecting the anomaly data onto the eigenvectors, as in Equation 2.5 (Wilks 2011).

$$\text{PCs} = \mathbf{X}'\mathbf{V} \tag{2.5}$$

Figure 12 displays an example of a PC vector for the data point within the black square, where the PC vector components are of magnitudes 23.0 and 6.6. If the anomaly data have a time component, Equation 2.5 can be used to construct a PC time series to relate patterns across time.

Lastly, the variance explained, or the percentage that represents the fraction of the variance associated with a given eigenvector, can be calculated using Equation 2.6,

$$\text{Variance Explained} = 100\% \times \frac{\lambda_i}{\sum_{i=1}^{i=m} \lambda_i}, \tag{2.6}$$

where the numerator represents the eigenvalue for a given eigenvector and the denominator represents the sum of eigenvalues for all eigenvectors.

EOF analyses are commonly used for climate-related studies (e.g., Roundy 2015; You and Furtado 2017), but less commonly used for meteorological studies. In one meteorological example, Biggerstaff et al. (2006) used an EOF analysis to identify differences in cloud property anomalies across numerical simulations of a squall line. Similarly, Biggerstaff and Seo (2010) did an EOF analysis to evaluate whether simulated tropical precipitation, which is used for rain rate retrievals, is representative of actual tropical rainfall, especially given the high variability in precipitation across the tropics.

Figure 13 depicts example results of the EOF analysis by Biggerstaff et al. (2006) for vertical velocity and latent heating in both convective and stratiform regions. Each

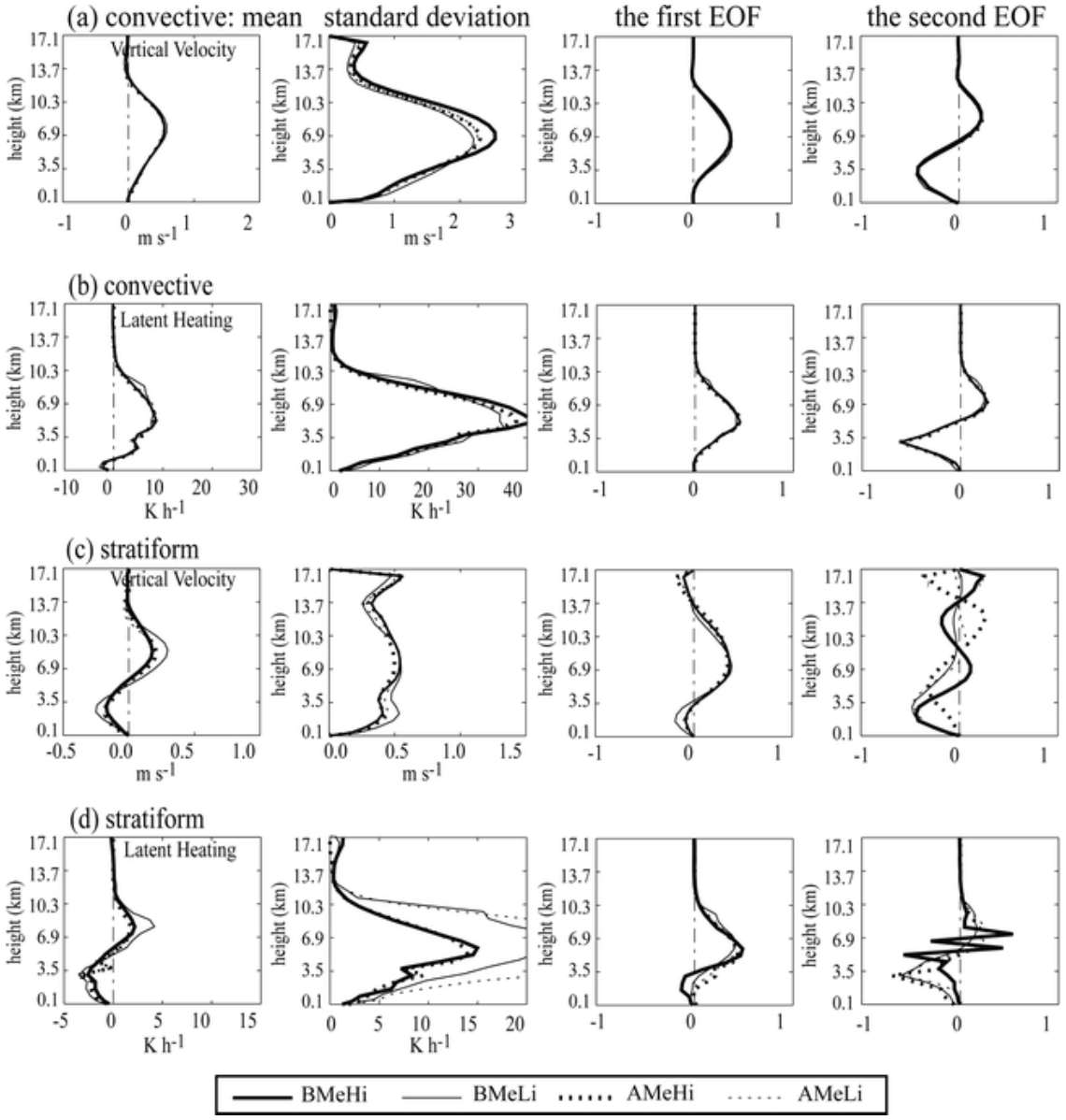

Figure 13: Figure 5 from Biggerstaff et al. (2006). Shows the mean, standard deviation, EOF-1, and EOF-2 vertical profiles for vertical velocity and latent heating in convective and stratiform regions. Each plot consists of four vertical profiles, representing each simulation.

of the four profiles represents two simulated microphysical schemes (A or B) consisting of two different ice crystal amounts (H or L), designated as AM_eH_i, AM_eL_i, BM_eH_i, and BM_eL_i. The first and second EOF profiles represent the eigenvectors of the perturbations corresponding to each variable for each simulation. Their associated

eigenvalues, identifying the fraction of the variance represented, are located in Table 1. Overall, Biggerstaff et al. (2006) concluded that the EOF analysis was useful for drawing comparisons among the different simulations.

	BM_eH_i				AM_eH_i				BM_eL_i				AM_eL_i			
Variables	Convective		Stratiform		Convective		Stratiform		Convective		Stratiform		Convective		Stratiform	
Water vapor	76	*10*	81	*9*	72	*12*	78	*11*	76	*21*	79	*9*	70	*21*	75	*13*
Cloud water	70	*21*	50	*27*	69	*22*	48	*30*	63	*24*	60	*19*	65	*23*	55	*17*
Rain	90	*9*	90	*8*	89	*9*	93	*6*	90	*9*	88	*11*	88	*9*	92	*7*
Cloud ice	74	*16*	67	*16*	76	*14*	64	*24*	90	*6*	80	*9*	84	*10*	78	*11*
Snow	86	*5*	30	*26*	70	*14*	62	*20*	80	*15*	77	*14*	65	*19*	60	*27*
Graupel	86	*11*	89	*8*	87	*9*	92	*6*	90	*7*	87	*10*	88	*7*	89	*9*
Radar reflectivity	71	*23*	96	*3*	92	*3*	98	*1*	93	*2*	93	*5*	92	*3*	98	*1*
Vertical motion	72	*15*	37	*18*	66	*19*	35	*19*	59	*25*	32	*23*	64	*22*	31	*20*
Latent heating	78	*16*	73	*13*	74	*19*	75	*17*	65	*26*	67	*22*	71	*22*	72	*21*

Table 1: Table 2 from Biggerstaff et al. (2006), presents the eigenvalues for the first (regular font) and second (italicized font) EOFs. The eigenvalues were calculated for nine different variables across four simulations in both convective and stratiform regions.

Biggerstaff and Seo (2010) looked at brightness temperature (T_B) in four different regions in the tropics [i.e, northwest Pacific (NWP), southwest Pacific (SWP), east Pacific (EP), and the Atlantic (TA)] and used three storm simulations (i.e., KWAJ, KAMP, and TOGA) with varying levels of organization, two of which had comparable thermodynamics. The purpose of covering several regions and using multiple simulations was to ensure adequate variability in the precipitation structure. Figure 14 displays EOF analysis results of the observed radiance indices for each tropical region for category 1–3 precipitation types that correspond to convection, convection-stratiform mixture, and stratiform, respectively. In general, the primary observed cloud structure in each region can be inferred from this figure. Similarly, Figure 15 depicts the EOF results of the simulated radiance indices for each precipitation category. Biggerstaff and Seo (2010) concluded that consideration of the thermodynamic environment between

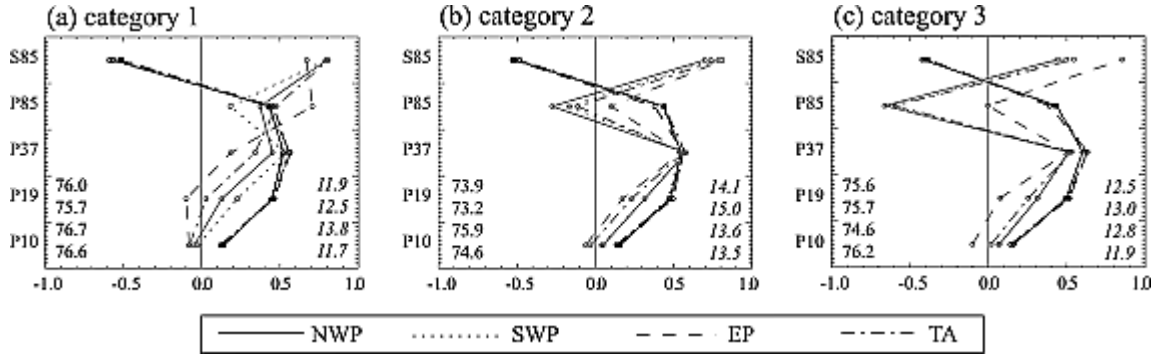

Figure 14: Figure 5 from Biggerstaff and Seo (2010), which shows EOF-1 (black lines) and EOF-2 (gray lines) for the observed radiance indices. The eigenvalues for EOF-1 and EOF-2 are presented in regular and italic font, respecitively. From the top down, the eigenvalues correspond to NWP, SWP, EP, and TA. Panel a) represents convective precipitation, panel b) represents a convective and stratiform precipitation mixture, and panel c) represents stratiform precipitation.

the simulated and observed regions is important, graupel is often overrepresented in simulations, and cloud types are often inadequately represented in the simulations.

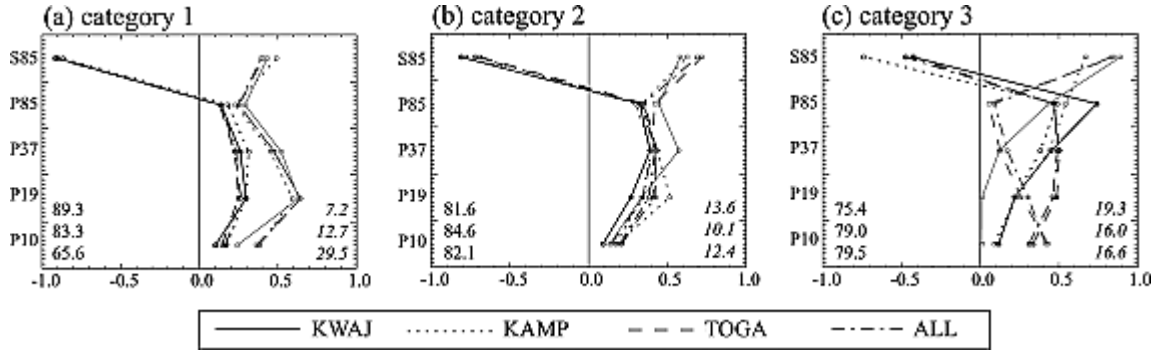

Figure 15: Figure 7 from Biggerstaff and Seo (2010). As in Figure 14, except for simulated radiance indices. From the top down, the eigenvalues correspond to KWAJ, KAMP, and TOGA.

In general, Biggerstaff et al. (2006) and Biggerstaff and Seo (2010) demonstrated the usefulness of analyzing meteorological data via EOF analysis. While EOF analysis is scarcely used, it could potentially be used to resolve the vertical structure of a variety of meteorological phenomena or to draw comparisons between observed and simulated meteorological phenomena.

Chapter 3

Data & Methods

3.1 Hurricane Laura Overview

The National Hurricane Center Tropical Cyclone Report for Hurricane Laura by Pasch et al. (2020) detailed the history of the storm. In summary, Laura originated as a westward propagating tropical wave from the west coast of Africa before converging with a low pressure region, becoming more organized. Laura was declared a tropical depression by 0000 UTC on 20 August, before becoming a tropical storm with 40-kt (20.6 m s^{-1}) maximum winds on 21 August. Laura was offically declared a hurricane on 25 August upon reaching the southeastern Gulf of Mexico. While in the Gulf of Mexico, Laura underwent rapid intensification on 26 August, becoming 55 kt (28.3 m s^{-1}) stronger by 0000 UTC 27 August. Laura's strongest winds were roughly 130 kt (66.9 m s^{-1}) a few hours prior to making landfall in Cameron, LA at 0600 UTC on 27 August as a Category 4 hurricane.

3.2 SMART-R Background & Deployment

The Shared Mobile Atmospheric Research and Teaching Radars (SMART-Rs, hereafter SRs) are C-band mobile dual-polarimetric Doppler radars, as outlined by Biggerstaff et al. (2005) and Biggerstaff et al. (2021). In brief, the SRs were developed in part to

Radar Specifications				
Radar Name	**Frequency**	**Beamwidth**	**Peak Power**	**Antenna Diameter**
Lake Charles, LA WSR-88D (KLCH)	2700-3000 MHz (S-band)	Approx. 1°	750 kW	8.5 m
SR1	5593 MHz (C-band)	1.5°	300 kW (each channel 150 kW)	2.4 m

Table 2: The specifications for the KLCH and SR1 radars. Includes the frequency, beamwidth, peak power, and antenna diameter. KLCH information retrieved from Crum and Alberty (1993) and SR1 information retrieved from Biggerstaff et al. (2021).

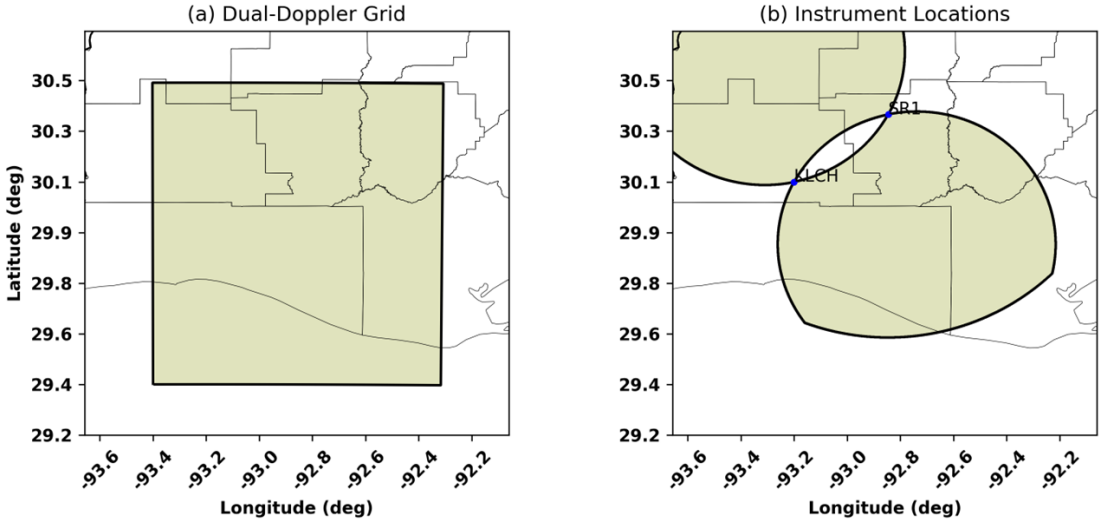

Figure 16: a) The collective dual-Doppler grid for Hurricane Laura from the SR1 and KLCH radars. **b)** The locations of the SR1 and KLCH radars, with the dual-Doppler lobes designating where 3-D wind retrievals were obtained. The baseline between the two radars was about 44 km.

capture meteorological phemonena that may not otherwise be observed by stationary S-band WSR-88D radars, as the SRs are able to move to storm locations. Depending on the research goal, SRs offer some advantages over X-band radars as well, such as

less attenutation and a higher Nyquist velocity. Some notable SR specifications are included in Table 2. At the time Biggerstaff et al. (2005) was written, the SRs only had the capability to collect radar reflectivity (Z), velocity (V), and spectrum width (σ_v) data. However, the SRs were later modified to have the ability to collect polarimetric data including differential reflectivity (Z_{DR}), differential phase (ϕ_{dp}), and correlation coefficient (ρ_{hv}) (Biggerstaff et al. 2021).

Scanning Strategies				
Radar Name	**Elevations (°)**	**Nyquist Velocity**	**Range Gate Spacing**	**Volumetric Update Time**
Lake Charles, LA WSR-88D (KLCH)	0.5, 0.9, 1.3, 1.8, 2.4, 3.1, 0.5, 4.0, 5.1, 6.4, 8.0, 10.0, 12.0, 14.0, 16.7, 19.5	± 29.01 – 34.01 m s^{-1}	250 meters	6-7 minutes
SR1	0.8, 1.5, 2.3, 3.2, 4.0, 4.7, 5.5, 6.2, 7.0, 8.0, 9.0, 10.0, 11.0, 12.0, 14.0, 16.0, 18.0, 20.0, 23.0, 26.0	± 16.08 m s^{-1}	75 meters	5-6 minutes

Table 3: The scanning strategies for the KLCH and SR1 radars during the Hurricane Laura deployment. Includes the elevations, Nyquist velocity, range gate spacing, and volumetric update time.

Before Laura made landfall, both SRs traveled to the Louisiana coast to collect data. However, SR2 was unavailable for the entire deployment. Therefore, the Lake Charles, LA WSR-88D (KLCH) was substituted to complete dual-Doppler retrievals in cooperation with SR1. SR1 data are valid from 2359 UTC 26 August 2020 through

1046 UTC 27 August 2020 and KLCH data are valid from 2353 UTC 26 August 2020 through 0553 UTC 27 August 2020, when KLCH sustained damage and became inoperable. The radar locations and dual-Doppler domain are mapped in Figure 16 and the radar scanning strategies are listed in Table 3.

3.3 Data Processing

After obtaining the WSR-88D data from the National Centers for Environmental Information (NCEI), following the methodology of Alford et al. (2019) and Biggerstaff et al. (2021), the SR data and KLCH data were both objectively dealiased by the Python ARM Radar Toolkit (Py-ART, Helmus and Collis 2016). To ensure the data were sufficiently edited by Py-ART, the data were then manually inspected and subjectively edited using the National Center for Atmospheric Research (NCAR) Solo3 software package (Oye et al. 1995).

Using a natural neighbor interpolation scheme (Sibson 1981), the edited volumes were then interpolated to a 1-km horizontally spaced and 500-m vertically spaced cartesian grid. Based on the grid origin, KLCH, the grid spanned from -10 km to 100 km in the x-direction, -80 km to 40 km in the y-direction, and 0.5 km to 10 km in the z-direction. To account for errors resulting from time differences across a given volume, the V_R and Z_H data were then passed through an objective advection correction algorithm (Shapiro et al. 2010). From Potvin et al. (2012), the three-dimensional variational data assimilation (3DVAR) method was then used to obtain dual-Doppler wind retrievals (i.e., DDAs) with a temporal resolution of 5-10 minutes. DDAs are available from 0002 UTC through 0550 UTC for 27 August 2020. However, due to time constraints relating to advection correction execution, only the analyses from

0106 UTC through 0544 UTC were used in this analysis. This time constraint reduces the number of available outer rainband profiles.

3.4 Methodology

Typically, hurricanes are analyzed relative to their storm center, which can be defined relative to different variables, such as reflectivity (e.g., Griffin et al. 1992), tangential wind (e.g., Lee and Marks 2000), pressure (e.g., Braun et al. 2006), and others. Although Nguyen et al. (2014) identified the pressure centroid method to be the best for center-finding, pressure measurements cannot be collected by radars. Therefore, the most objective way the center can be defined in this case is by using the ground-based velocity-track-display (GBVTD) algorithm described by Lee and Marks (2000). While this algorithm can be used with dual-Doppler data, it was solely run with the KLCH data due to that radar having the longest interval of eyewall wind observations. For the period before the eyewall was in range of KLCH, and thus the GBVTD algorithm could not be used, the Atlantic Oceanographic and Meteorological Laboratory (AOML) center estimates were assumed. These estimates are determined according to methodology described by Willoughby and Chelmow (1982).

The dataset was then divided into the eyewall, inner rainband, and outer rainband components. Some studies have defined the inner-outer rainband divide as the radius that is 2-3 times the radius of maximum wind (RMW) (Wang 2009; Li and Wang 2012b). However, a better definition involves VRWs. Because VRWs have been observed to propagate along the negative radial vorticity gradient (Montgomery and Kallenbach 1997; Abarca and Corbosiero 2011), the radius where the negative gradient diminishes, called the stagnation radius, marks the inner boundary of the

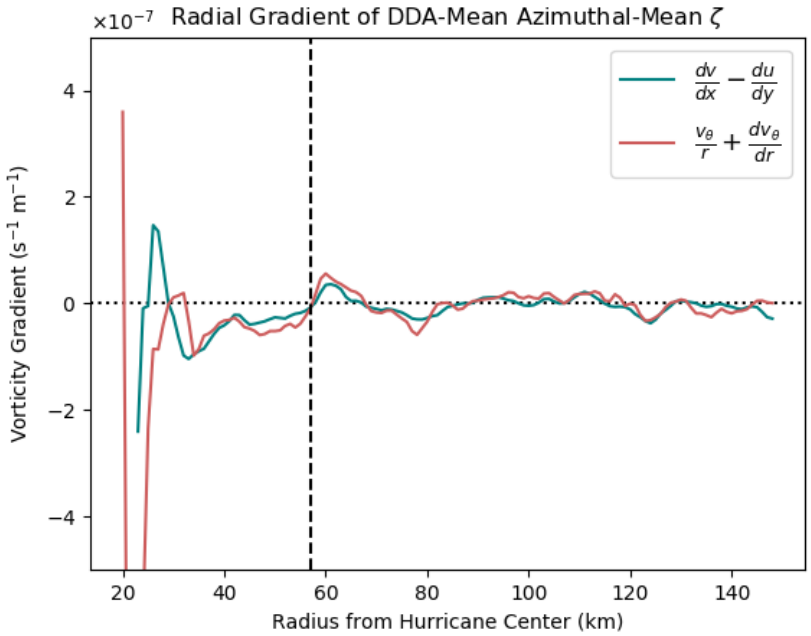

Figure 17: The DDA-mean azimuthal-mean radial gradient of relative vorticity, for two different vorticity calculation methods. Using both methods, the radial vorticity gradient becomes positive at a radius of 57 km (dashed black line), marking the divide between the inner and outer rainbands.

outer rainband region. Two different methods for calculating vorticity were used (i.e., $dv/dx - du/dy$ and $\bar{v}_\theta/r + d\bar{v}_\theta/dr$, where r is the radius and $\bar{v}_\theta$ is the azimuthally averaged tangential wind). From both methods, the DDA-mean azimuthal-mean relative vorticity gradient became positive at a radius of 57 km, shown in Figure 17, thereby signaling the inner-outer rainband divide. Due to the lack of a documented partitioning method, the boundary between the eyewall and inner rainbands was determined based on profiles of DDA-mean azimuthal-mean reflectivity, radial wind, azimuthal wind, and vertical velocity (e.g., Figure 18). All mean variables showed a sharp gradient at a radius of 50 km, therefore indicating the eyewall-inner rainband divide.

To partition between the convective and stratiform regions of the DDAs, two Py-ART convective-stratiform modules, adapted from Steiner et al. (1995), Yuter and

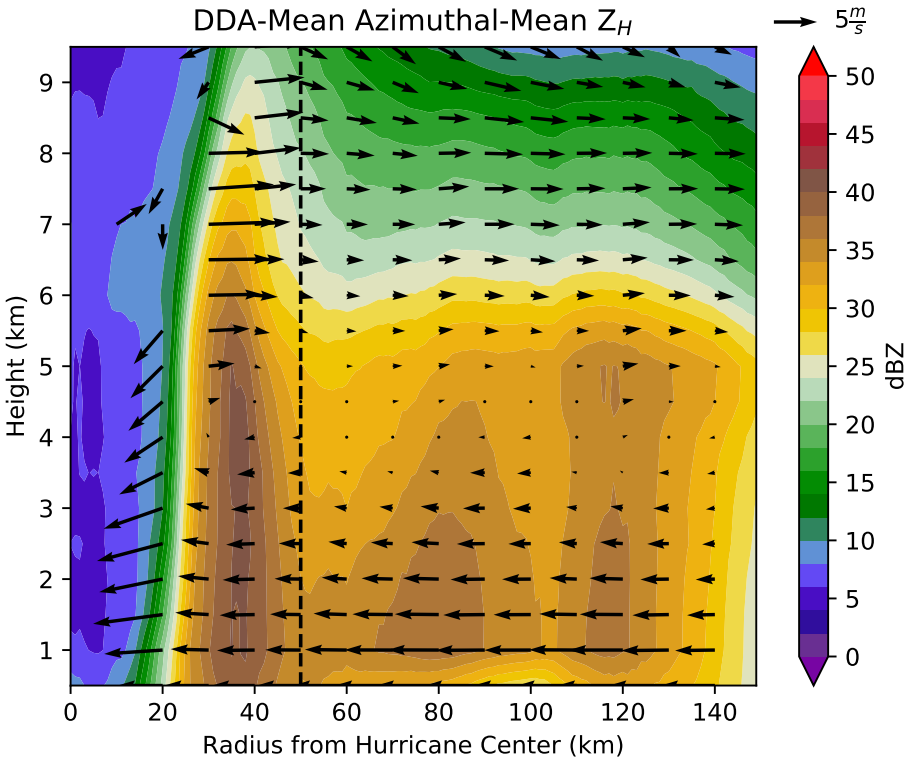

Figure 18: The DDA-mean azimuthal-mean radar reflectivity (shaded) and azimuthal mean radial and vertical velocity (vectors). The dashed black line at a radius of 50 km marks the divide between the eyewall and inner rainbands.

Houze (1997), and Yuter et al. (2005), were explored (Helmus and Collis 2016). However, both partitioning methods use reflectivity to determine convective cores. While reflectivity can provide a rain rate estimate, it is not necessarily a reliable proxy for dividing convective and stratiform regions because vertical velocity maxima and reflectivity maxima can often be misaligned, as shown in several conceptual models. Because vertical velocity is available in this analysis, it was used to divide between convective and stratiform regions instead of reflectivity. In support of this method, several studies have identified a vertical velocity of 2 m s^{-1} as a cutoff between the stratiform and convective regions (e.g. Steiner et al. 1995; Houze Jr 1997; Didlake and Houze 2013b), where velocities below the cutoff are indicative of stratiform and vice versa. Convective

regions were further divided into updraft and downdraft regions. To avoid oversampling convective cores, only the local maximum and local minimum drafts within 4-km by 4-km grids were selected. Updraft and downdraft profiles exclusively contain >0 m s^{-1} and <0 m s^{-1} vertical velocities, respectively. To ensure the stratiform regions were exclusively stratiform, rather than weak convective echoes, only weak drafts with surface reflectivity values of <30 dBZ were included. An example of this partitioning method is shown in Figure 19. To incorporate profiles that contain both updrafts and downdrafts, reflectivity cores were also selected. Reflectivity core profiles are defined as profiles collocated with low-level reflectivity maxima (>40 dBZ) in a 4-km x 4-km grid. This partitioning method is also included in Figure 19. It should be noted that these profiles are solely vertical, so slanted convection is not directly analyzed. However, slanted convection can be inferred within the EOF analyses.

Once the data were divided into their respective convective, stratiform, and reflectivity core components for the eyewall, inner rainbands, and outer rainbands, they were then partitioned into four shear-dependent quadrants. This was done because high environmental wind shear has been shown to cause variations in the kinematic structure of different parts of a TC (e.g., Hence and Houze 2012; Barron et al. 2022). The estimated environmental wind shear values, defined as 0-500 km center-relative horizontally averaged 200-850 hPa vortex-removed shear, and their corresponding vectors were obtained from the Statistical Hurricane Intensity Prediction Scheme (SHIPS) model (DeMaria and Kaplan 1994). Because the temporal resolution of these values is 6 hours, a linear interpolation was completed to infer the hourly environmental shear estimates. After the interpolation, each DDA time dataset was divided into the downshear left, downshear right, upshear left, and upshear right quadrants based on its

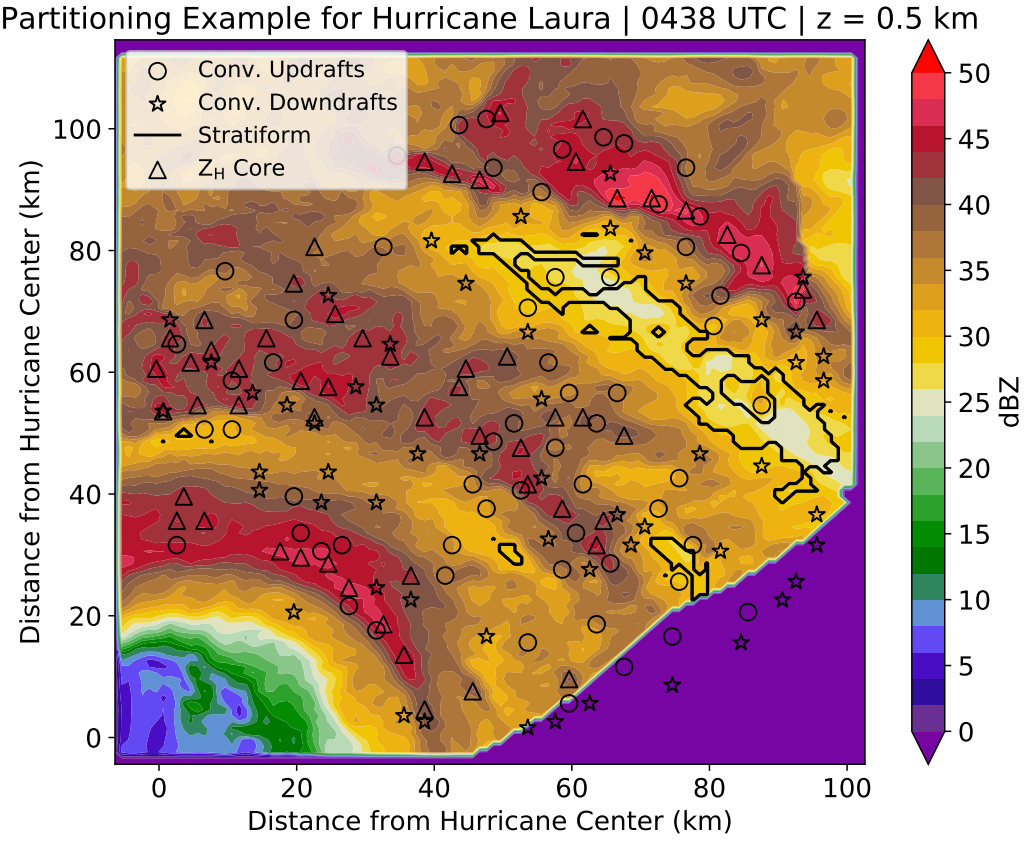

Figure 19: Plan view example of the convective updraft (black circles), convective downdraft (black stars), stratiform (black contours), and reflectivity core (black triangles) regions of Hurricane Laura that have been partitioned using the methods described in Section 3.4. These regions are overlaid on 0.5-km height radar reflectivity (shaded) from 0438 UTC.

interpolated shear information. It should be noted that only the downshear left quadrant was analyzed in this study, as the upshear quadrants were not sampled and the downshear right quadrant was minimally sampled.

Once the data were divided into their respective quadrants, all vertical profiles with missing values were removed. Then, the mean vertical profile was calculated for each TC region for radial wind (V_R), azimuthal wind (V_θ), vertical velocity (w), relative vorticity (ζ), divergence ($\nabla_H \cdot \vec{V}$), and radar reflectivity (Z_H). The anomalies were then calculated by subtracting the mean profile from each vertical profile. Then,

the vertical profile for each region was passed through the scikit-learn PCA module (Pedregosa et al. 2011). The eigenvector output was then scaled by multiplying each EOF with the square root of its corresponding eigenvalue for ease of interpretation (Wilks 2011). Finally, the mean profile for each region was added back to the EOF anomalies in order to interpret the EOFs as complete profiles rather than as anomaly profiles.

Chapter 4

Results: Azimuthal Mean Vertical Profiles

Many of the features detailed in the Chapter 2 conceptual models were identified from composite analyses of the respective regions. To provide a fair comparison between Hurricane Laura and the conceptual models, azimuthal-mean vertical profiles for radar reflectivity (Z_H), vertical velocity (w), radial velocity (V_R), azimuthal velocity (V_θ), relative vorticity (ζ), and divergence ($\nabla_H \cdot \vec{V}$) were computed across all DDA times for the downshear left quadrants of the eyewall, inner rainband, and outer rainband regions. These profiles are shown in Figures 20–22.

4.1 Eyewall Region

From Figure 20a, the eyewall reflectivity structure agrees with the conceptual model of Jorgensen (1984), where the low-level reflectivity maximum is upright and the upper-level reflectivity tower is tilted outward. Based on the radial and vertical velocity vectors, the slant of the reflectivity core at the upper levels is the manifestation of hydrometeor advection by the radial outflow (Jorgensen 1984; Marks and Houze 1987). Contoured in Figure 20c, the radial velocity is shown to be strongest in the upper levels as outflow, where the tilted reflectivity core is most notable. The outwardly slanted updraft, extensively covered in TC literature and included in every schematic

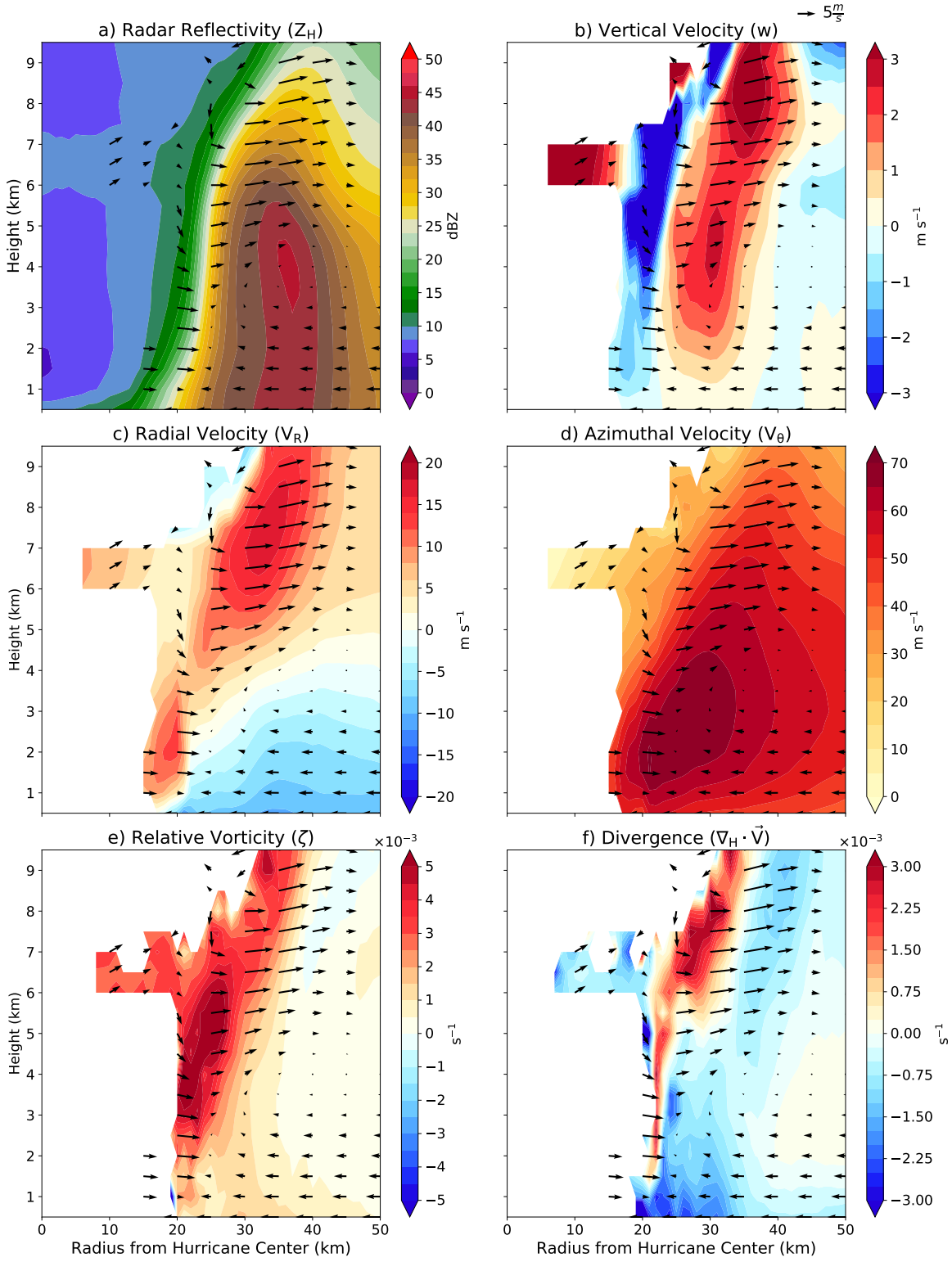
Downshear Left Eyewall DDA-Mean Azimuthal-Mean Variables
a) Radar Reflectivity (Z_H)
b) Vertical Velocity (w)
$5\frac{m}{s}$
c) Radial Velocity (V_R)
d) Azimuthal Velocity (V_θ)
e) Relative Vorticity (ζ)
f) Divergence ($\nabla_H \cdot \vec{V}$)
Height (km)
Radius from Hurricane Center (km)
dBZ
m s^{-1}
s^{-1}
$\times 10^{-3}$

Figure 20: The DDA-mean azimuthal-mean vertical profiles of **a)** radar reflectivity (dBZ), **b)** vertical velocity (m s^{-1}), **c)** radial velocity (m s^{-1}), **d)** azimuthal velocity (m s^{-1}), **e)** relative vorticity (s^{-1}), and **f)** divergence (s^{-1}) for the downshear left eyewall in Hurricane Laura. Black vectors represent the radial and vertical velocities.

in Section 2.1.1, is evident in Figure 20b. Radially inside of the updraft, there is a substantial downdraft. According to Jorgensen (1984) and Willoughby (1998), this could be subsidence occurring in the eye in response to the eyewall updraft. A weaker downdraft is also evident beneath the updraft, depicted in all conceptual models in Section 2.1.1, resulting from hydrometeor fallout. Also shown in all conceptual models, the secondary circulation structure is apparent in Figure 20c, where radial inflow is limited to the lowest 3 km. The outwardly tilted azimuthal velocity structure documented by Jorgensen (1984) and Marks and Houze (1987) is shown in Figure 21d, where the maximum (i.e., RMW) occurs at a radius of 21 km from the storm center. Figure 20e shows mean cyclonic (positive) vertical vorticity across the eyewall, with the maximum vorticity occurring in the mid-levels on the inner edge of the updraft. While the conceptual models in Section 2.1.1 do not include relative vorticity, this result is expected. Namely, based on ideas from Hence and Houze (2008) and Houze (2010), horizontal vorticity is generated from speed shear below the tangential jet in the eyewall. This horizontal vorticity ultimately gets tilted and advected upward by the updraft. From Figure 20f, upper-level divergence above the lower-level updraft decreases the positive vorticity in the upper levels. To satisy mass continuity, low-level convergence must exist near the surface at the base of the updraft, which is clear in Figure 20f.

4.2 Inner Rainband Region

From Figure 21a, the inner rainband reflectivity field is lower in magnitude compared to the eyewall, and convective cores are indistinguishable. Because of the transient

and shallow nature of convectively-coupled VRWs, individual bands of reflectivity are likely getting smoothed when the mean is calculated. Jorgensen (1984) and Marks and Houze (1987) designated the region outside of the eyewall as stratiform, complete with downward motion beneath the melting layer and upward motion above it. However, possibly resulting from shear, the reflectivity field does not exhibit any evidence of a melting layer and, from Figure 21b, broad mean upward motion is seen below a height of 4 km. The vertical draft structure is consistent with the findings of Didlake and Houze (2013a), where inner rainband updrafts are confined to the lower levels. The "in-up-out" secondary circulation described by both Didlake and Houze (2013a) and Barron et al. (2022) is shown in Figure 21c, although the mean inflow is deeper than Didlake and Houze (2013a) described. Since convective cores are not resolved in these profiles, it is rather unsurprising that tangential jets associated with the convection are not resolved in Figure 21d, either. The background azimuthal velocity shows a decrease in magnitude with increasing radius. Despite not being covered in conceptual models, azimuthal velocity would have to decrease with increasing radius to conserve angular momentum. The background vertical vorticity shown in Figure 21e is cyclonic, which is broadly consistent with TC literature (e.g., Gray 1968). In the upper levels, the vertical vorticity is more strongly positive, which could possibly be from the advection of eyewall positive vorticity outward by the outflow. Based on mass continuity arguments, in response to the low-level mean updrafts, low-level horizontal convergence should exist at the updraft base and horizontal divergence should exist above the updraft. Evidently, from Figure 21f, this is the case.

Downshear Left Inner Rainband DDA-Mean Azimuthal-Mean Variables

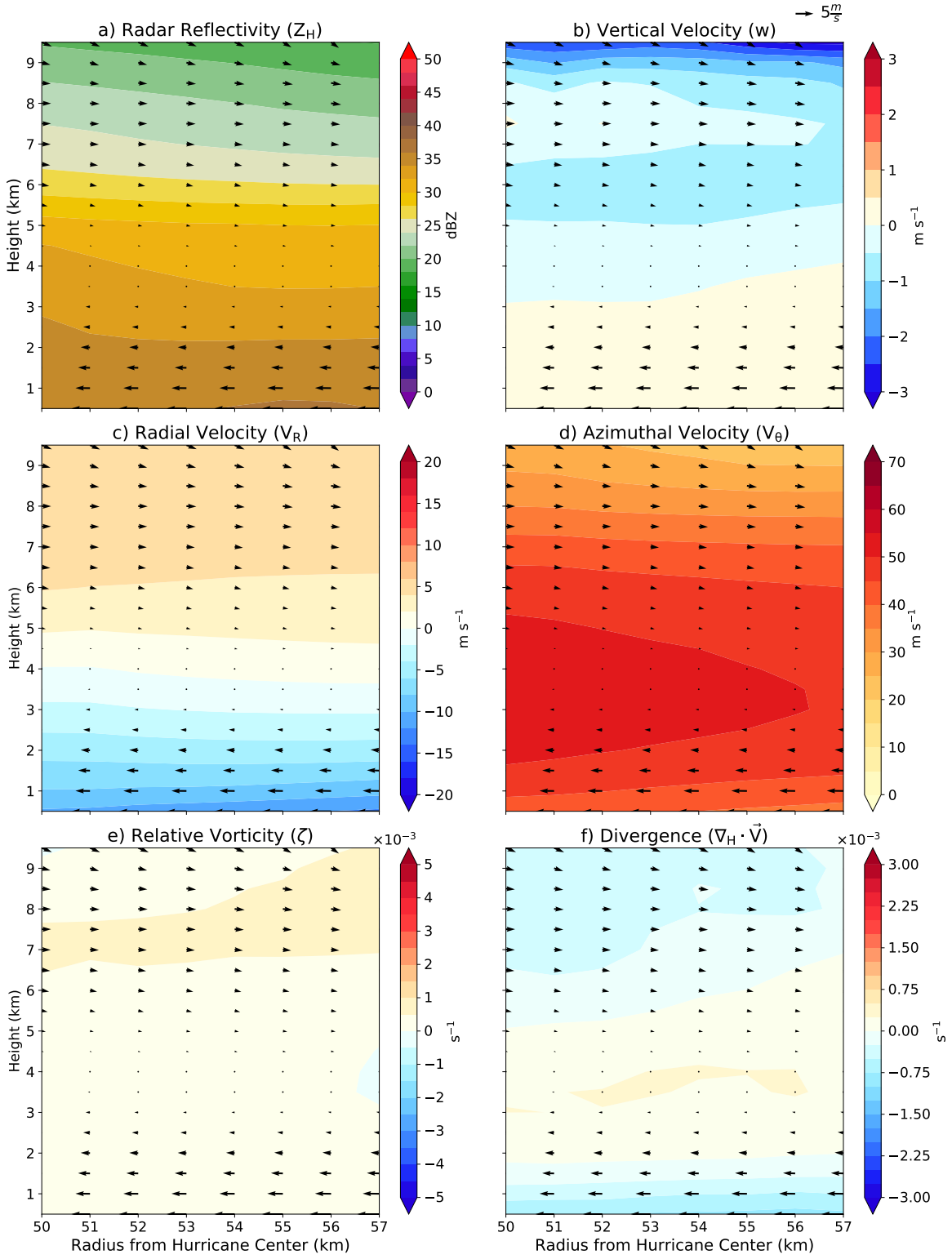

Figure 21: As in Figure 20, but for the inner rainband region.

4.3 Outer Rainband Region

From Figure 22a, convective towers can be resolved in the reflectivity field that increase in height with increasing radius. While the updrafts shown in Figure 22b extend to the same heights, the updrafts at larger radii appear to be stronger. These results are consistent with the findings of Didlake and Houze (2013a), as they similarly found that rainbands at larger radii are deeper and have stronger updrafts. Figure 22b also shows mean downdrafts next to the updrafts, which points to the presence of the upper-level downdraft described by Hence and Houze (2008) and Didlake and Houze (2009). The low-level downdraft shown in most conceptual models in Section 2.1.3 could also be present. Its presence is further supported by the slanted inflow structure at the updraft bases in Figure 22c. The secondary circulation depicted in most conceptual models is evident in this analysis as well. However, using the Zhang et al. (2011) definition of radial inflow depth, the inflow depth difference between the inner and outer rainbands cannot be determined, as the lower extent of the analysis is a height of 0.5 km. The azimuthal velocity is lower in magnitude compared to the inner rainbands and continues to decrease with radius, consistent with angular momentum conservation. Between a height of 2-3 km, the azimuthal velocity contours protrude outward, possibly hinting at the secondary horizontal wind maximum (SHWM) described by Hence and Houze (2008). From Figure 22e, pockets of anticyclonic vertical vorticity exist. These are likely manifestations of the vorticity couplets described by Hence and Houze (2008) and Didlake and Houze (2009). Lastly, low-level convergence and upper-level divergence exist in Figure 22f, which is consistent with mass continuity.

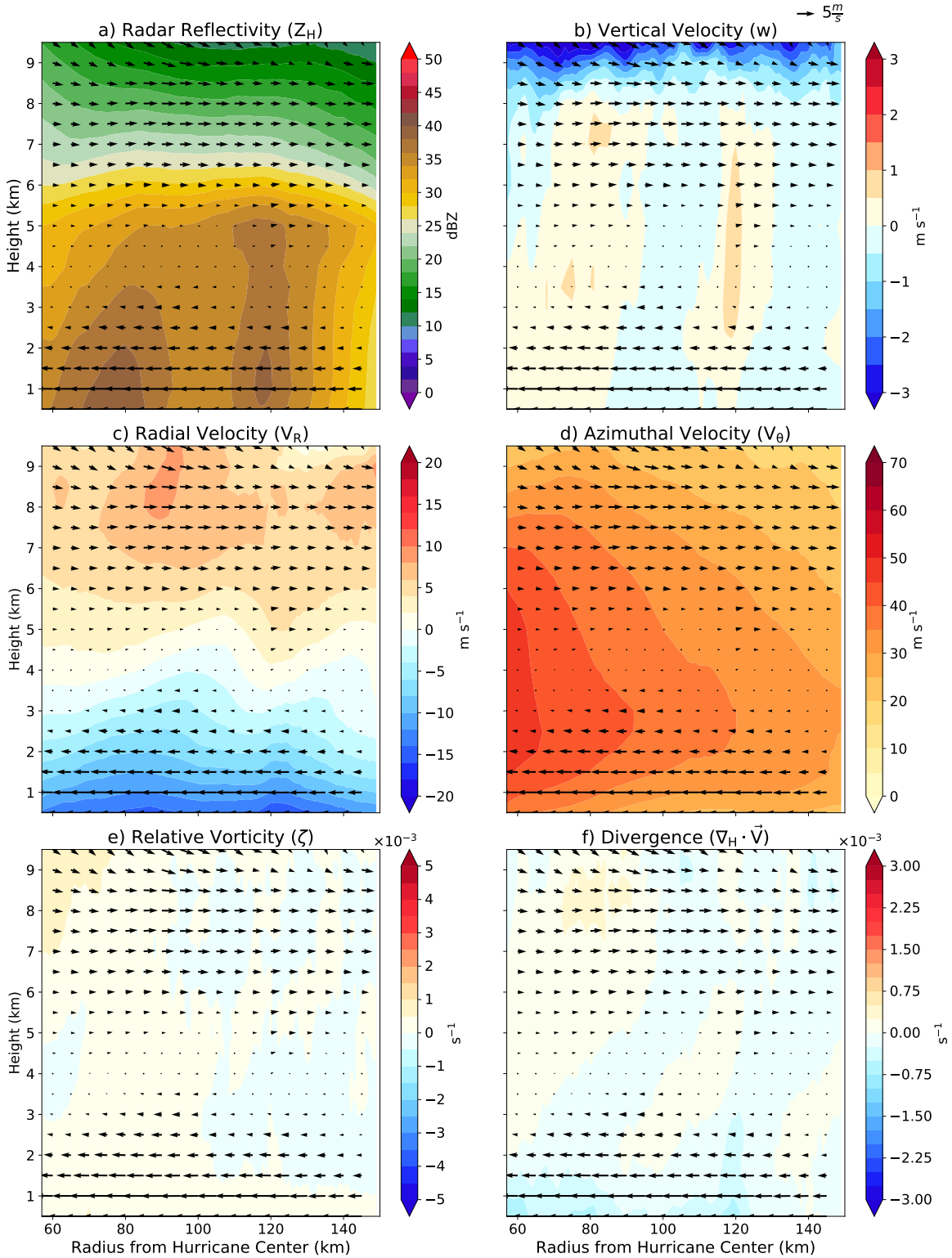
Downshear Left Outer Rainband DDA-Mean Azimuthal-Mean Variables
a) Radar Reflectivity (Z_H)
b) Vertical Velocity (w)
$5\frac{m}{s}$
c) Radial Velocity (V_R)
d) Azimuthal Velocity (V_θ)
e) Relative Vorticity (ζ)
f) Divergence ($\nabla_H \cdot \vec{V}$)
Height (km)
Radius from Hurricane Center (km)
dBZ
m s^{-1}
s^{-1}
$\times 10^{-3}$

Figure 22: As in Figure 20, but for the outer rainband region.

In summary, the DDA-mean azimuthal-mean vertical profiles were created for radar reflectivity, vertical velocity, radial velocity, azimuthal velocity, relative vorticity, and divergence for the downshear left eyewall, inner rainband, and outer rainband regions of Hurricane Laura. All profiles largely agreed with the conceptual models, although some features were inconsistent or absent. While azimuthal-mean vertical profiles provide insight on the broad kinematics of TCs, they fail to depict perturbations. Outliers also exert too much influence over the final profile and, because TCs are not perfectly circular, rainband features can become blended across radii. Therefore, an EOF analysis is detailed in Chapter 5. The EOF analysis will reveal perturbations for each variable that represent a specified percentage of the variance, resulting in a more thorough analysis of the existing kinematics in Hurricane Laura. These results will be further used to validate the conceptual models described in Chapter 2.

Chapter 5

Results: EOF Analyses

The azimuthal-mean profiles from Chapter 4 provide a general idea of the processes occurring in each region of Hurricane Laura. However, they do not include perturbations. Therefore, pieces of the overall TC structure are missing when azimuthal mean profiles are exclusively used in analyses. An EOF analysis was completed with this dataset to isolate perturbations in each region and quantify how much of the variance they represent.

The results of the EOF analysis for the eyewall, inner rainbands, and outer rainbands are shown in Figures 23–38, Figures 39–56, and Figures 57–72, respectively. These figures contain profiles for convective updrafts, convective downdrafts, stratiform regions, and reflectivity cores. As discussed in Chapter 3, partitioning between convective and stratiform regions was completed based on the strength of the vertical motion, rather than by an echo classification algorithm. The vertical motion cutoff of 2 m s^{-1} is consistent with the findings of other studies (e.g., Steiner et al. 1995; Houze Jr 1997; Didlake and Houze 2013b). Therefore, profiles with vertical velocities of $|>2$ m $s^{-1}|$ are designated as convective and profiles with vertical velocities of $|<2$ m $s^{-1}|$ are designated as stratiform. The stratiform region was further restricted to profiles of <30 dBZ reflectivity maxima to remove weak echoes. Convective updraft (downdraft) profiles exclusively consist of >0 m s^{-1} (<0 m s^{-1}) vertical velocities. Reflectivity core profiles include updrafts and downdrafts and are associated with low-level >40 dBZ reflectivity maxima.

As noted in Chapter 3, two possible solutions exist for a given EOF because of the ambiguity of eigenvectors' sign. For completeness, both solutions are included in this analysis, as they are both valid. Therefore, each analyzed region has two profiles for each EOF. Also noted in Chapter 3, the EOFs were calculated from anomalies, scaled by the square root of the eigenvalues, and added back to the mean profile for ease of interpretation. For each variable, enough EOFs were included to ensure at least 90% of the variance is represented.

5.1 Eyewall Region

5.1.1 Radar Reflectivity

Figure 23a shows the mean convective reflectivity field has a near-40 dBZ magnitude for a considerable depth, indicating the convection is deep in this region. Displayed in Figure 23b, 73% (81%) of the variance in the convective updraft (downdraft) radar reflectivity can be explained by EOF-1, which parallels the mean profile except for its differing values. EOF-2 and EOF-3, shown in Figures 23c–d, collectively explain 19% (13%) of the variance in the convective updraft (downdraft) reflectivity field and exhibit more variation from the mean. That is, there are some instances where reflectivity increases with height in the mid-levels. This feature was also observed in Figure 20a and could signify hydrometeors are melting in the mid-levels, hydrometeors are evaporating before reaching the lower levels, convection is tilted, or it could be a byproduct of hydrometeor size sorting. However, because polarimetric variables are not included in this analysis, the absolute cause cannot be determined. EOF-3 also presents a profile where the reflectivity values steadily decrease with height. This is indicative of a laminar reflectivity structure.

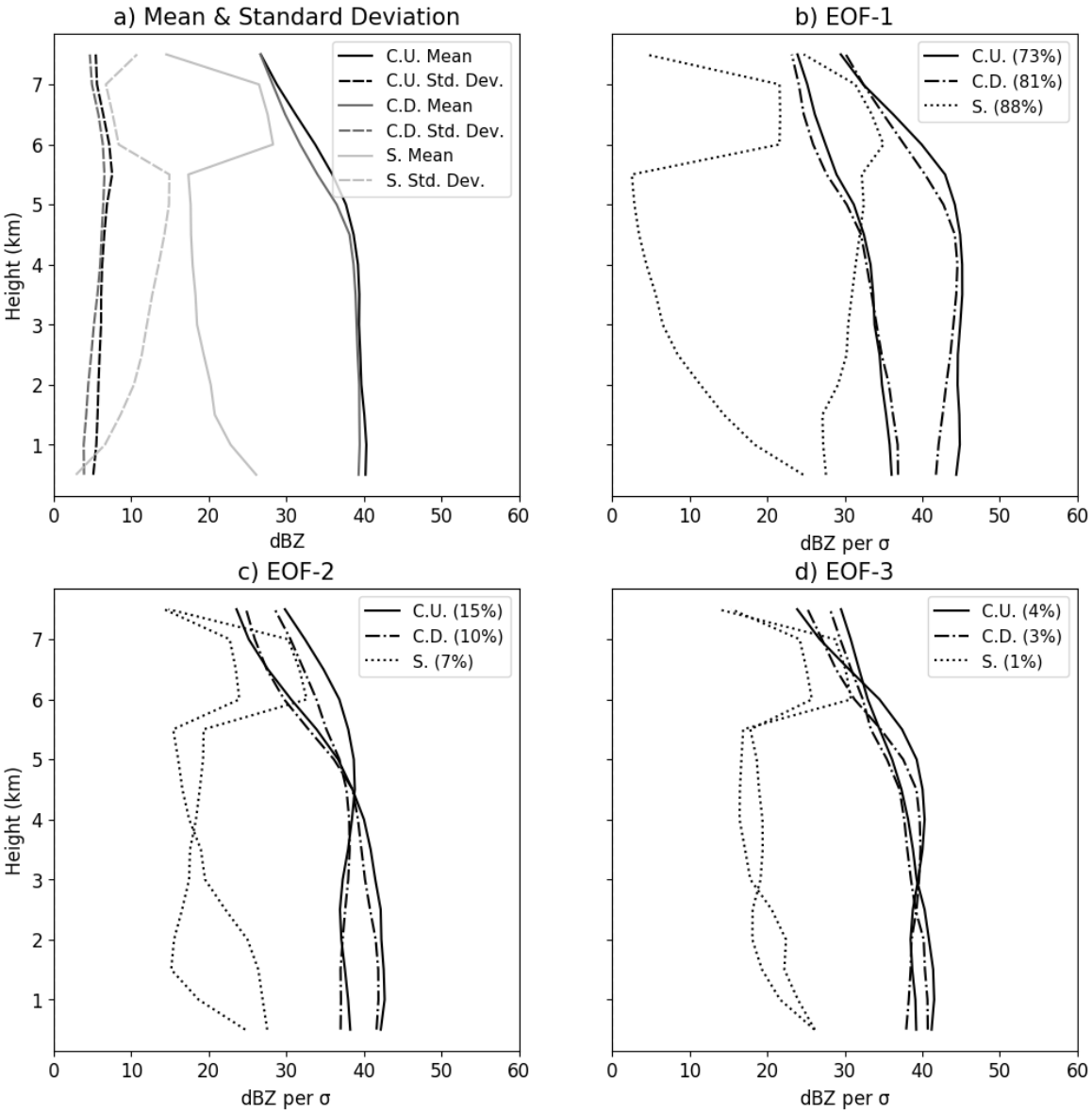

Figure 23: **a)** The mean (solid) and standard deviation (dashed) profiles for downshear left eyewall radar reflectivity (Z_H) in the convective updraft (black; n=177), convective downdraft (gray; n=134), and stratiform (light gray; n=98) regions. **b)** EOF-1 profiles for downshear left eyewall radar reflectivity in the convective updraft (solid), convective downdraft (dashed-dotted), and stratiform (dotted) regions. Corresponding variance explained percentages included in plot legend. **c)** As in b), except for EOF-2. **d)** As in b), except for EOF-3.

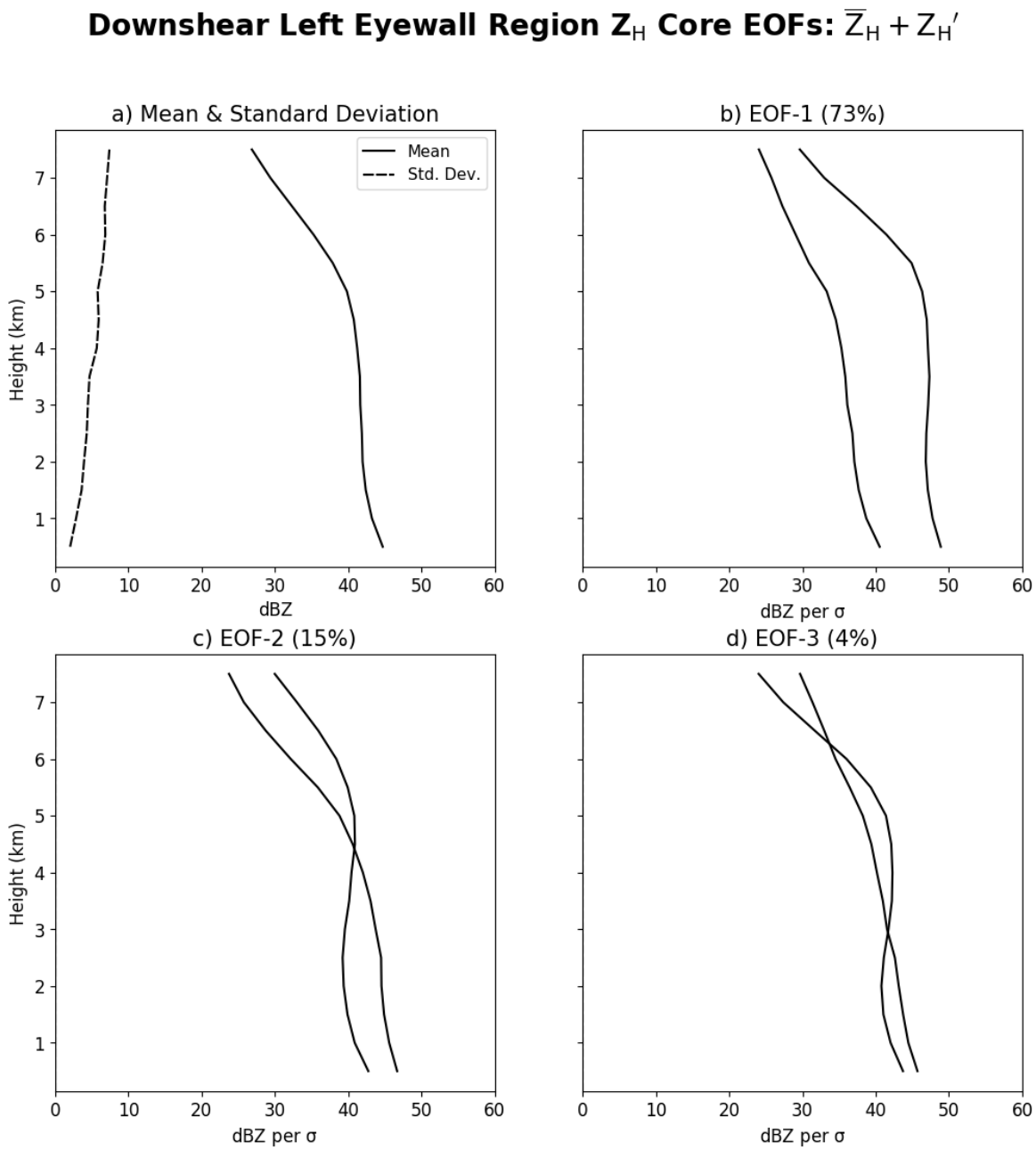

Figure 24: a) The mean (solid) and standard deviation (dashed) profiles for downshear left eyewall radar reflectivity (Z_H) in the reflectivity cores (n=177). **b)** EOF-1 profiles for downshear left eyewall radar reflectivity in the reflectivity cores. Corresponding variance explained percentages included in plot title. **c)** As in b), except for EOF-2. **d)** As in b), except for EOF-3.

Figure 23a also shows the mean vertical profile and standard deviation for radar reflectivity in the stratiform eyewall region. Notably lower in magnitude, the low-level mean reflectivity values are <30 dBZ and decrease in value with height. Above a height of 5.5 km, the mean stratiform reflectivity increases with height, pointing to the widely observed stratiform bright band. In Figure 23b, representing 88% of the variance in stratiform eyewall reflectivity, EOF-1 shows two vastly different profiles. While one profile looks like the mean with lower magnitudes, the other profile shows an increase in reflectivity with height up to the bright band and a decrease in reflectivity above the bright band. That is, precipitation could be evaporating near the surface (i.e., lowering reflectivity values) while hydrometeors are melting in the mid-levels (i.e., raising reflectivity values). Shown in Figures 23c–d, EOF-2 and EOF-3 for the stratiform eyewall represent a combined 8% of the variance in the reflectivity and show variations of the mean profile. This suggests these profiles are produced by similar processes as the mean profile.

The mean, standard deviation, and EOF profiles for the reflectivity field of the eyewall reflectivity cores are shown in Figures 24a–d. Like the mean reflectivity profiles for the eyewall convective regions, the mean reflectivity field for the reflectivity cores shows deep convection up to the melting layer, although the magnitude is slightly higher. EOFs 1 and 2 resemble the mean structure with varying values, and EOFs 2 and 3 capture the increase in reflectivity up to the mid-levels. EOF-3 also shows the structure of steadily decreasing reflectivity with height, suggesting there exists a laminar reflectivity structure in some places.

5.1.2 Vertical Velocity

The mean convective updraft, shown in Figure 25a, increases in magnitude with height. This profile is likely capturing the strong eyewall updraft, which was observed to

strengthen with height in Figure 20b. This structure also supports findings by Zipser (2003) that suggest upper-level latent heat release strengthens updrafts. From Figure 25b, the convective updraft EOF-1 profiles represent 76% of the variance in eyewall convective updraft vertical velocity. One profile shows a steady increase in vertical velocity with height, while the other increases less rapidly before increasing more significantly with height above 6 km. EOFs 2 and 3, displayed in Figures 25c–d, jointly explain 22% of the variance in eyewall convective updraft vertical velocity and resemble the profiles of EOF-1, except with different magnitudes.

Like the mean convective updraft profile, the mean convective downdraft profile, shown in Figure 25a, increases in magnitude with height. Based on Figure 20b, this profile appears to capture the downdraft on the inner edge of the convective updraft. Theorized to result from a combination of forced descent from the eyewall updraft (Willoughby 1998) and evaporative cooling (Jorgensen 1984), the maximum convective downdraft value occurs in the upper levels. Presented in Figure 25b, 92% of the variance in eyewall convective downdraft vertical velocity is explained by EOF-1. Similar to EOF-1 for the convective updraft region, one profile shows an increase in magnitude with height and the other begins strengthening more significantly in the upper levels. Explaining a combined 7% of the variance in eyewall convective downdraft vertical velocity and shown in Figures 25c–d, EOFs 2 and 3 appear to show variations of the downdrafts shown in EOF-1.

Figure 25a displays the mean and standard deviation profiles for the stratiform eyewall region. The mean profile reveals weak upward motion from the lowest level up to the mid-levels and weak downward motion above that. Interestingly, this mean profile shows the reverse of the stratiform structure described by Marks and Houze (1987). However, as explained by Houze Jr (1997), stratiform regions can have a

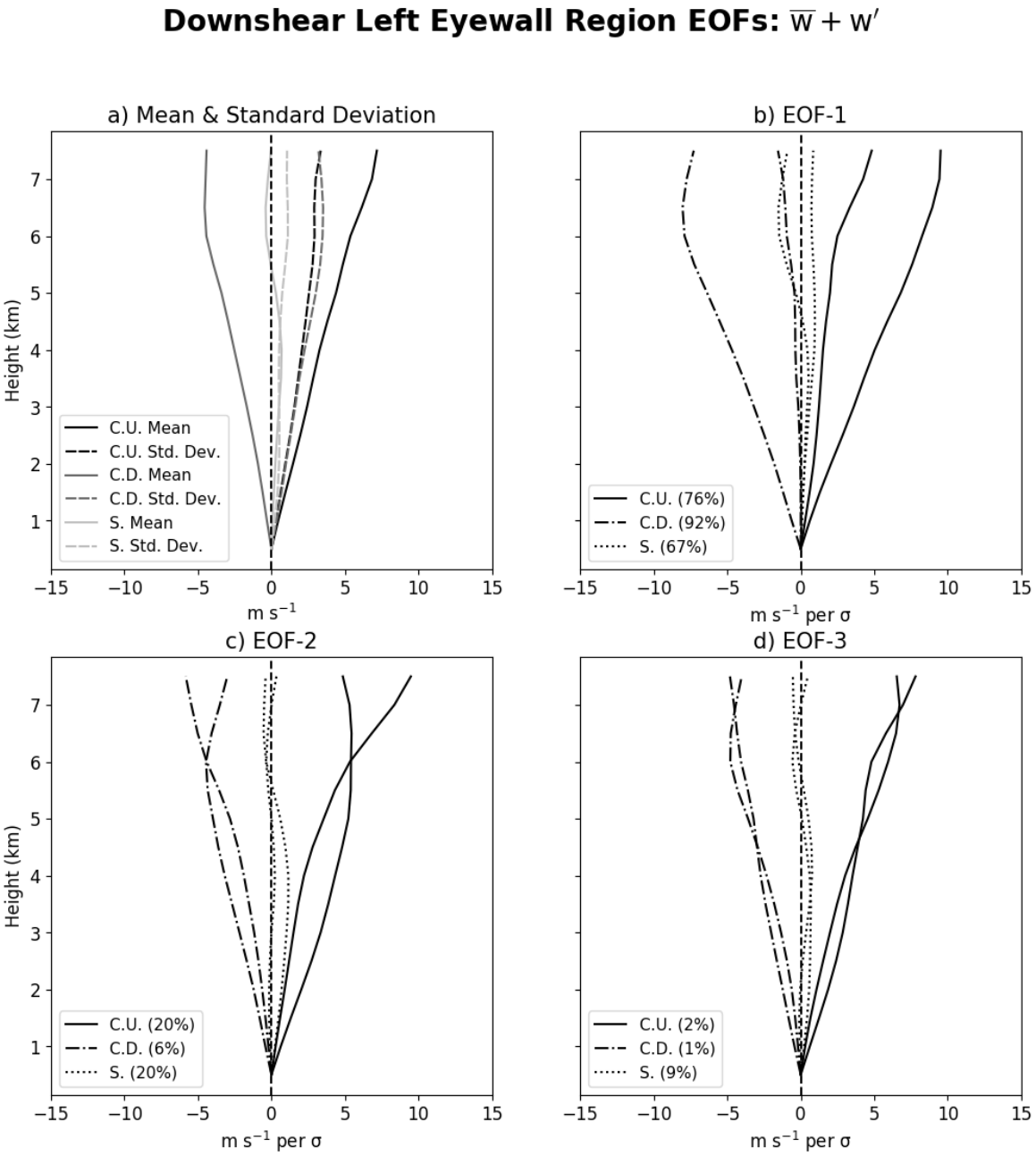

Figure 25: a) The mean (solid) and standard deviation (dashed) profiles for downshear left eyewall vertical velocity (w) in the convective updraft (black; n=133), convective downdraft (gray; n=85), and stratiform (light gray; n=21) regions. **b)** EOF-1 profiles for downshear left eyewall vertical velocity in the convective updraft (solid), convective downdraft (dashed-dotted), and stratiform (dotted) regions. Corresponding variance explained percentages included in plot legend. **c)** As in b), except for EOF-2. **d)** As in b), except for EOF-3.

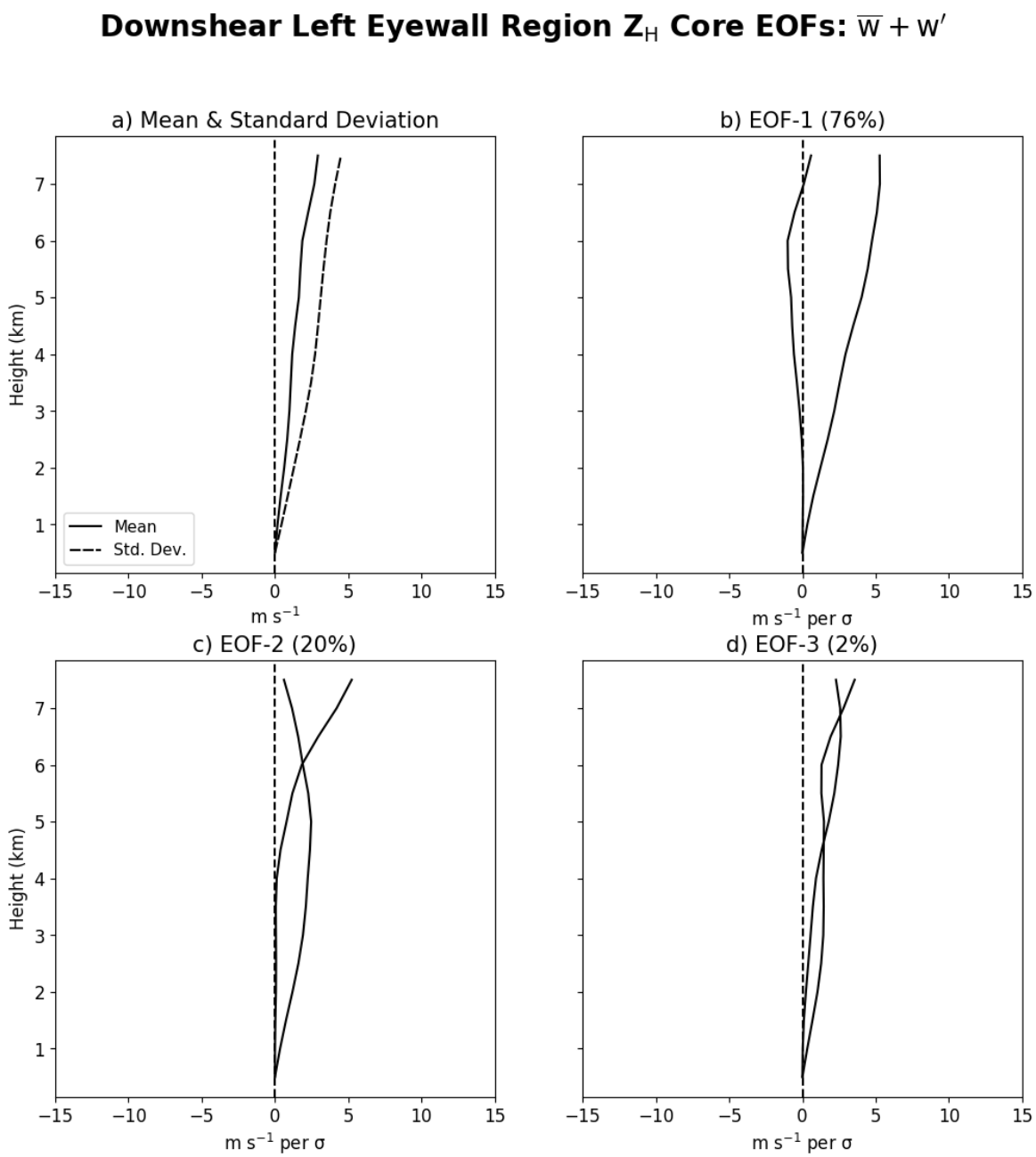

Figure 26: a) The mean (solid) and standard deviation (dashed) profiles for downshear left eyewall vertical velocity (w) in the reflectivity cores (n=133). **b)** EOF-1 profiles for downshear left eyewall vertical velocity in the reflectivity cores. Corresponding variance explained percentages included in plot title. **c)** As in b), except for EOF-2. **d)** As in b), except for EOF-3.

conglomeration of drafts, validating the findings of this analysis. It should be noted that only 21 stratiform eyewall profiles were used in this analysis, as stratiform eyewall regions are scarce, which is a relatively small sample size. Therefore, these results should be used with caution. Displayed in Figure 25b, EOF-1 represents 67% of the variance. One of the EOF-1 profiles resembles the mean, only it is more amplified. The other profile shows a columnar weak updraft. EOF-2 is displayed in Figure 25c and represents 20% of the variance. One profile resembles the mean with an amplified updraft, while the other profile shows a weak downdraft in the lower levels, a weak updraft in the mid-levels, and another weak downdraft in the upper levels. From Figure 25d, the mean profile shape is also represented in EOF-3, which explains 9% of the variance. Overall, the stratiform eyewall structure described by Marks and Houze (1987) is not prominent, which could be due to this analysis being performed on the downshear left quadrant. The only stacked downdraft-updraft structure is evident in EOF-2, where the transitions from downdraft to updraft occur at lower and higher heights than expected.

Figure 26a displays the mean and standard deviation for vertical velocity in the eyewall reflectivity cores. The mean structure shows an updraft that increases in magnitude with height, like the convective updrafts, although its overall magnitude is lower. Explaining 76% of the variance and displayed in Figure 26b, the first EOF shows both a profile that resembles the mean structure as well as a deep downdraft that transitions to an updraft in the mid- to upper levels. This reveals the eyewall reflectivity cores (i.e., low-level reflectivity maxima) are associated with both updrafts and downdrafts. Based on explanations from Didlake and Houze (2013b) and the EOF-1 vertical velocity structure, these downdrafts could be associated with decaying convection, especially for profiles close to the upshear quadrants. Shown in Figure 26c, EOF-2 represents 20% of the variance and shows a profile of near-zero vertical motion

that begins increasing significantly in the mid-levels. The other EOF-2 profile shows an updraft that increases with height, maximizes in the mid-levels, and weakens with height. Lastly, from Figure 26d, EOF-3 shows variations of an updraft and explains 2% of the variance.

5.1.3 Radial Velocity

From Figure 27a, the mean eyewall convective updraft and downdraft profiles show low-level radial inflow and upper-level radial outflow, where the magnitude of the inflow (outflow) is higher for the convective downdraft (updraft) profile. Embodying the secondary circulation, this profile agrees with the conceptual models of Section 2.1.1. Explaining 51% of the variance in eyewall convective updraft radial velocity and shown in Figure 27b, EOF-1 shows two variations of the mean radial velocity structure with differing depths of radial inflow. Namely, there is shallow radial inflow associated with deeper and stronger outflow, and vice versa. For the convective downdraft region, the two EOF-1 profiles have nearly identical low-level inflow, while the upper-level outflow varies in strength. The depth of the inflow for the convective downdraft profiles is also less varied. These profiles represent 48% of the variance. Displayed in Figure 27c and similar to the EOF-1 convective updraft radial velocity structure, the EOF-2 structures for the convective regions reveal varying depths and values of low-level radial inflow and upper-level outflow. The convective updraft and convective downdraft structures for this EOF represent 35% and 37% of the variance, respectively. Shown in Figure 27d and explaining 9% and 7% of the variance, the EOF-3 convective updraft and downdraft radial velocity profiles resemble the mean structure. The profiles for each convective region are nearly identical, except for differences in magnitude near the surface.

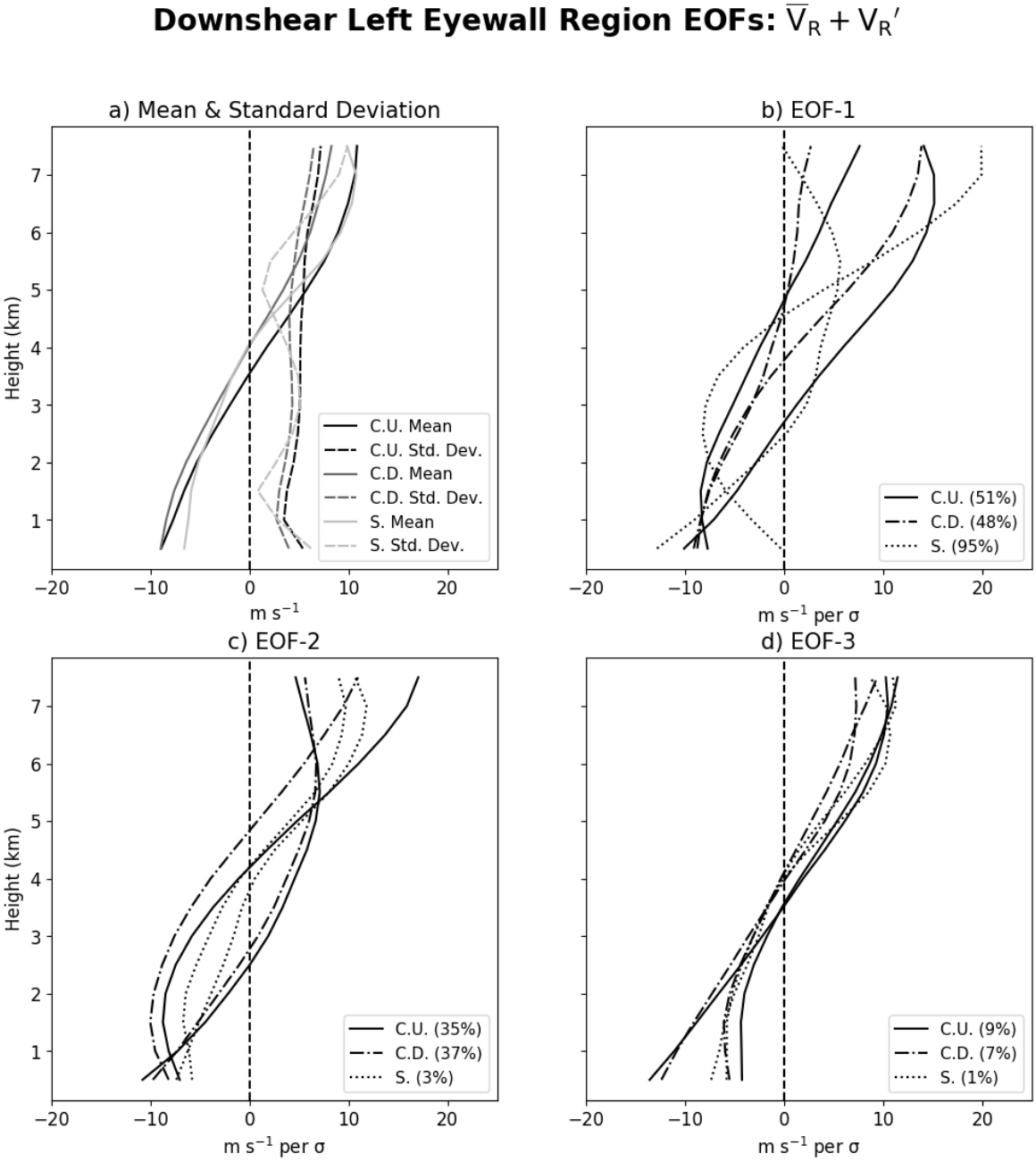

Figure 27: As in Figure 25, except for radial velocity.

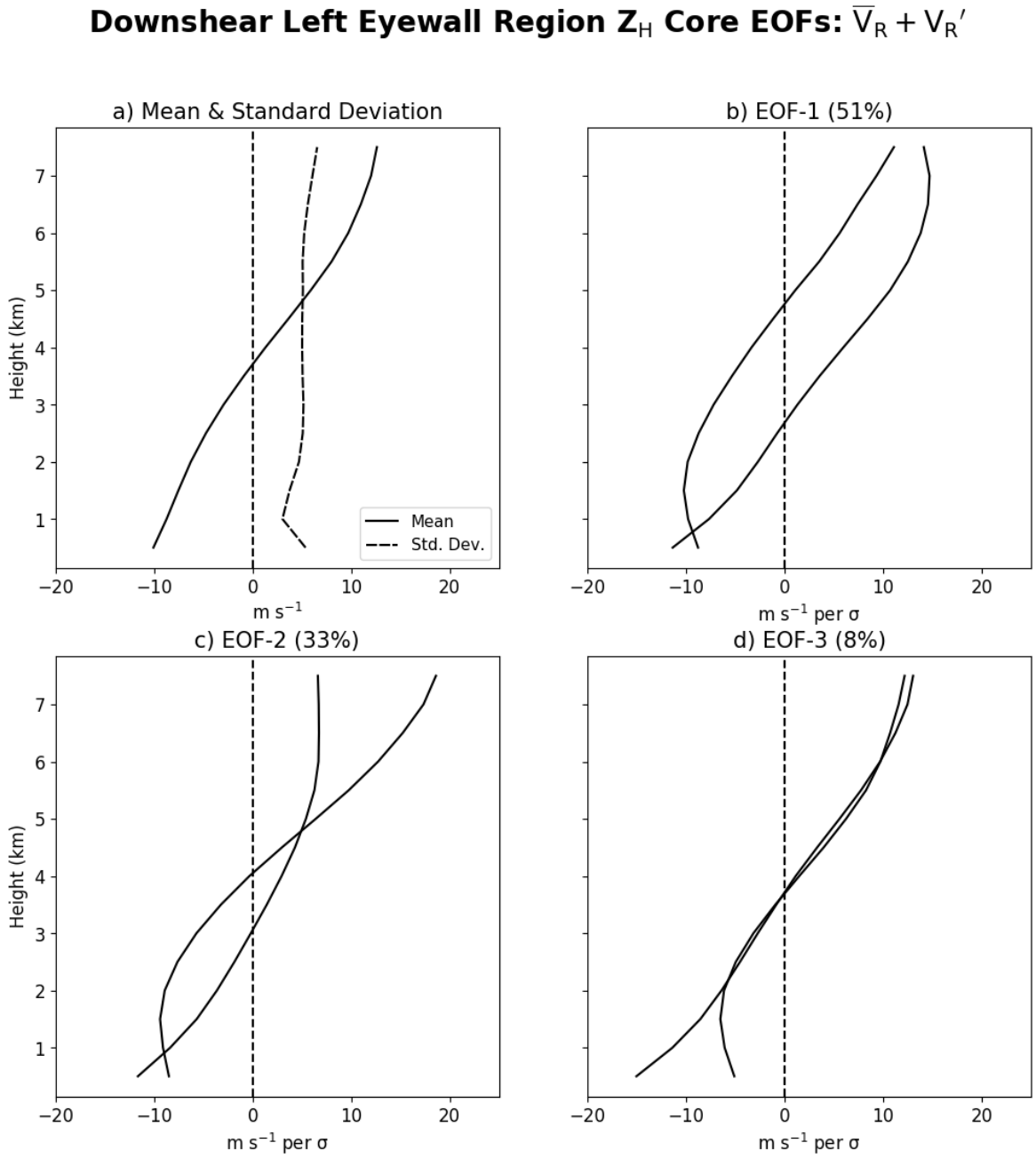

Figure 28: a) The mean (solid) and standard deviation (dashed) profiles for downshear left eyewall radial velocity (w) in the reflectivity cores (n=124). **b)** EOF-1 profiles for downshear left eyewall radial velocity in the reflectivity cores. Corresponding variance explained percentages included in plot title. **c)** As in b), except for EOF-2. **d)** As in b), except for EOF-3.

The mean stratiform eyewall radial velocity profile, also shown in Figure 27a, is similar in structure to the mean convective radial velocity profiles. This result is expected, as the secondary circulation is not limited to convective regions. Like the stratiform eyewall vertical velocity, only 21 stratiform eyewall radial velocity vertical profiles were available for this analysis. Therefore, the results should be considered with caution. The first EOF for the stratiform eyewall radial velocity, displayed in Figure 27b, explains 95% of the variance, indicating most stratiform eyewall radial velocity perturbation structures resemble it. As expected, the two profiles have low-level inflow and upper-level outflow. However, the velocities and inflow depth vary noticeably. That is, the profile with more shallow inflow sees its strongest velocities near the surface as inflow, while the profile with deeper inflow sees its strongest velocities in the upper levels as outflow. Shown in Figures 27c–d, EOFs 2 and 3 represent a combined 4% of the variance and show variations of the mean low-level inflow and upper-level outflow structure.

The mean profile of radial velocity in the reflectivity cores, displayed in Figure 28a, reveals a similar structure to that of the convective draft regions. That is, low-level inflow that transitions to upper-level outflow in the mid-levels. The consequent EOFs, presented in Figures 28b–d, all exhibit variations of low-level inflow and upper-level outflow, where, as observed in the convective draft regions, varying depths of inflow exist as well as varying velocity values.

5.1.4 Azimuthal Velocity

Shown in Figure 29a, the mean azimuthal velocity profiles for the convective updraft and downdraft regions have slightly different magnitudes and nearly identical shapes, where the maximum azimuthal velocity occurs in the lower levels. The placement of the azimuthal velocity maximum and the decreasing trend with height does agree with the

conceptual model of Marks and Houze (1987), except the magnitude of the maximum in this analysis is stronger by more than 15 m s^{-1}. Though, this discrepancy is likely owed to structural and intensity differences in the analyzed storms as well as differences in the data collection techniques. From Figure 29b, EOF-1 explains 63% of the variance in the convective updraft azimuthal velocity and shows two profiles that roughly parallel the shape of the mean, where one has lower values and the other has higher values. For the convective downdraft region, EOF-1 has a similar interpretation, although its values are lower than those of the convective updraft region. This suggests the azimuthal velocity is stronger in the convective updraft region than in the convective downdraft region. In addition to a profile that resembles the mean, EOF-2, displayed in Figure 29c, offers a slightly different azimuthal velocity vertical profile shape for both the convective updraft and downdraft regions. This profile exhibits a relatively constant azimuthal velocity through the mid-levels rather than a notable decrease. Therefore, this profile shows there are instances in the eyewall region where the vertical gradient in azimuthal velocity is relatively weak. EOF-2 explains 22% and 28% of the variance in eyewall convective updraft and downdraft azimuthal velocity, respectively. From Figure 29d, variations of the profiles shown in EOFs 1 and 2 are displayed in EOF-3 and explain 8% and 6% of the variance for the convective updraft and downdraft regions, respectively.

From Figure 29a, the mean stratiform azimuthal velocity profile is of similar shape and magnitude to the mean convective profiles. This is expected as, based on angular momentum requirements, the whole downshear left eyewall region should have strong azimuthal velocity. Like the vertical velocity and radial velocity stratiform eyewall profiles, the azimuthal velocity stratiform eyewall profiles only include 21 profiles, which may not be enough to accurately represent the stratiform eyewall. Displayed in Figure

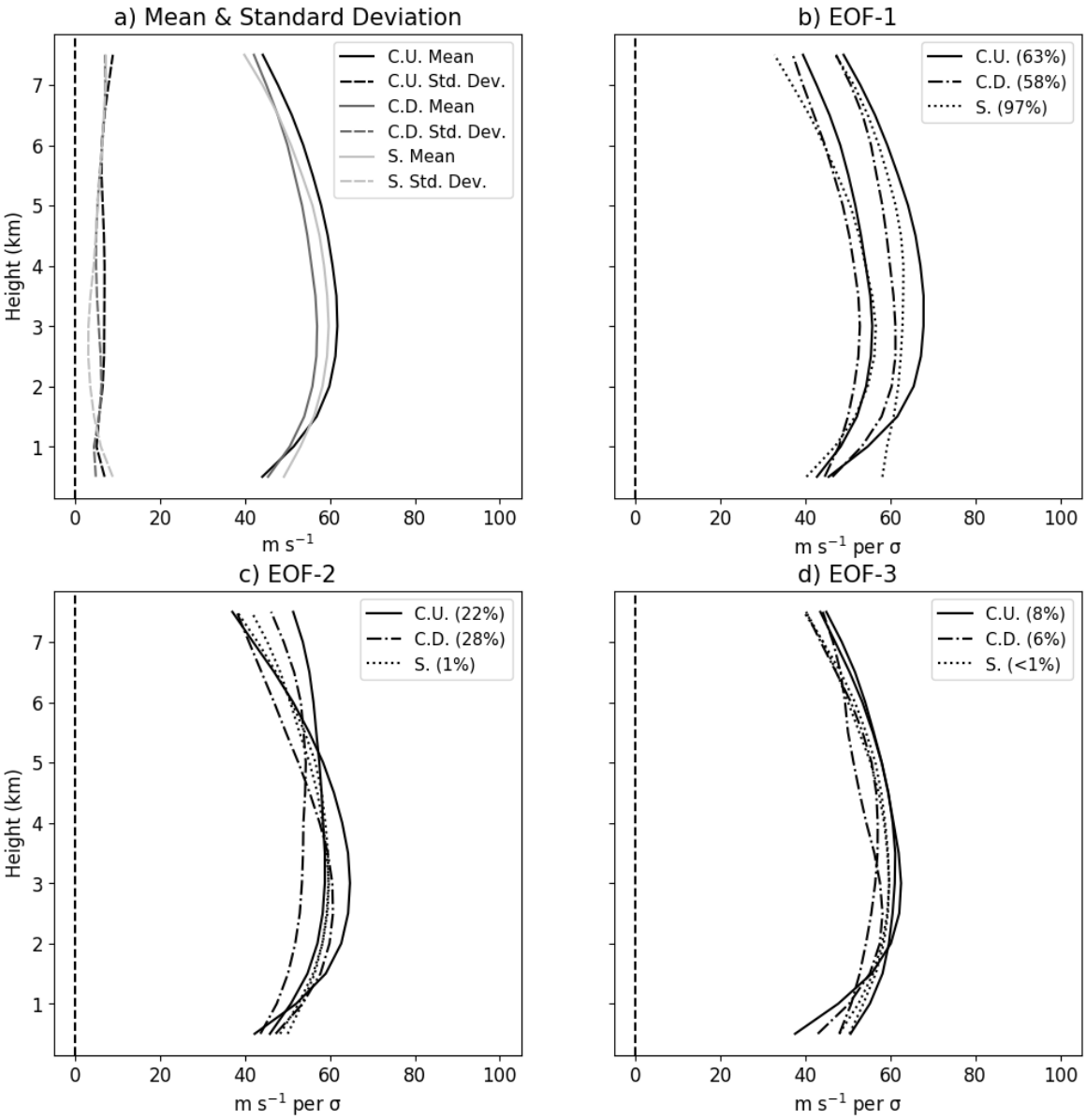

Figure 29: As in Figure 25, except for azimuthal velocity.

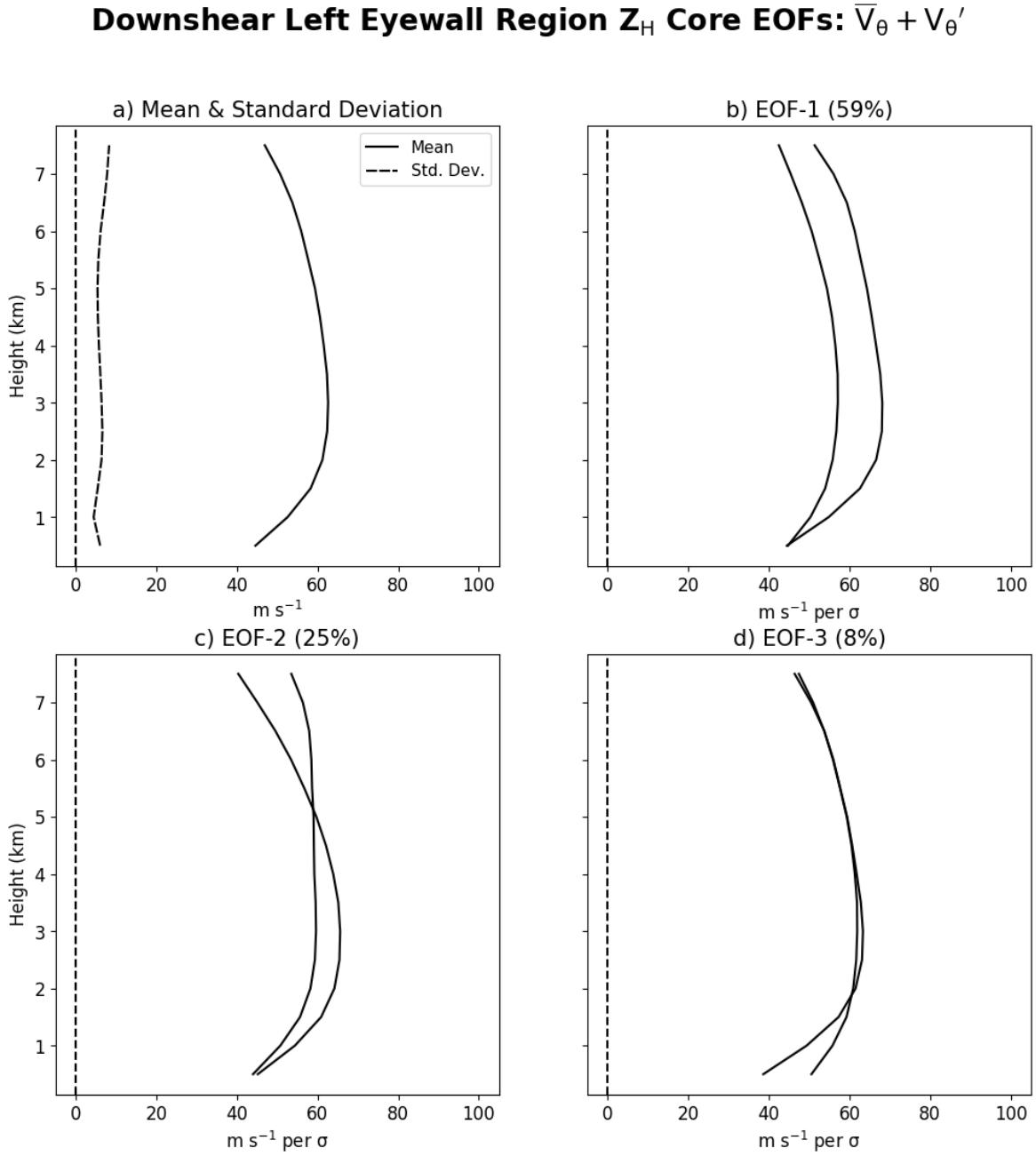

Figure 30: As in Figure 28, except for azimuthal velocity.

29b, 97% of the variance in stratiform eyewall azimuthal velocity can be explained by the profiles in EOF-1. These profiles maintain the relative shape of the mean, where one profile is lower in magnitude and the other is higher. From Figures 29c–d, EOFs 2 and 3 represent less than 2% of the variance and resemble the mean profile. These EOFs suggest the vertical structure of the stratiform eyewall azimuthal velocity is relatively uniform and does not differ much from the mean.

The mean, standard deviation, and EOF profiles for the azimuthal velocity in the reflectivity cores, displayed in Figures 30a–d, resemble those of the convective updraft regions. Namely, the mean profile exhibits a low-level azimuthal velocity maximum before the velocity decreases with height. The EOFs further present profiles that are structurally similar to the EOFs for the convective updraft region. That is, there are profiles that resemble the mean as well as profiles with weak vertical azimuthal velocity gradients.

5.1.5 Relative Vorticity

From Figure 31a, the mean profile for the eyewall convective updraft vertical vorticity shows maximum cyclonic vorticity near the surface that decreases in the mid-levels before increasing in the upper levels. Shown in Figure 31b, EOF-1 explains 53% of the variance in eyewall convective updraft vertical vorticity, where one of the profiles resembles the shape of the mean profile, except its minimum and maximum values are amplified. The other profile shows low- to mid-level weak cyclonic vorticity that transitions to anticyclonic vorticity in the upper levels. EOF-2, displayed in Figure 31c, similarly reveals profiles of mostly cyclonic vorticity, where one becomes anticyclonic in the upper levels. The profiles of EOFs 3 and 4, shown in Figures 31d and 32a, are likewise mostly cyclonic. In general, these EOFs show the convective eyewall updrafts

are largely associated with cyclonic vorticity, although the magnitude and vertical structure vary considerably.

While the mean eyewall convective downdraft vertical vorticity profile, displayed in Figure 31a, has a similar shape to that of the convective updraft, its overall magnitude is lower. This indicates the convective updrafts transport higher mean cyclonic vorticity than the downdrafts. EOF-1, explaining 56% of the variance and presented in Figure 31b, shows two profiles with weak cyclonic vorticity in the low- to mid-levels. Above the mid-levels, one profile increases in cyclonic vorticity with height while the other transitions to anticyclonic vorticity. For EOF-2, in Figure 31c, the convective downdraft profiles represent 21% of the variance and almost mirror each other. One of the profiles shows nearly columnar anticyclonic vorticity, aside from cyclonic vorticity in the lower and upper levels, while the other shows columnar cyclonic vorticity. Both profiles exhibit their maximum magnitude just above 5 km. Displayed in Figures 31d and 32a, the third and fourth EOFs show profiles of low-level anticyclonic and mid- to upper-level cyclonic vorticity as well as profiles with low-level cyclonic, mid-level anticyclonic, and upper-level cyclonic vorticity. Collectively, EOF-3 and EOF-4 explain 14% of the variance. Compared to the convective eyewall updrafts, the convective downdrafts transport more anticyclonic vorticity.

From Figure 31a, the stratiform eyewall mean vertical vorticity is similar in magnitude to that of the convective updraft region, implying the stratiform eyewall profiles are in close proximity to the convective updrafts. Like the other variables, only 16 stratiform eyewall vertical vorticity profiles could be used in this analysis. Therefore, these results should be used with caution. From Figures 31b–d and Figure 32a, EOFs 1-4 show cyclonic vorticity profiles of varying shape and magnitude. Since the stratiform

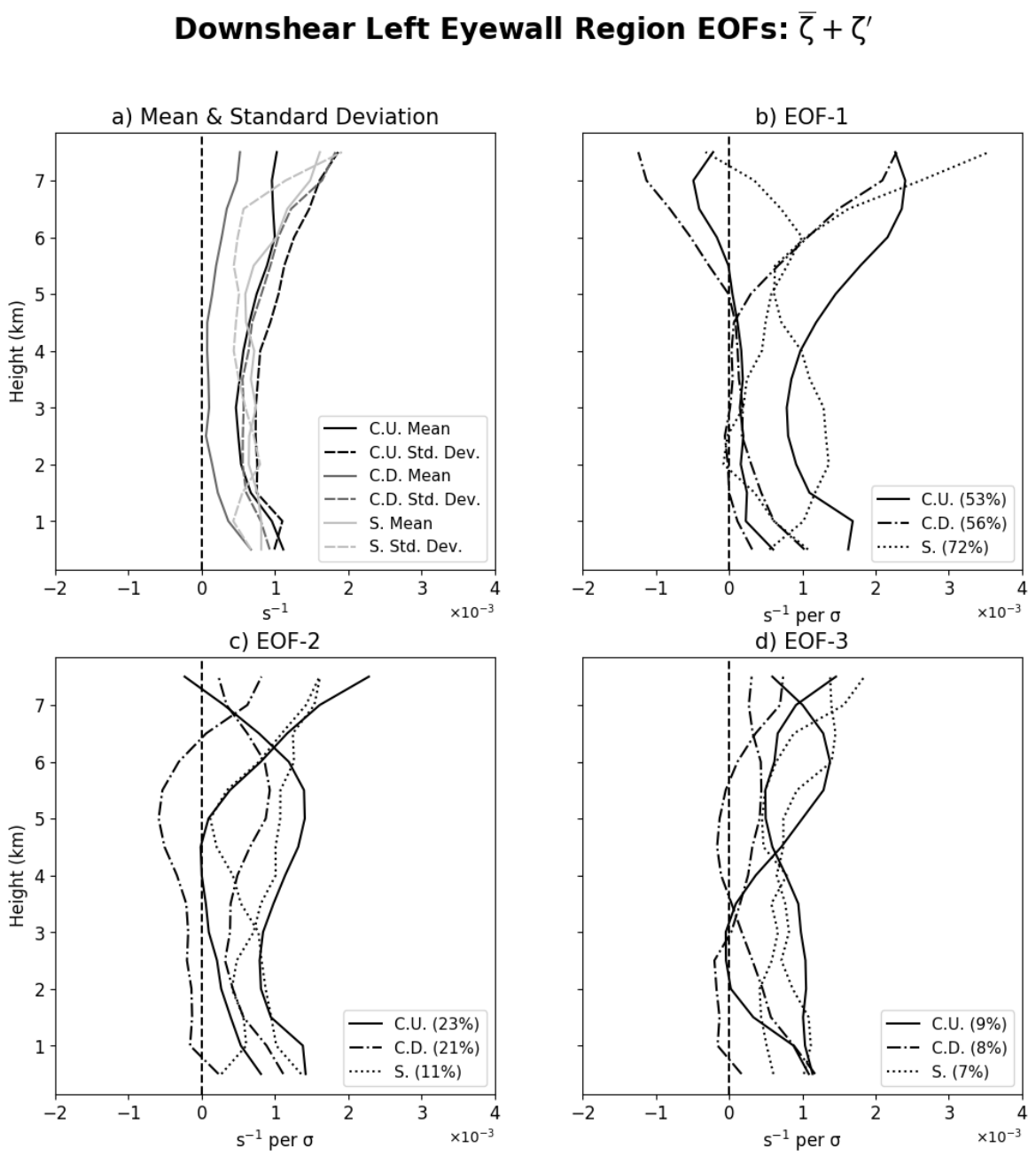

Figure 31: a) The mean (solid) and standard deviation (dashed) profiles for downshear left eyewall relative vorticity (ζ) in the convective updraft (black; n=95), convective downdraft (gray; n=80), and stratiform (light gray; n=16) regions. **b)** EOF-1 profiles for downshear left eyewall relative vorticity in the convective updraft (solid), convective downdraft (dashed-dotted), and stratiform (dotted) regions. Corresponding variance explained percentages included in plot legend. **c)** As in b), except for EOF-2. **d)** As in b), except for EOF-3.

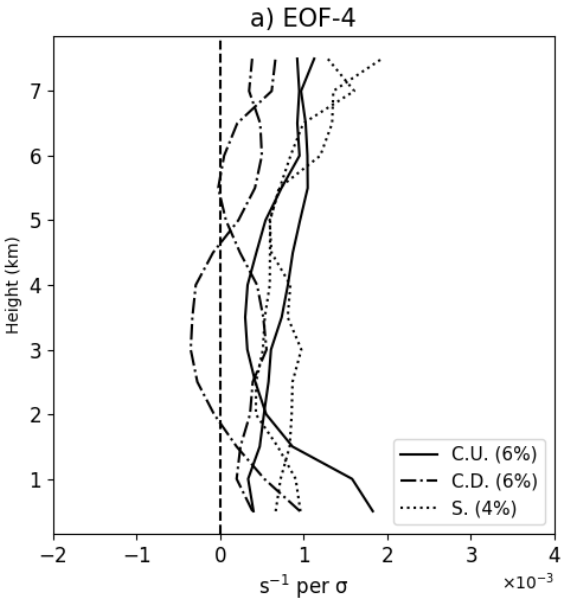

Figure 32: A continutation of the EOFs from Figure 31, where **a)** is EOF-4.

eyewall region largely has weak updrafts, it is possible these updrafts are advecting positive vorticity in concert with the convective updrafts or positive vorticity is being advected into the stratiform regions.

Figures 33a–d and Figure 34a display the mean, standard deviation, and EOF profiles for the relative vorticity associated with the eyewall reflectivity cores. Mean cyclonic vorticity is evident with a minimum in the mid-levels. EOF-1, explaining 60% of the variance, shows one profile with low-level cyclonic vorticity that transitions to anticyclonic vorticity in the mid-levels and another vorticity profile that is exclusively cyclonic. The remaining EOF profiles show cyclonic vorticity except for one, where weak anticyclonic vorticity exists in the mid-levels. Like in the other regions, the relative vorticity vertical structure in the eyewall reflectivity cores varies considerably.

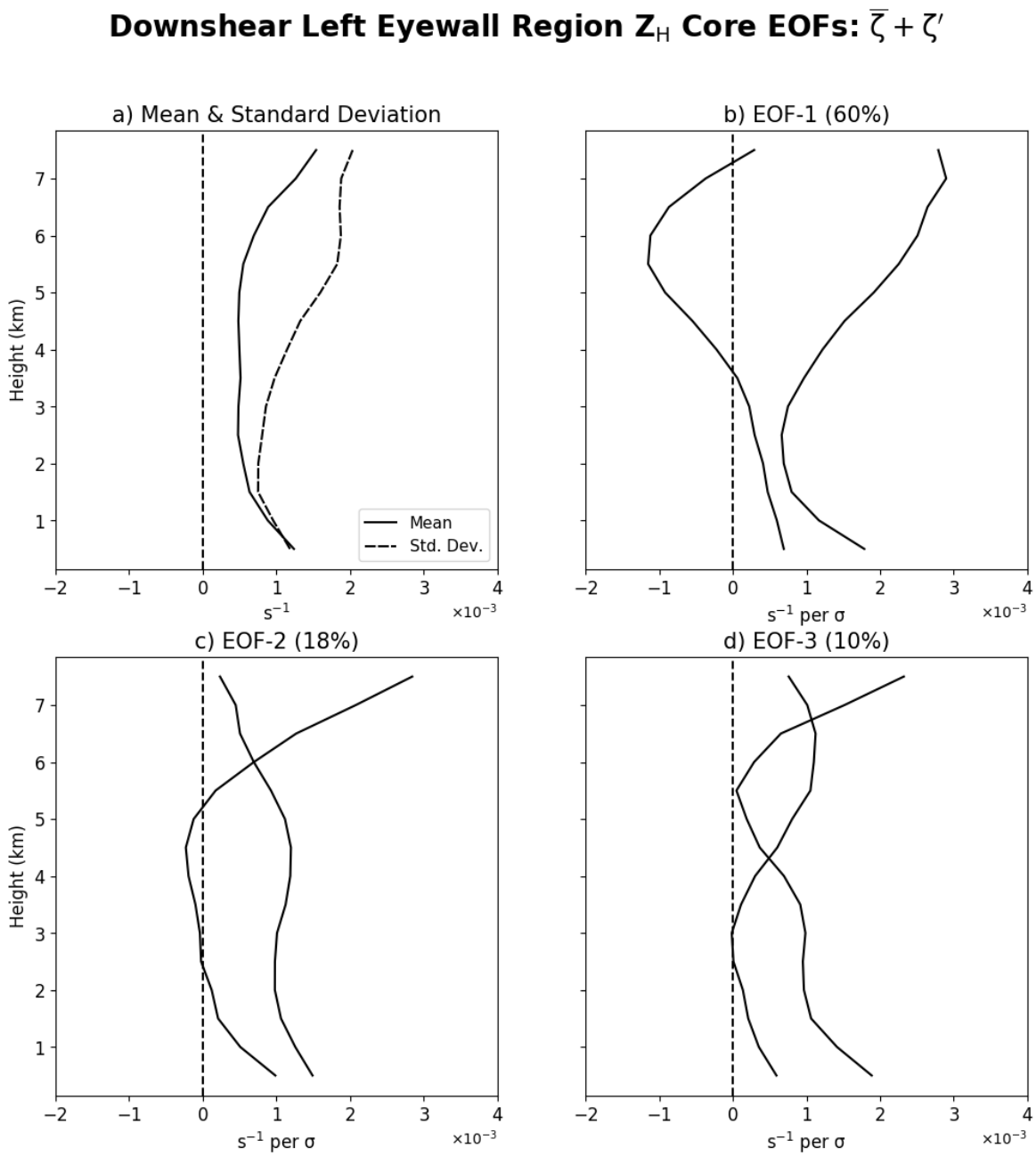

Figure 33: a) The mean (solid) and standard deviation (dashed) profiles for downshear left eyewall relative vorticity (ζ) in the reflectivity cores (n=103). **b)** EOF-1 profiles for downshear left eyewall relative vorticity in the reflectivity cores. Corresponding variance explained percentages included in plot title. **c)** As in b), except for EOF-2. **d)** As in b), except for EOF-3.

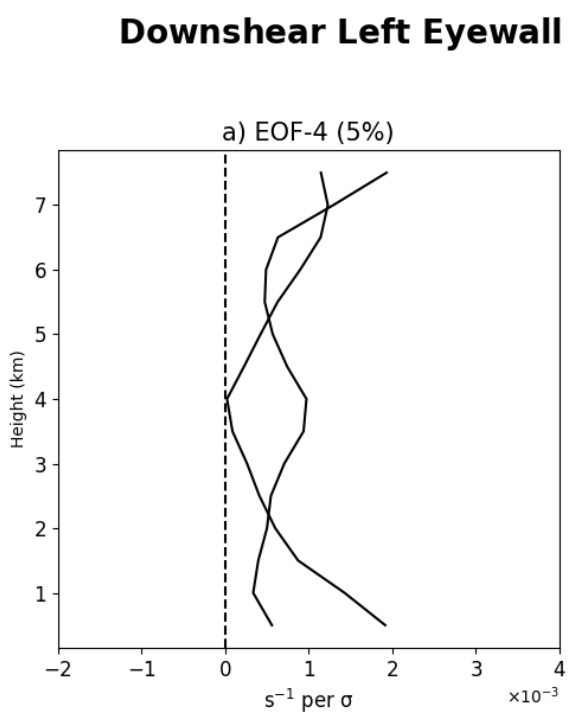

Figure 34: A continutation of the EOFs from Figure 33, where **a)** is EOF-4.

5.1.6 Divergence

Displayed in Figure 35a, the mean eyewall convective updraft divergence profile shows columnar convergence, with a maximum occurring near the surface. Based on mass continuity, this result is expected. That is, in regions of upward motion, horizontal convergence (divergence) would need to occur below (above) the updraft. While mean divergence is not evident in the upper levels of this profile, it likely occurs above the upper extent of this analysis. EOF-1, explaining 52% of the variance and displayed in Figure 35b, shows one exclusively convergent profile and another profile of low- to mid-level convergence and upper-level divergence. Based on Figure 25, this divergence likely corresponds to updraft weakening in the upper levels. From Figures 35c–d and Figures 36a–b, EOFs 2-5 show variations of columnar convergence.

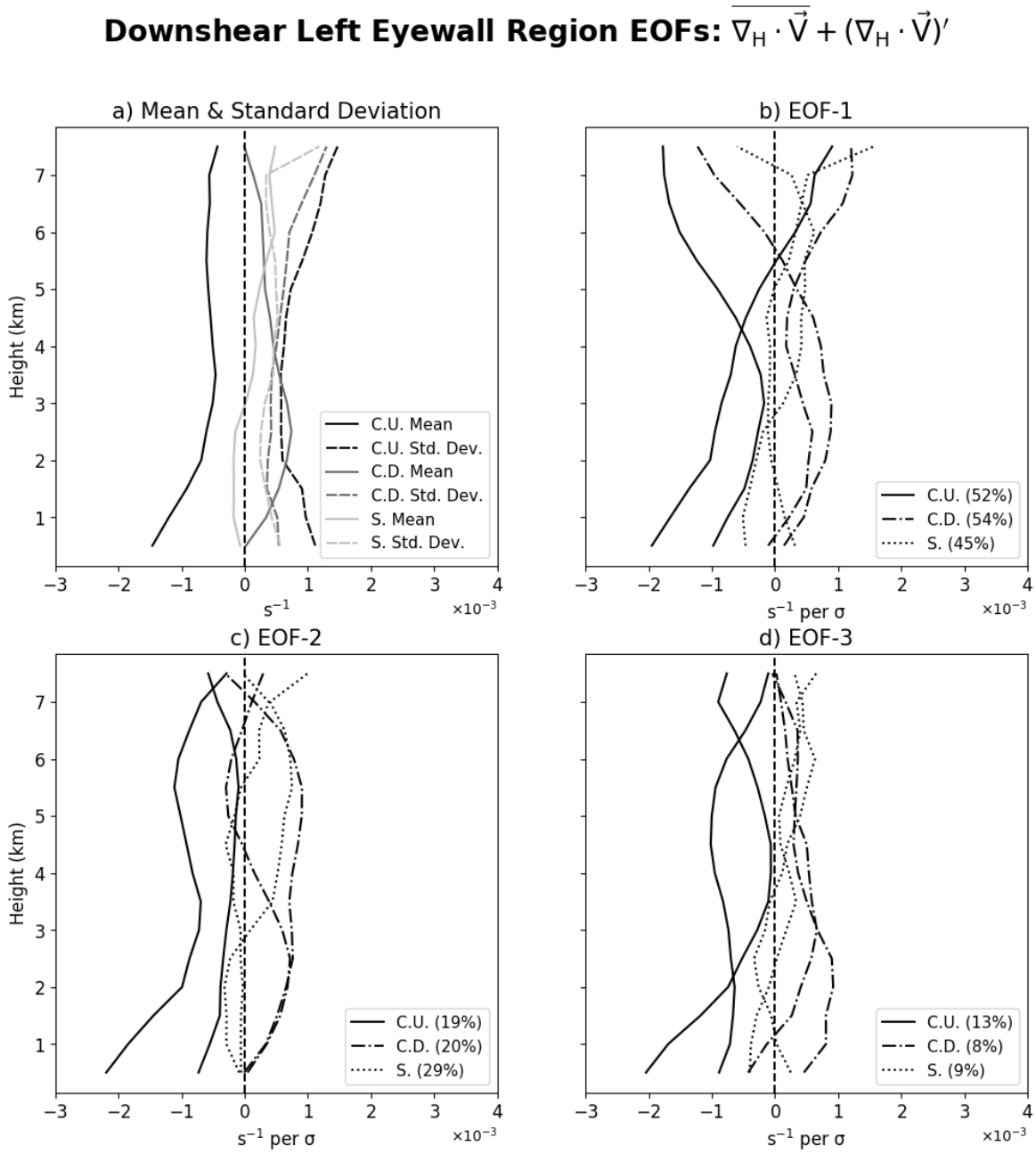

Figure 35: a) The mean (solid) and standard deviation (dashed) profiles for downshear left eyewall divergence ($\nabla_H \cdot \vec{V}$) in the convective updraft (black; n=92), convective downdraft (gray; n=77), and stratiform (light gray; n=18) regions. **b)** EOF-1 profiles for downshear left eyewall divergence in the convective updraft (solid), convective downdraft (dashed-dotted), and stratiform (dotted) regions. Corresponding variance explained percentages included in plot legend. **c)** As in b), except for EOF-2. **d)** As in b), except for EOF-3.

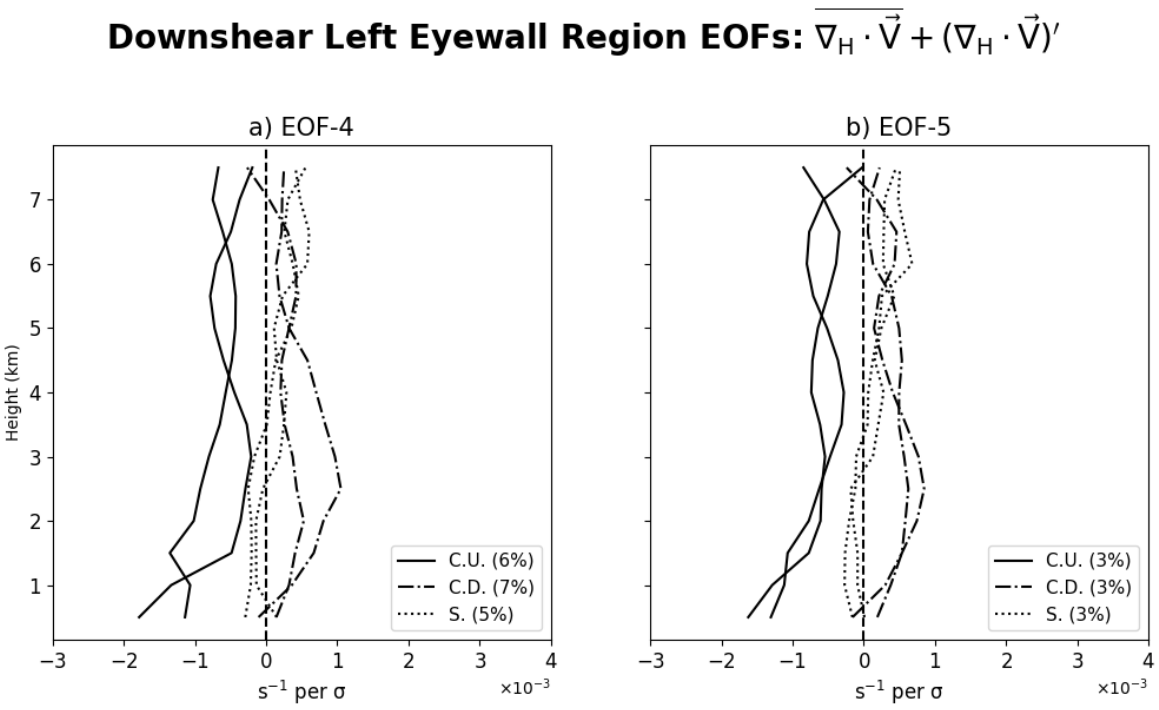

Figure 36: A continutation of the EOFs from Figure 35, where **a)** is EOF-4 and **b)** is EOF-5.

Based on mass continuity logic, the convective downdraft region should have low-level mean divergence and upper-level mean convergence. Sure enough, in Figure 35a, low-level divergence is observed in the mean convective downdraft profile. Upper-level convergence, however, is not observed. Like the convective updraft region, the vertical profile likely does not extend high enough to observe upper-level convergence. From Figure 35b, the EOF-1 profiles show mostly columnar divergence, except upper-level convergence is evident in one of them. Similar to the upper-level divergence in the convective updraft region, this upper-level convergence likely corresponds to upper-level downdraft weakening, based on Figure 25. EOF-1 represents 54% of the variance. EOFs 2-5, displayed in Figures 35c–d and Figures 36a–b, show varying profiles of low-level divergence, and in some cases upper-level convergence, and explain a combined 38% of the variance.

From Figure 35a, the mean divergence profile for the stratiform eyewall shows weak convergence in the lower levels and weak divergence above it. This points to the existence of a mean shallow or weakening updraft. Indeed, Figure 25a does show shallow mean upward motion in the lower levels. Representing 45% of the variance and shown in Figure 35b, EOF-1 displays a profile of low-level convergence, mid- to upper-level divergence, and upper-level convergence. This implies there exists a weak low-level updraft and a weak upper-level downdraft, which is confirmed by Figures 25a–c. The other profile displays near-surface divergence, mid-level convergence, and upper-level divergence. Based on mass continuity, this profile suggests there is a low-level downdraft and a mid-level updraft, which is also confirmed by Figure 25c. From Figures 35c–d, EOFs 2 and 3 show variations of EOF-1 and represent 29% and 9% of the variance in stratiform eyewall divergence, respectively. EOFs 4 and 5, displayed in Figures 36a–b, represent a combined 8% of the variance and display variations of low-level convergence and mid- to upper-level divergence, like the mean profile.

Rather unsurprisingly, from Figure 37a, mean convergence is evident in the reflectivity cores. However, from Figure 37b, EOF-1 shows a profile of low-level convergence and upper-level divergence as well as a profile of near-surface convergence, low- to mid-level divergence, and upper-level convergence. These profiles each explain 61% of the variance. Shown in Figure 37c, one EOF-2 profile presents mostly columnar convergence with upper-level divergence, while the other profile shows low- and upper-level convergence and mid-level divergence. These profiles represent 13% of the variance. EOFs 3 and 4, displayed in Figure 37d and Figure 38a, show variations of columnar convergence as well as convergent profiles with low- and upper-level divergence and explain a combined 17% of the variance. These EOFs show the reflectivity cores contain

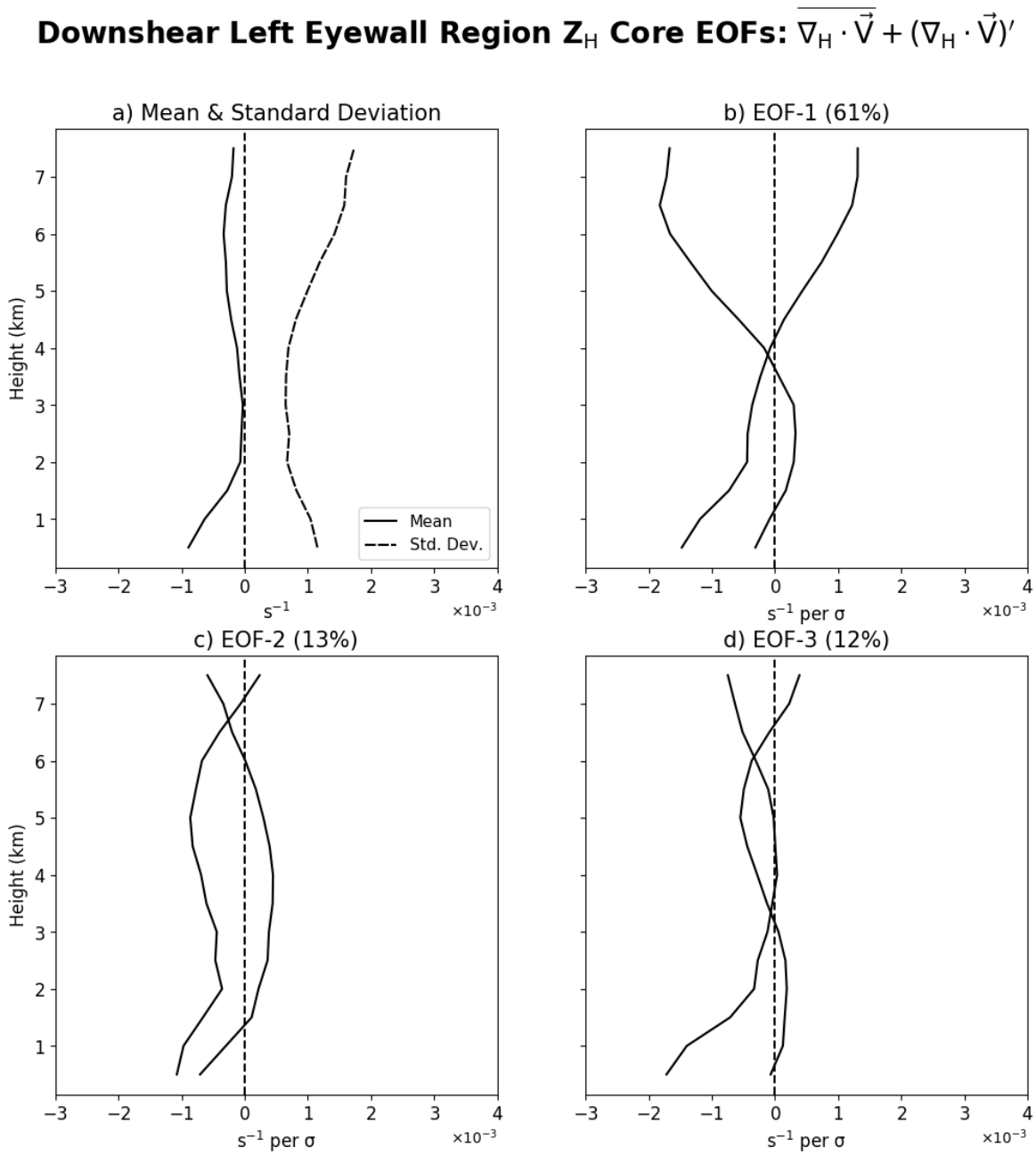

Figure 37: a) The mean (solid) and standard deviation (dashed) profiles for downshear left eyewall divergence ($\nabla_H \cdot \vec{V}$) in the reflectivity cores (n=97). **b)** EOF-1 profiles for downshear left eyewall divergence in the reflectivity cores. Corresponding variance explained percentages included in plot title. **c)** As in b), except for EOF-2. **d)** As in b), except for EOF-3.

Downshear Left Eyewall Region Z_H Core EOFs: $\overline{\nabla_H \cdot \vec{V}} + (\nabla_H \cdot \vec{V})'$

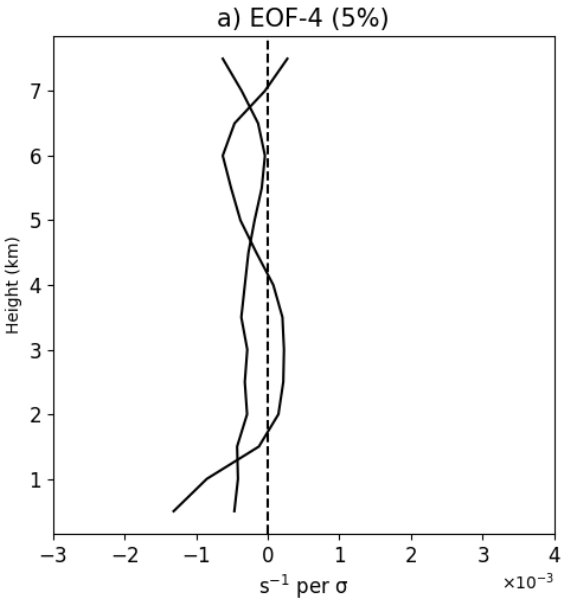

Figure 38: A continutation of the EOFs from Figure 37, where **a)** is EOF-4.

both convergent and divergent profiles, which is expected as updrafts and downdrafts are both present.

5.2 Inner Rainband Region

5.2.1 Radar Reflectivity

The mean reflectivity profiles for the convective updraft and downdraft regions, shown in Figure 39a, are nearly identical. Unlike in the eyewall region, these profiles show a steady decrease in reflectivity with height. The mean vertical profile of reflectivity in Figure 21a looks rather laminar, which is consistent with this steady decrease. Shown in Figure 39b, 49% (54%) of the variance in inner rainband convective updraft (downdraft) reflectivity is represented by the EOF-1 profiles. All of the profiles resemble the mean structure, indicating the majority of the convective profiles in this region have a laminar reflectivity structure. In addition to profiles that resemble the mean structure, the convective updraft and downdraft EOF-2 profiles, displayed in Figure 39c, each have a reflectivity profile that appears to be more upright up to the mid-levels. This hints at the existence of convective cores in the inner rainband region. These profiles explain 24% of the variance for both convective regions. EOF-3, representing 11% of the variance and displayed in Figure 39d, shows similar reflectivity structures to EOF-2. Variations of the slanted and upright reflectivity profiles are also shown in EOFs 4-6 in Figures 40a–c, which collectively represent 10% and 5% of the convective updraft and downdraft variance, respectively.

Unlike the convective regions, from Figure 39a, the mean stratiform inner rainband reflectivity profile shows a steady increase in reflectivity up to its peak between 4-5 km before decreasing with height. This increase in reflectivity with height indicates hydrometeors are likely evaporating before reaching the surface and the reflectivity peak is likely the manifestation of the bright band commonly observed in stratiform

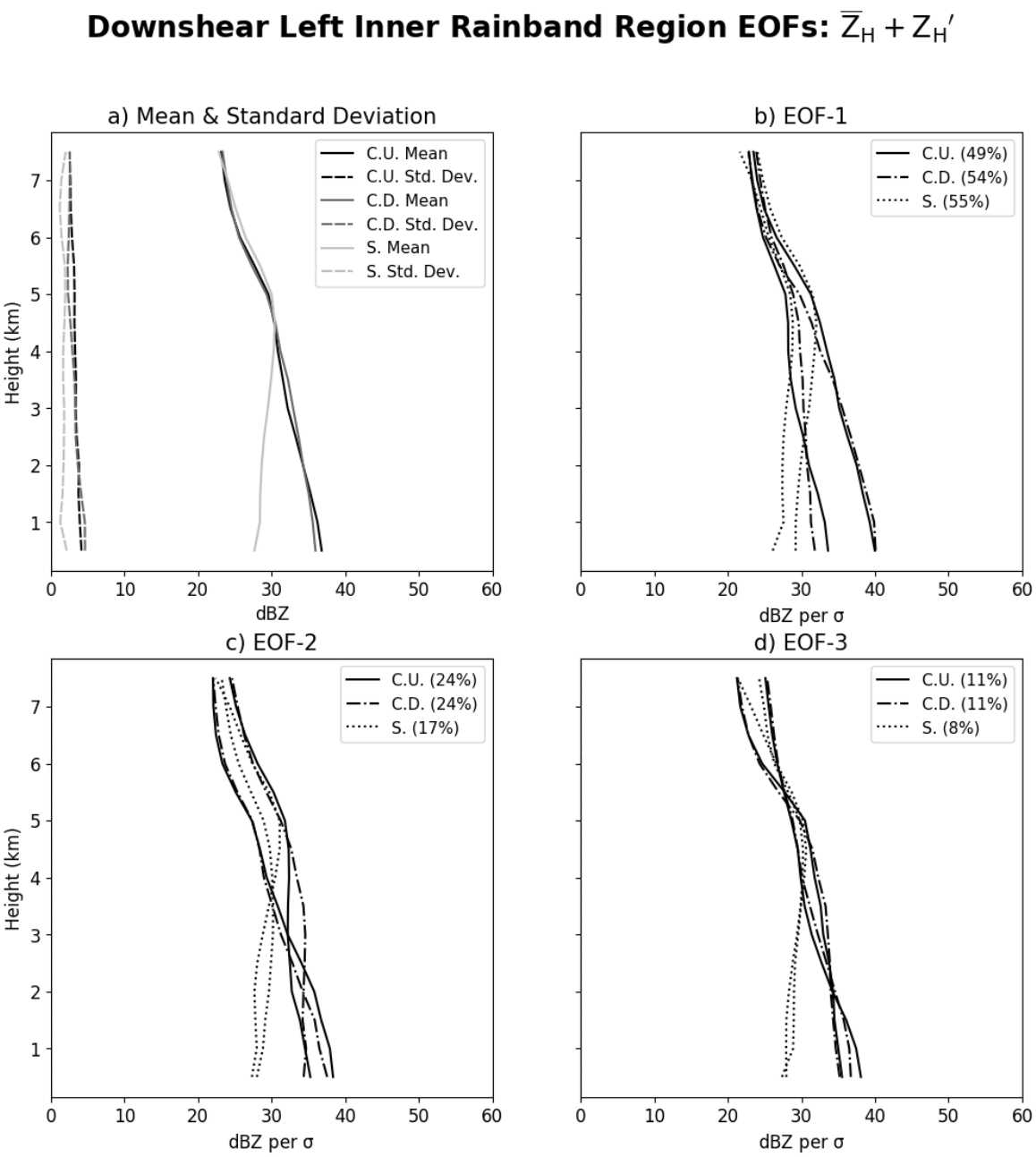

Figure 39: a) The mean (solid) and standard deviation (dashed) profiles for downshear left inner rainband radar reflectivity (Z_H) in the convective updraft (black; n=92), convective downdraft (gray; n=74), and stratiform (light gray; n=355) regions. **b)** EOF-1 profiles for downshear left inner rainband radar reflectivity in the convective updraft (solid), convective downdraft (dashed-dotted), and stratiform (dotted) regions. Corresponding variance explained percentages included in plot legend. **c)** As in b), except for EOF-2. **d)** As in b), except for EOF-3.

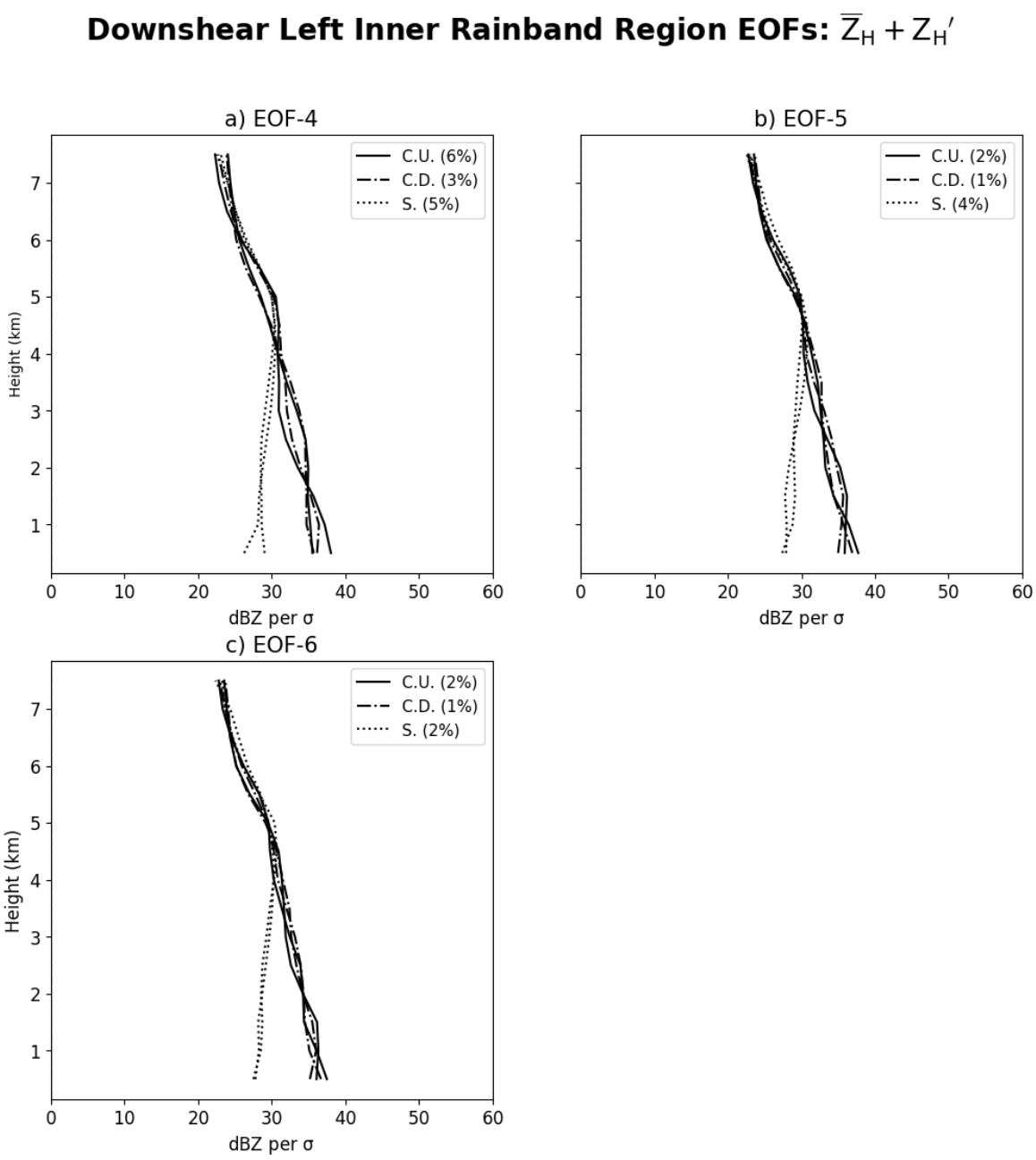

Figure 40: A continutation of the EOFs from Figure 39, where **a)** is EOF-4, **b)** is EOF-5, and **c)** is EOF-6.

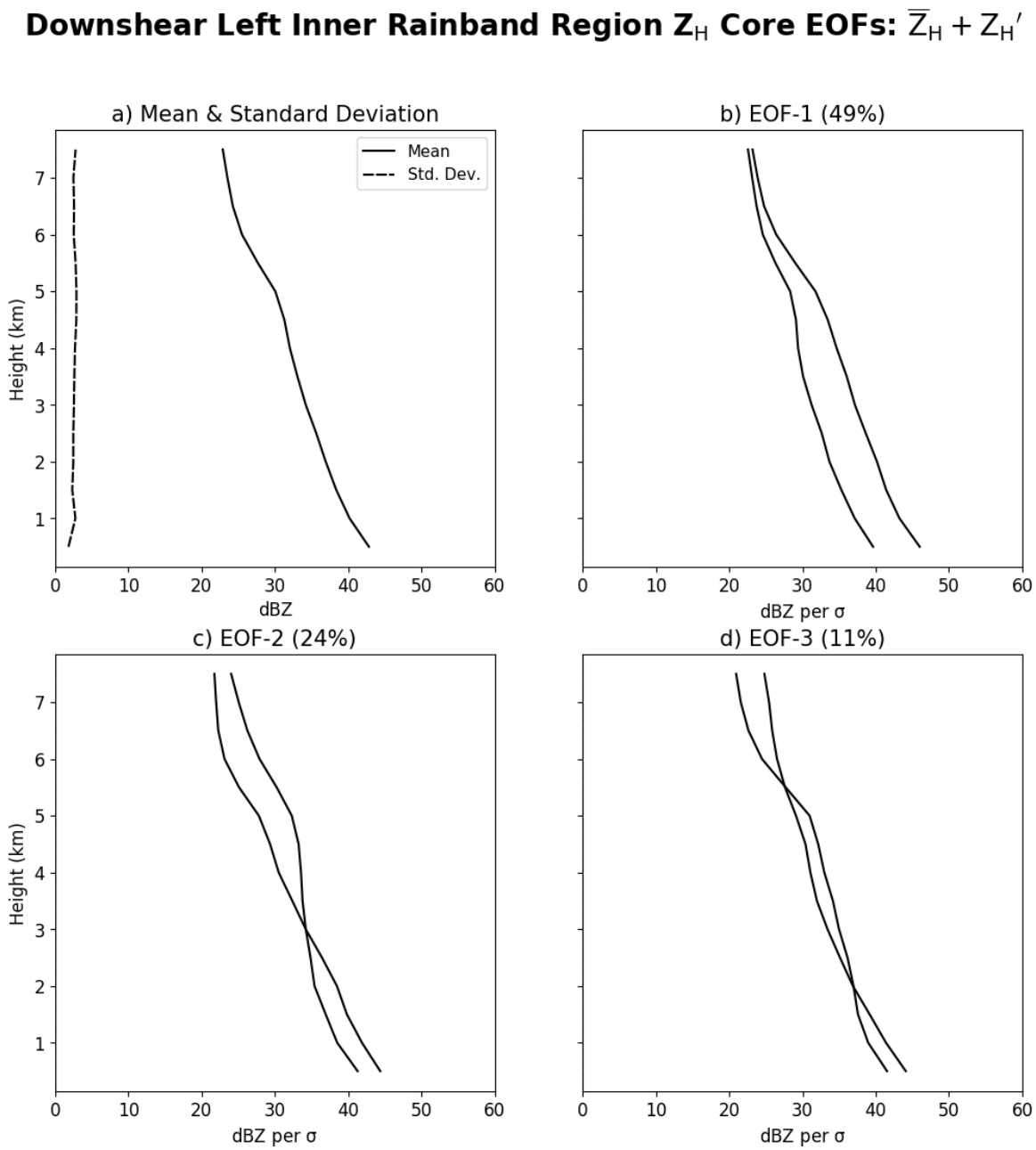

Figure 41: a) The mean (solid) and standard deviation (dashed) profiles for downshear left inner rainband radar reflectivity (Z_H) in the reflectivity cores (n=92). **b)** EOF-1 profiles for downshear left inner rainband radar reflectivity in the reflectivity cores. Corresponding variance explained percentages included in plot title. **c)** As in b), except for EOF-2. **d)** As in b), except for EOF-3.

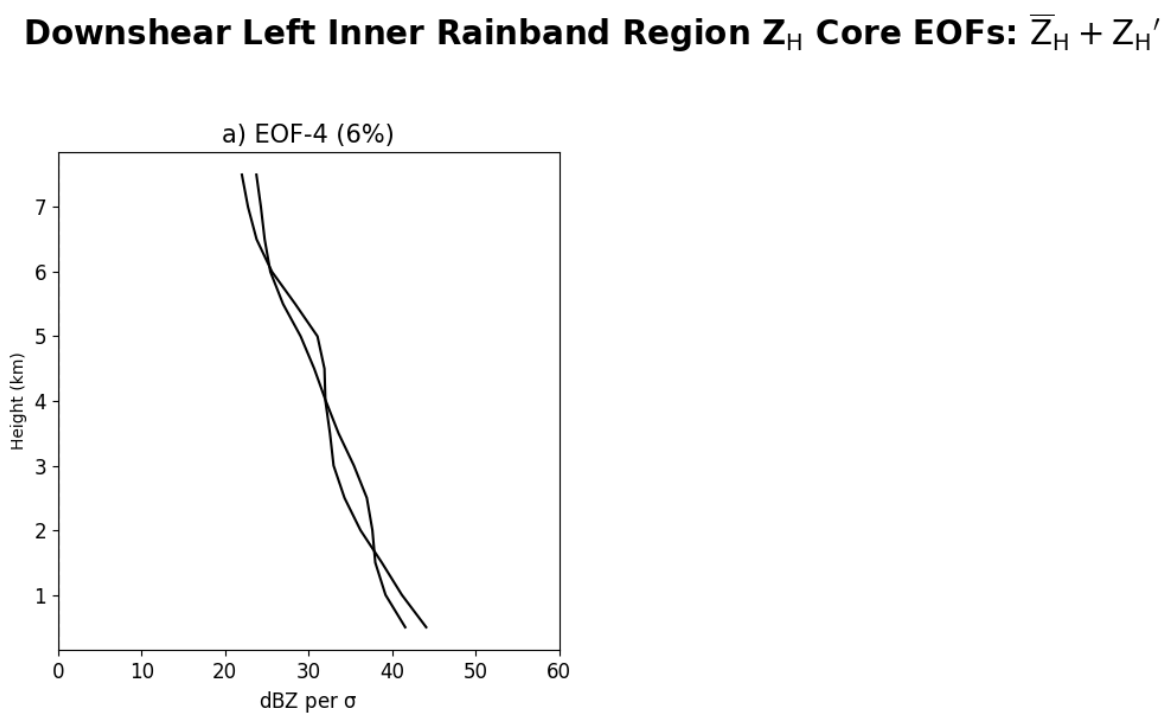

Figure 42: A continutation of the EOFs from Figure 41, where **a)** is EOF-4.

precipitation. Shown in Figures 39b–d and Figures 40a–c, the profiles for all six EOFs resemble the mean, pointing to a consistent increase in reflectivity with height in the stratiform inner rainbands and a reflectivity peak (i.e., bright band) in the mid-levels.

From Figure 41a, the relatively laminar mean reflectivity structure is also evident in the inner rainband reflectivity cores. Likewise, this structure is present in EOF-1 of Figure 41b, which explains 49% of the variance. Similarly, from Figures 41c–d, EOFs 2 and 3 show this laminar structure, although they also reveal more of an upright reflectivity structure. Because this upright structure is not present in the mean or EOF-1 profiles, inner rainband low-level >40 dBZ reflectivity maxima cannot be assumed to correspond to reflectivity towers. Overall, these profiles show the reflectivity field of the inner rainband reflectivity cores is similar to that of the inner rainband convective draft regions.

5.2.2 Vertical Velocity

Similar to the convective regions of the eyewall, the convective regions of the inner rainbands, presented in Figure 43a, show the mean vertical velocity magnitude increases with height. Interestingly, the mean vertical velocity in Figure 21b is inconsistent with this structure. However, it is likely the strong updrafts and downdrafts neutralize each other when the azimuthal-mean vertical profile is calculated. For the first EOF, displayed in Figure 43b, the convective updraft and downdraft regions both show profiles that increase in magnitude with height and profiles that remain weak in the mid-levels before increasing in value in the upper levels. Therefore, 93% and 96% of the variance in the inner rainband convective up- and downdrafts can be explained by both strong and weak drafts. The strong drafts are puzzling, however, as they are strongest in the upper levels and Didlake and Houze (2013a) found inner rainbands to be more shallow. They are also stronger than those of the eyewall region. However, these findings could be due to the proximity of the inner rainband region to the eyewall. From Figures 43c–d, EOFs 2 and 3 for the convective updraft and downdraft regions represent a combined 5% and <3% of the variance in the vertical velocity. They offer more variations of the profiles shown in EOF-1.

Also in Figure 43a, the mean stratiform inner rainband vertical velocity profile shows weak to near-zero upward motion, which further disagrees with the stratiform structure outlined by Marks and Houze (1987). EOF-1 explains 76% of the variance and is displayed in Figure 43b, where one profile shows a columnar weak updraft and the other profile shows a shallow low-level updraft capped by a downdraft. From Figure 43c, EOF-2 shows both a deeper updraft topped by a downdraft and a mostly columnar updraft with a mid-level downdraft. These profiles explain 14% of the variance. Lastly, shown in Figure 43d, EOF-3 explains 7% of the variance and shows a columnar

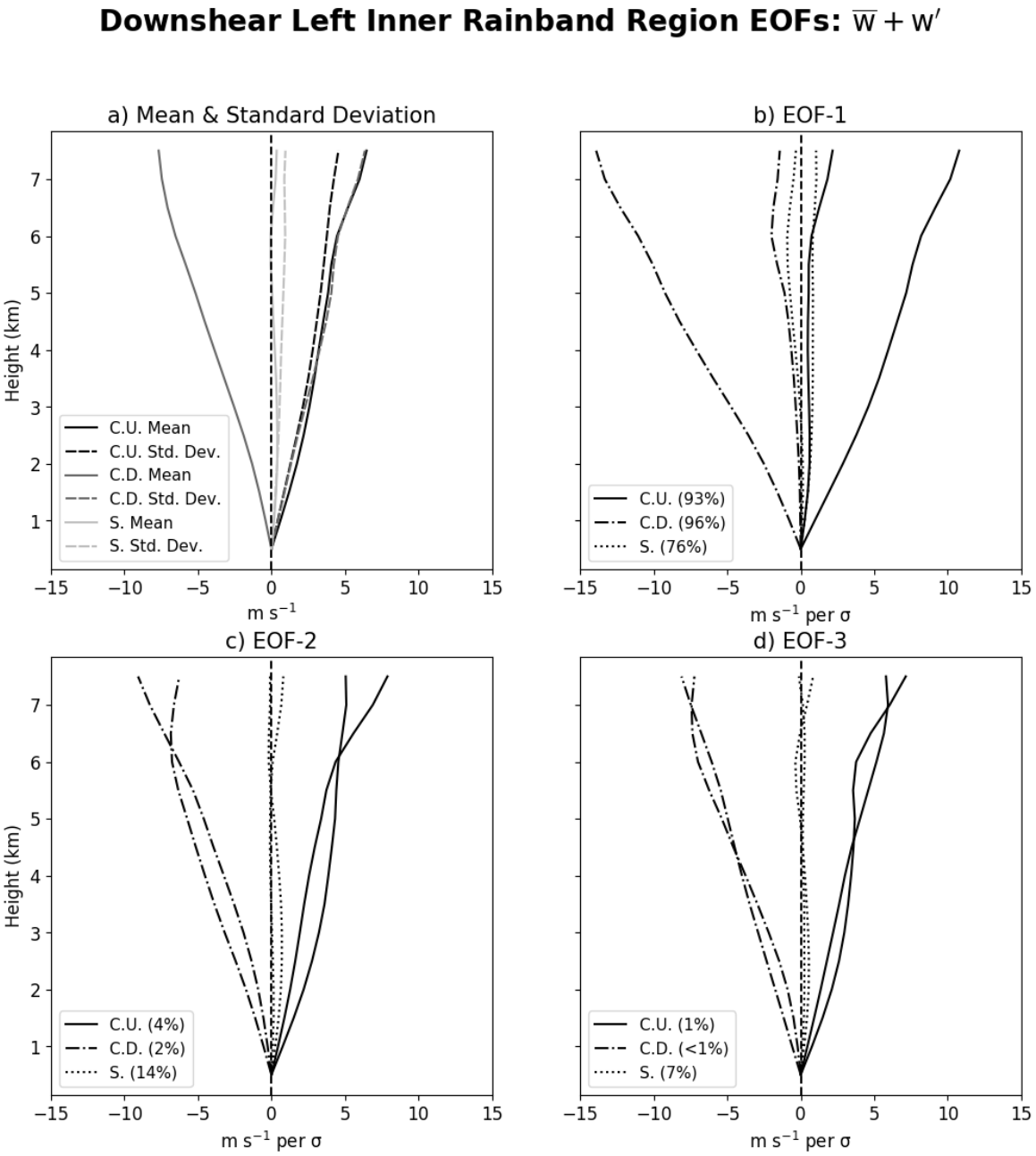

Figure 43: a) The mean (solid) and standard deviation (dashed) profiles for downshear left inner rainband vertical velocity (w) in the convective updraft (black; n=74), convective downdraft (gray; n=54), and stratiform (light gray; n=134) regions. **b)** EOF-1 profiles for downshear left inner rainband vertical velocity in the convective updraft (solid), convective downdraft (dashed-dotted), and stratiform (dotted) regions. Corresponding variance explained percentages included in plot legend. **c)** As in b), except for EOF-2. **d)** As in b), except for EOF-3.

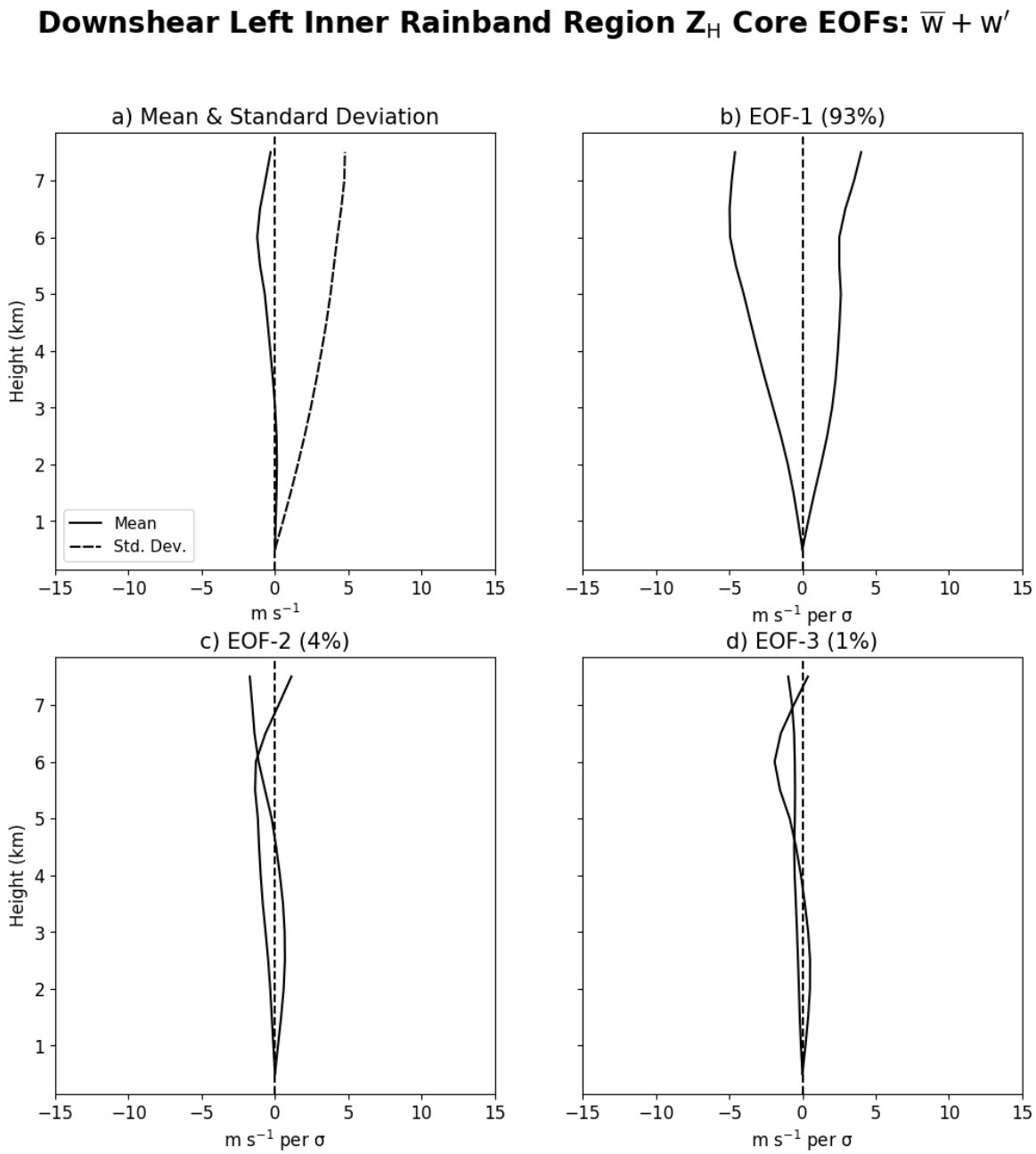

Figure 44: a) The mean (solid) and standard deviation (dashed) profiles for downshear left inner rainband vertical velocity (w) in the reflectivity cores (n=74). **b)** EOF-1 profiles for downshear left inner rainband vertical velocity in the reflectivity cores. Corresponding variance explained percentages included in plot title. **c)** As in b), except for EOF-2. **d)** As in b), except for EOF-3.

updraft as well as a mostly columnar updraft with a mid- to upper-level downdraft. In general, updrafts topped with downdrafts are more prevalent in the stratiform inner rainbands than the structure described by Marks and Houze (1987). Their proposed structure does occur in one EOF-2 and one EOF-3 profile, though it is more elevated and accompanied by an updraft in the low levels. Also, since it does not appear in EOF-1, the structure of Marks and Houze (1987) does not represent the majority of the variance in stratiform inner rainband vertical velocity.

The mean vertical velocity of the inner rainband convective cores, displayed in Figure 44a, shows a weak low-level updraft with a stronger upper-level downdraft. Like the inner rainband convective draft regions and shown in Figure 44b, the first EOF shows both a columnar updraft and a columnar downdraft that increase in value with height. These profiles explain 93% of the variance. Shown in Figure 44c, the mean structure is evident in EOF-2 in addition to a low- to mid-level downdraft and upper-level updraft. This structure resembles that of Marks and Houze (1987), although the downdraft-updraft transition is misplaced. Further, this profile only represents 4% of the variance, indicating this structure is not common in the inner rainband reflectivity cores. Explaining 1% of the variance and displayed in Figure 44d, EOF-3 shows a columnar weak downdraft and a profile that resembles the mean.

5.2.3 Radial Velocity

The mean radial velocity for the convective regions, displayed in Figure 45a, shows low-level radial inflow and upper-level radial outflow, where the inflow is largely stronger than the outflow. From Figure 45b, EOF-1 explains 68% of the variance in the convective updraft region and 69% of the variance in the convective downdraft region. The EOF-1 profiles for both convective regions illustrate both shallow (i.e., $\sim$2.5 km) and deep (i.e., $\sim$6 km) radial inflow beneath radial outflow. The shallow inflow is supported

by several conceptual models (e.g., Didlake and Houze 2013a; Barron et al. 2022), while the deep inflow is not. Explaining 20% and 17% of the variance in convective up- and downdraft radial velocity, respectively, and shown in Figure 45c, the EOF-2 profiles reveal low-level radial inflow that transitions to outflow in the mid-levels. Unlike EOF-1, the depth of the inflow in the EOF-2 profiles varies less. Even less variant, from Figure 45d, the inflow to outflow transition in the convective EOF-3 regions occurs at roughly the same height for all profiles. The convective up- and downdraft EOF-3 profiles represent 7% and 9% of the variance in radial velocity, respectively. Across all EOFs, the "in-up-out" secondary circulation structure described by Barron et al. (2022) is abundant. However, the "out-up-out" structure is not observed.

The mean stratiform inner rainband radial velocity, depicted in Figure 45a, shows weak, deep inflow up to a height of 5 km and radial outflow above 5 km. From Figure 45b, EOF-1 depicts low-level radial inflow and upper-level radial outflow, where the transition height ranges from 4-6 km. These profiles explain 67% of the variance in stratiform inner rainband radial velocity. Similarly, shown in Figure 45c, EOF-2 exhibits low-level inflow that transitions to outflow between 4.5-5.5 km. These profiles represent 20% of the variance. Lastly, explaining 8% of the variance and displayed in Figure 45d, EOF-3 shows two nearly identical profiles of low-level inflow that transition to outflow at a height of 5 km. These EOFs all show that the inflow in the stratiform inner rainbands is relatively weak and deep. They also show that the "in-up-out" secondary circulation from the conceptual models persists through the stratiform inner rainband region and the "out-up-out" circulation from Barron et al. (2022) is still absent.

Figure 46a reveals mean radial inflow below a height of 3 km and mean radial outflow above that height in the inner rainband reflectivity cores. Like the inner

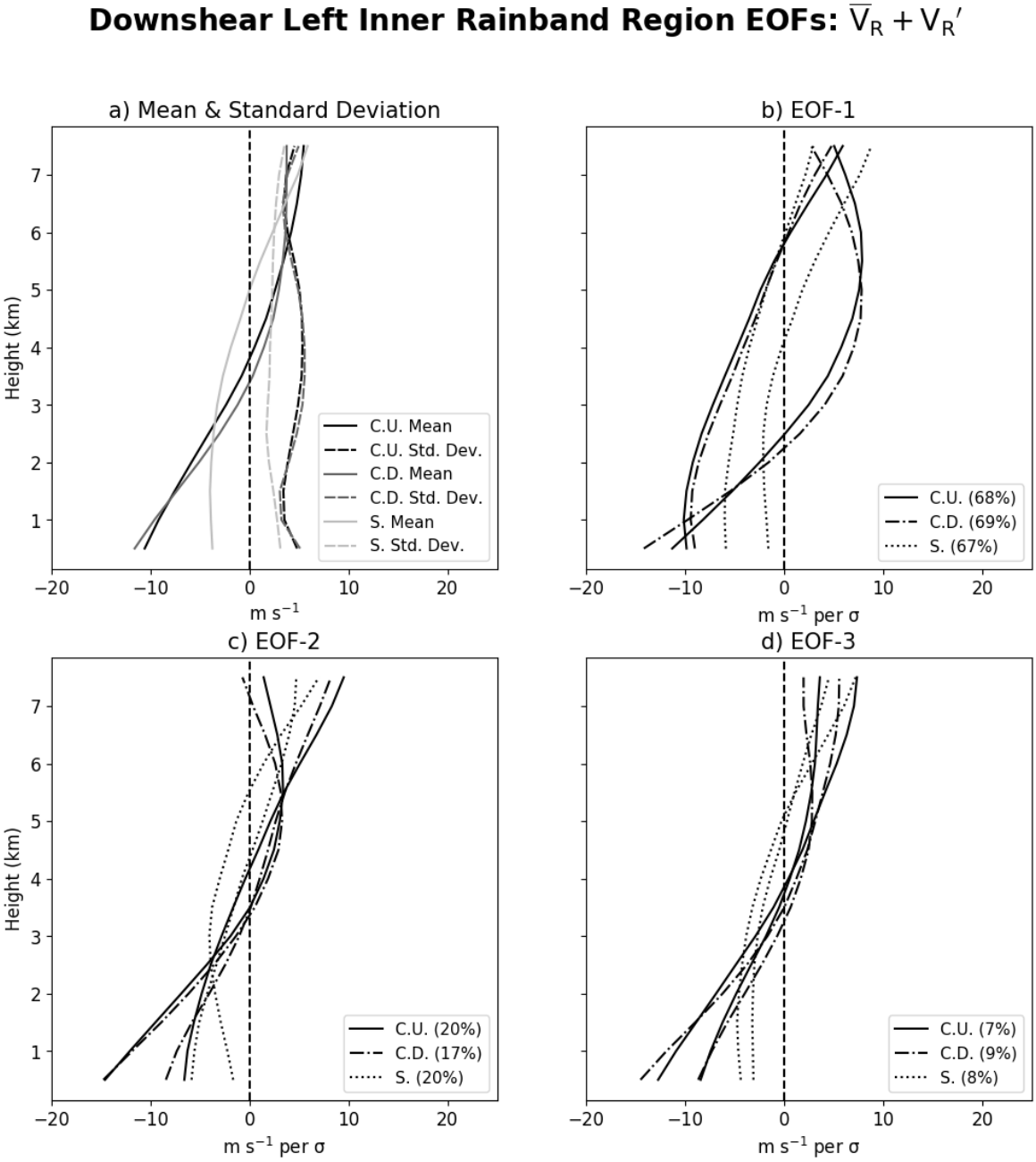

Figure 45: As in Figure 43, except for the radial velocity.

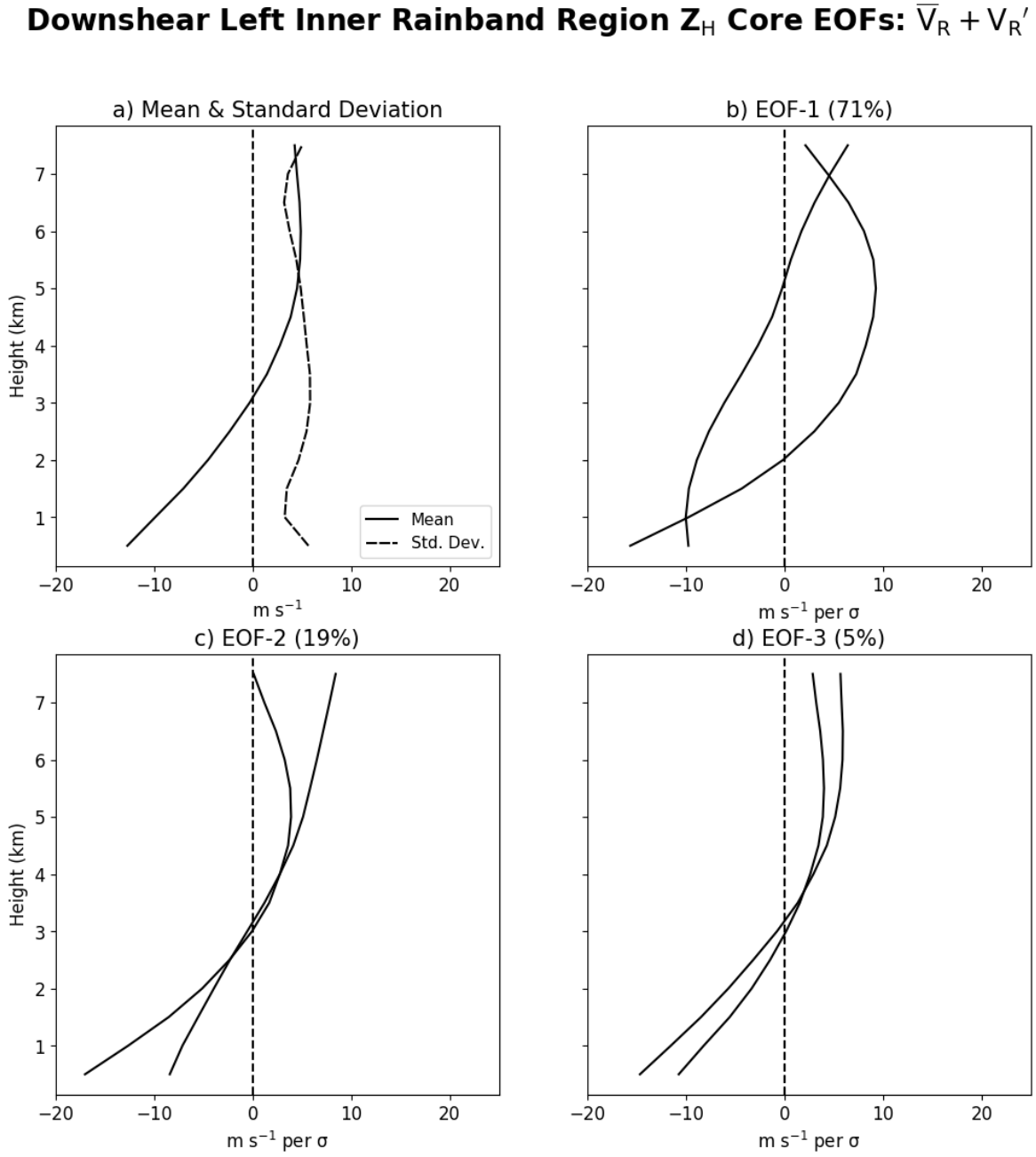

Figure 46: a) The mean (solid) and standard deviation (dashed) profiles for downshear left inner rainband radial velocity (w) in the reflectivity cores (n=75). **b)** EOF-1 profiles for downshear left inner rainband radial velocity in the reflectivity cores. Corresponding variance explained percentages included in plot title. **c)** As in b), except for EOF-2. **d)** As in b), except for EOF-3.

rainband convective draft regions, the reflectivity cores exhibit both shallow and deep inflow in EOF-1, presented in Figure 46b. These profiles represent 71% of the variance. However, like the mean structure, EOFs 2 and 3 do exhibit an inflow-outflow transition height of 3 km, shown in Figures 46c–d. These EOFs, explaining a combined 24% of the variance, therefore emphasize variations in the radial velocity magnitude.

5.2.4 Azimuthal Velocity

From Figure 47a, the mean azimuthal velocity profiles for both convective regions of the inner rainband show azimuthal velocity that maximizes between 2-4-km, which could be from a tangential jet. Compared to the eyewall, the mean inner rainband convective azimuthal velocity is lower in magnitude. This observation is consistent with angular momentum conservation requirements, where an increase in radius translates to a decrease in azimuthal velocity. From Figure 47b, the EOF-1 profiles are nearly identical between the convective updraft and downdraft regions and show two azimuthal velocity profiles of varying magnitude. Similar to the mean profile, these profiles maximize between heights of 2-4 km. The convective updraft and downdraft EOF-1 profiles explain 71% and 66% of the variance in azimuthal velocity, respectively. From Figure 47c, one EOF-2 profile resembles the mean, while the other appears to be relatively steady with height. Like in the eyewall region, the profile with steady azimuthal velocity with height points to the existence of a weaker vertical azimuthal velocity gradient in some places. These profiles represent 16% (22%) of the variance in convective updraft (downdraft) azimuthal velocity. Displayed in Figure 47d, aside from low-level and upper-level differences in magnitude, the EOF-3 convective profiles are identical and are similar to the mean structure. For EOF-3, the convective up-

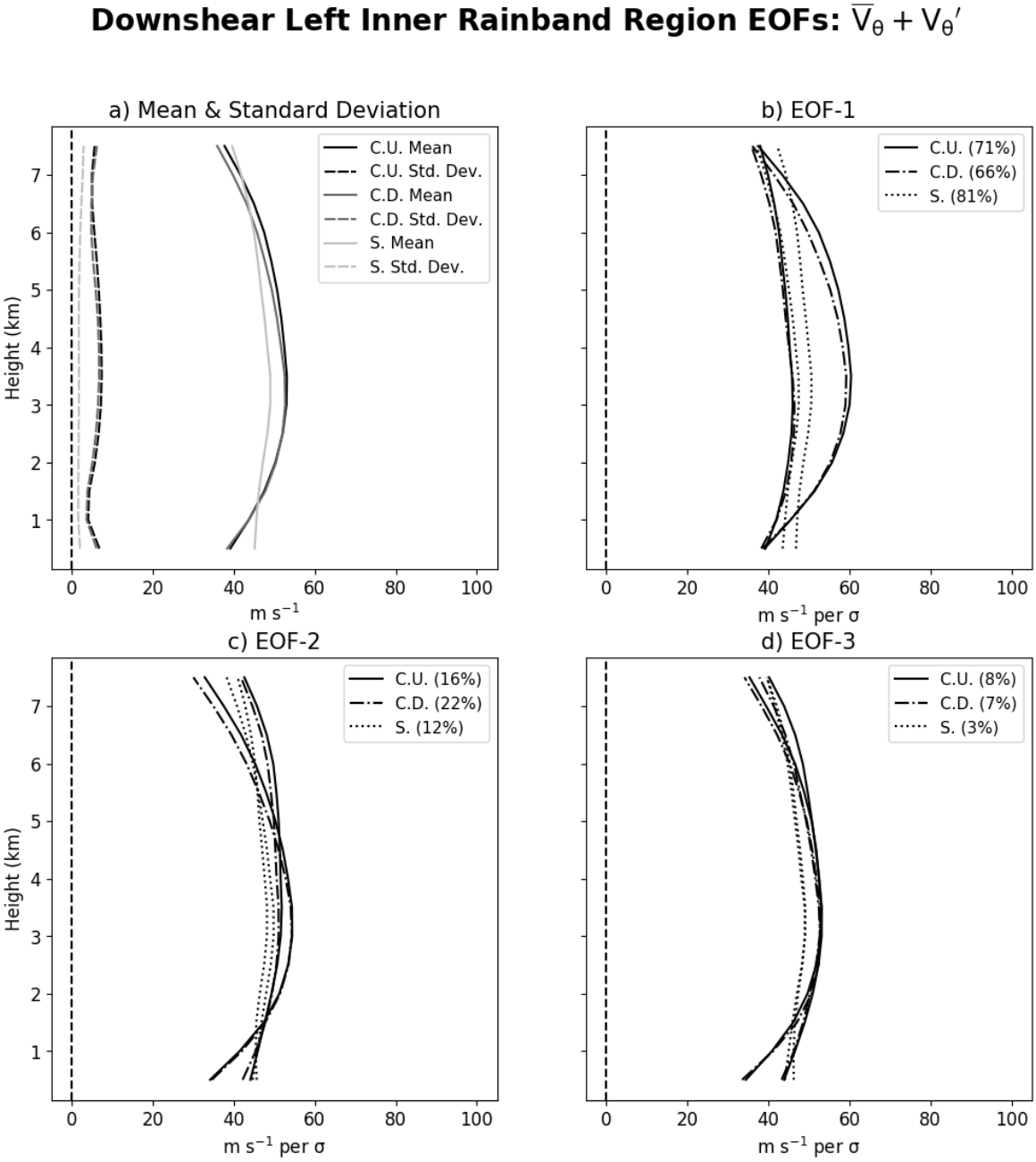

Figure 47: As in Figure 43, except for the azimuthal velocity.

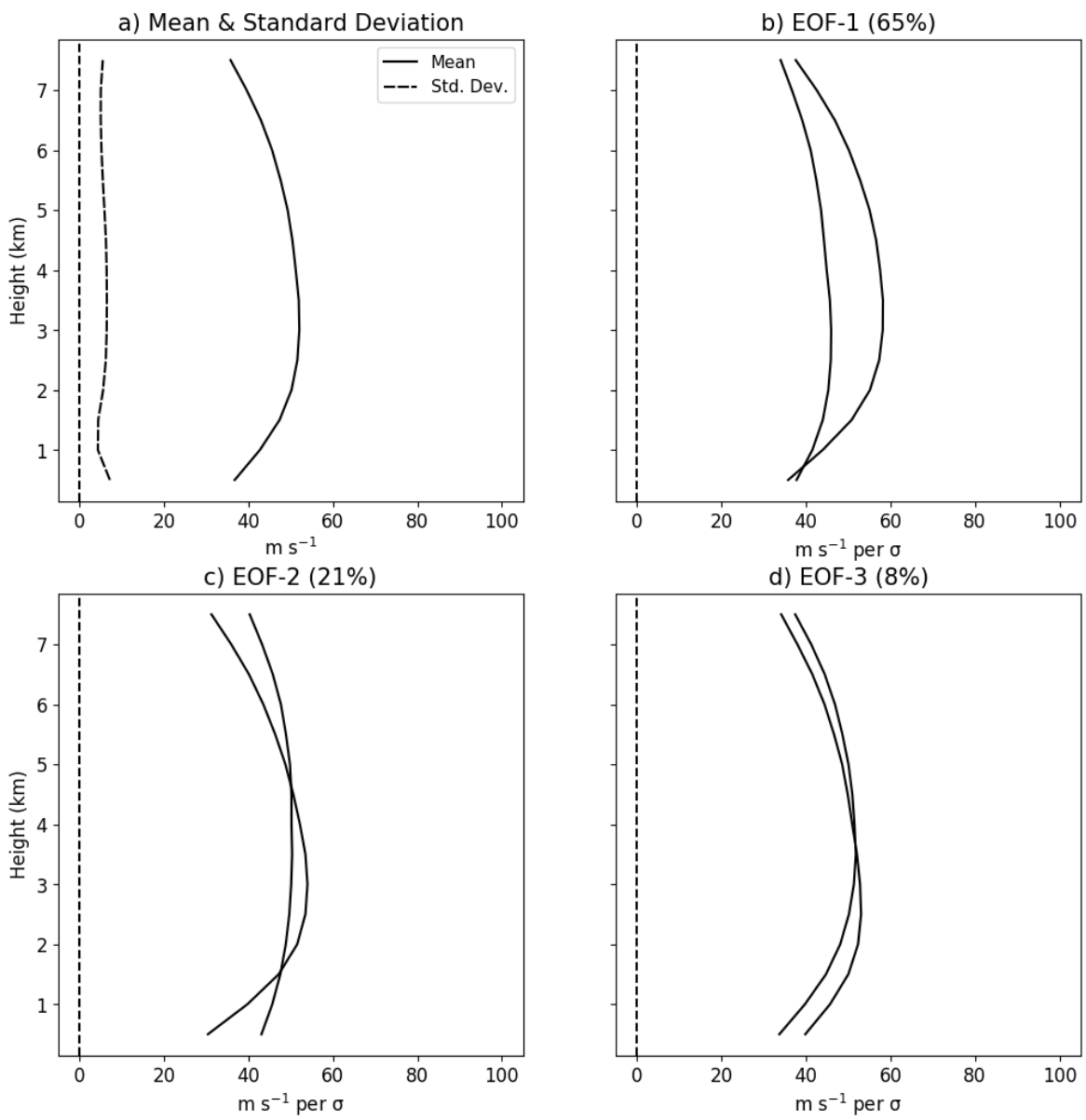

Figure 48: As in Figure 46, except for the azimuthal velocity.

and downdraft profiles explain 8% and 7% of the variance in inner rainband azimuthal velocity, respectively.

From Figure 47a, the stratiform inner rainband mean azimuthal velocity profile shares a similar magnitude with the convective regions, except the 2-4-km height maximum is more muted. In general, this profile likely represents the background azimuthal velocity, as the tangential jets observed in the convective regions are either reduced or absent in the conceptual model stratiform regions. Since an azimuthal velocity maximum is vaguely present, this points to the possible presence of a weakening tangential jet from eroding convection (Didlake and Houze 2013b). Shown in Figures 47b–d, EOFs 1-3 show profiles that resemble the mean profile, where a faint azimuthal velocity maximum is evident between 2-4 km in all profiles.

The mean, standard deviation, and EOF profiles for the azimuthal velocity of the inner rainband reflectivity cores are displayed in Figures 48a–d. These profiles all resemble those of the inner rainband convective draft regions, where the azimuthal velocity maxima are commonly observed between heights of 2-4 km. The profile with the weaker azimuthal velocity vertical gradient persists in EOF-2 and explains 21% of the variance.

5.2.5 Relative Vorticity

In Figure 49a, the mean vertical vorticity for the convective updraft region shows cyclonic vorticity that decreases in the mid-levels and increases again in the upper levels. Displayed in Figure 49b, EOF-1 shows one profile where low-level cyclonic vorticity transitions to anticyclonic vorticity in the upper levels. The other profile displays weak low- to mid-level anticyclonic vertical vorticity in an otherwise cyclonic profile. These profiles represent 38% of the variance in inner rainband convective updraft relative vorticity. From Figure 49c, EOF-2 shows a profile that resembles

the mean. That is, a profile of columnar cyclonic vorticity that minimizes in the mid-levels. The other profile exhibits low-level anticyclonic vorticity and upper-level cyclonic vorticity. These profiles represent 27% of the variance. The EOF-3 profiles, displayed in Figure 49d, show deep mid-level anticyclonic vorticity in an otherwise cyclonic profile as well as an exclusively cyclonic profile. The EOF-3 profiles represent 20% of the variance. Explaining 6% of the variance and shown in Figure 50a, the EOF-4 profiles both show brief anticyclonic vorticity in otherwise cyclonic vorticity profiles. Lastly, similar to many of the other EOFs and displayed in Figure 50b, EOF-5 shows a columnar cyclonic vorticity profile as well as a cyclonic vorticity profile with weak mid-level anticyclonic vorticity. These profiles represent 3% of the variance in inner rainband convective updraft relative vorticity. Like relative vorticity in the eyewall convective updraft region, the inner rainband convective updraft relative vorticity is largely cyclonic, albeit more anticyclonic, and possesses a wide variety of magnitudes and structures.

For the convective downdraft region, in Figure 49a, the mean relative vorticity profile is mostly cyclonic, aside from some brief anticyclonic vorticity at a 2.5-km height. From Figure 49b, one of the EOF-1 profiles shows a mostly cyclonic vorticity profile with minimal (and briefly anticyclonic) vorticity in the mid-levels. The other profile shows low-level anticyclonic vorticity that transitions to weakly positive vorticity in the mid-levels and transitions back to negative vorticity in the upper levels. These EOF profiles explain 41% of the variance in the inner rainband convective downdraft relative vorticity. Similarly, representing 26% of the variance and displayed in Figure 49c, the EOF-2 profiles show either columnar negative vorticity or columnar positive

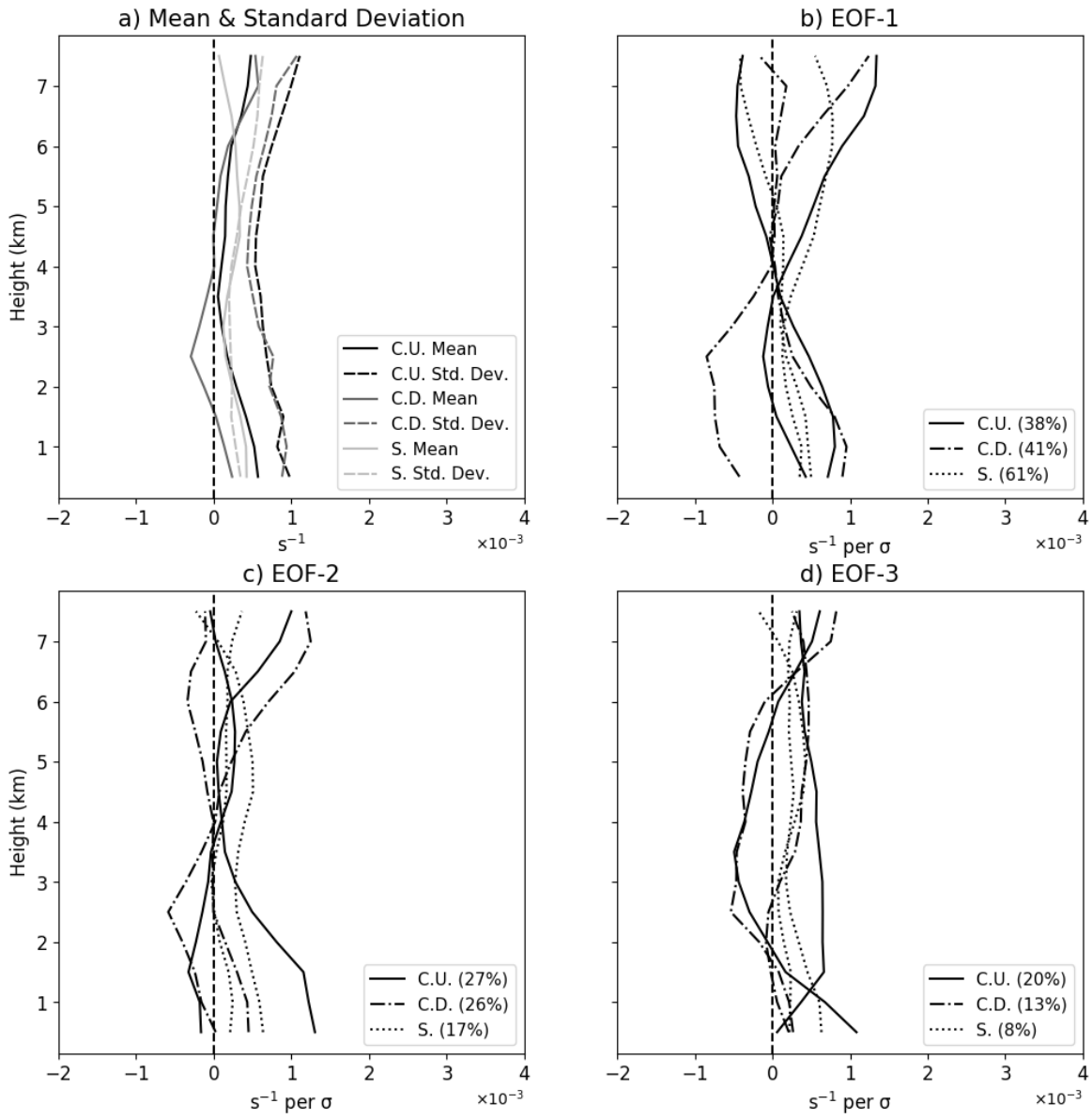

Figure 49: a) The mean (solid) and standard deviation (dashed) profiles for downshear left inner rainband relative vorticity (ζ) in the convective updraft (black; n=63), convective downdraft (gray; n=47), and stratiform (light gray; n=104) regions. **b)** EOF-1 profiles for downshear left inner rainband relative vorticity in the convective updraft (solid), convective downdraft (dashed-dotted), and stratiform (dotted) regions. Corresponding variance explained percentages included in plot legend. **c)** As in b), except for EOF-2. **d)** As in b), except for EOF-3.

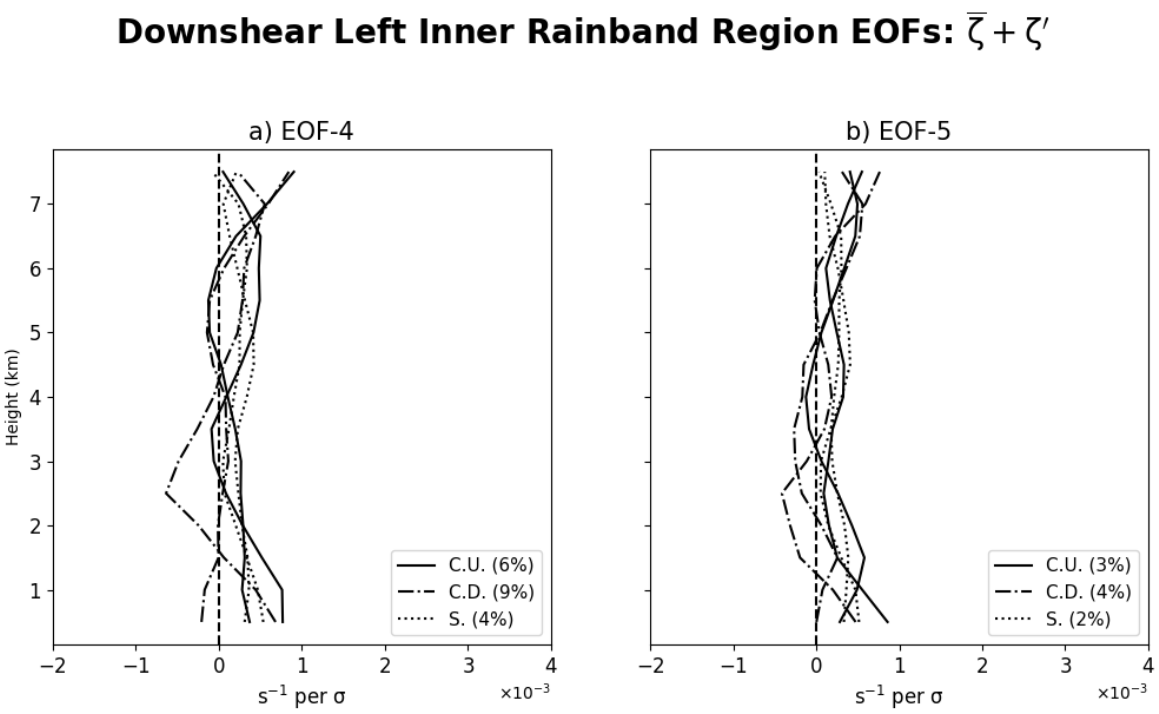

Figure 50: A continutation of the EOFs from Figure 49, where **a)** is EOF-4, and **b)** is EOF-5.

vorticity that minimizes in the mid-levels. From Figure 49d, both EOF-3 profiles display low-level cyclonic vorticity before transitioning to anticyclonic vorticity. Above this transition, one vorticity profile remains negative, while the other transitions back to positive vorticity. In the upper levels, both profiles have positive vorticity. These profiles represent 13% of the variance. Representing 9% of the variance and presented in Figure 50a, one EOF-4 profile shows a mostly cyclonic vorticity profile that has anticyclonic vorticity in the low- to mid-levels. The other profile shows low-level negative vorticity that transitions to positive vorticity and back to negative vorticity in the mid-levels, ultimately becoming positive in the upper levels. From Figure 50b, both EOF-5 profiles show variations of low-level cyclonic vorticity, mid-level anticyclonic vorticity, and upper-level cyclonic vorticity. These profiles explain 4% of the variance

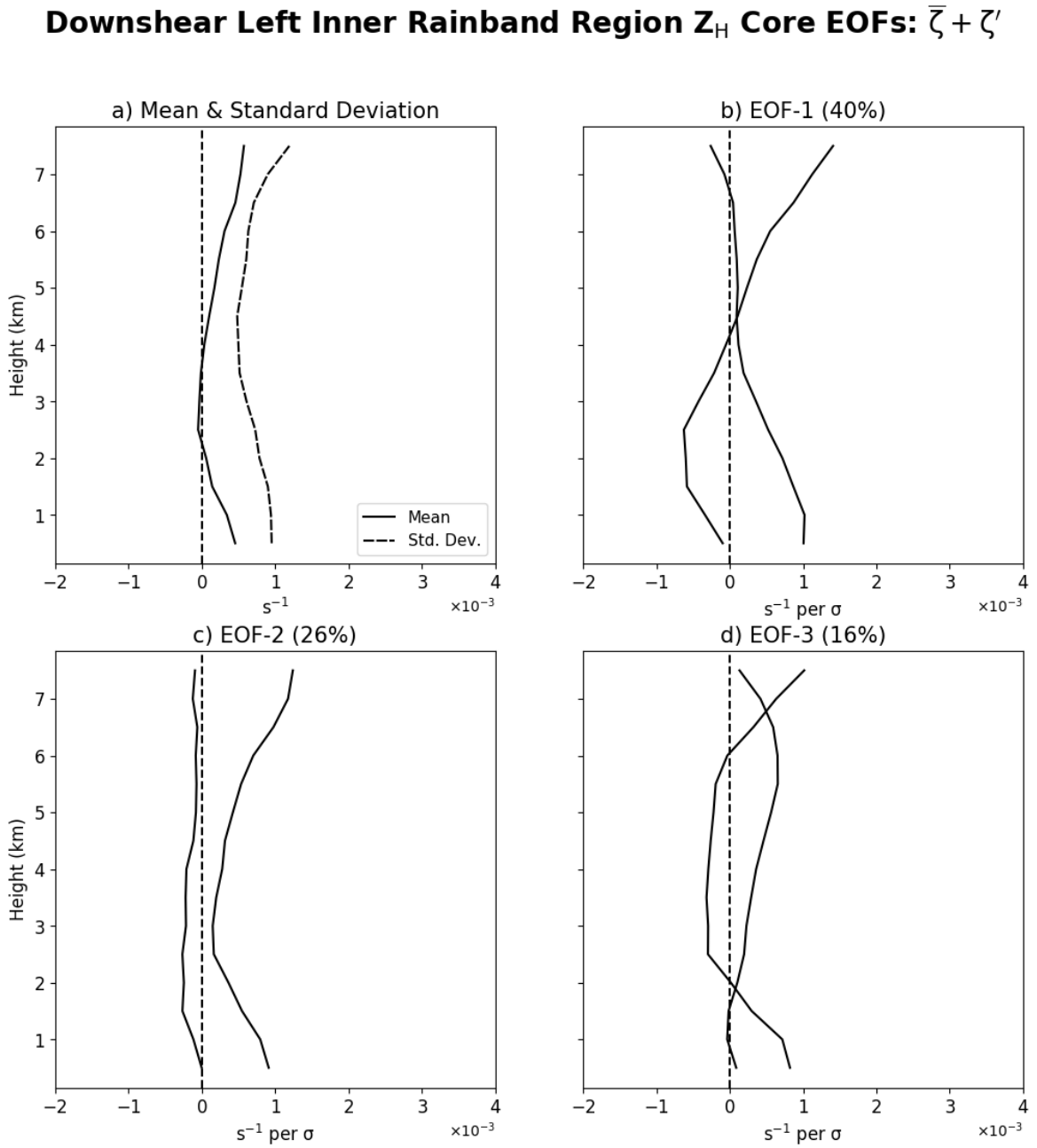

Figure 51: a) The mean (solid) and standard deviation (dashed) profiles for downshear left inner rainband relative vorticity (ζ) in the reflectivity cores (n=58). **b)** EOF-1 profiles for downshear left inner rainband relative vorticity in the reflectivity cores. Corresponding variance explained percentages included in plot title. **c)** As in b), except for EOF-2. **d)** As in b), except for EOF-3.

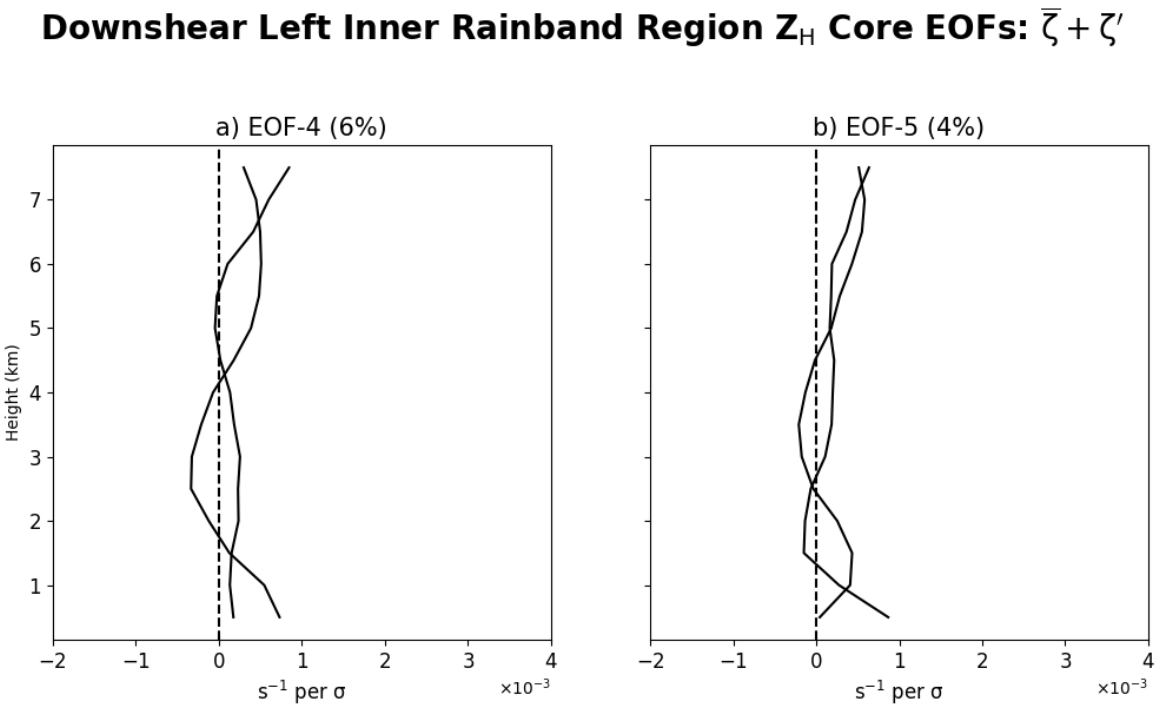

Figure 52: A continutation of the EOFs from Figure 51, where **a)** is EOF-4, and **b)** is EOF-5.

in the inner rainband convective downdraft relative vorticity. The inner rainband convective downdraft relative vorticity, like the inner rainband convective updraft relative vorticity, exhibits both anticyclonic and cyclonic vorticity transport and shows profiles of vastly different shapes and magnitude.

The mean stratiform inner rainband vertical vorticity is exclusively cyclonic and is displayed in Figure 49a. Explaining 61% of the variance and shown in Figure 49b, EOF-1 shows one profile of columnar cyclonic vorticity and another profile of low- to mid-level cyclonic vorticity and upper-level anticyclonic vorticity. EOF-2, representing 17% of the variance and displayed in Figure 49c, shows mostly columnar positive vorticity for both profiles, where one transitions to negative vorticity in the upper levels. EOFs 3-5, shown in Figure 49d and Figures 50a–b, exhibit profiles that are similar in structure to EOF-2, with slightly different magnitudes. These EOFs explain 8%, 4%, and 2% of the

variance in stratiform inner rainband relative vorticity, respectively. Unlike the inner rainband convective regions, the stratiform inner rainband relative vorticity profiles are mostly cyclonic, except for upper-level anticyclonic vorticity in some cases. The general shape and magnitude of these profiles are also relatively consistent across the EOFs, suggesting there is less variation in the stratiform inner rainband relative vorticity than in the convective inner rainbands.

From Figure 51a, the mean vertical vorticity profile for the inner rainband reflectivity cores is mostly cyclonic, aside from brief mean anticyclonic vorticity in the mid-levels. EOF-1, explaining 40% of the variance and presented in Figure 51b, shows low-level anticyclonic (cyclonic) vorticity that transitions to cyclonic (anticyclonic) vorticity in the mid-levels (upper levels). On the other hand, shown in Figure 51c, the profiles for the second EOF are exclusively cyclonic or anticyclonic and represent 26% of the variance. Displayed in Figure 51d and explaining 16% of the variance, one EOF-3 profile shows columnar cyclonic vorticity, while the other shows deep mid-level anticyclonic vorticity in an otherwise cyclonic profile. Lastly, from Figures 52a–b, the EOF-4 and EOF-5 profiles oscillate between cyclonic and anticyclonic vorticity and explain a combined 10% of the variance. These profiles show both anticyclonic and cyclonic vorticity exist in the inner rainband reflectivity cores, where anticyclonic vorticity is more prevalent than in the eyewall reflectivity cores.

5.2.6 Divergence

From Figure 53a, the inner rainband convective updraft mean profile exclusively shows convergence, where the highest magnitude occurs near the surface and the lowest magnitude occurs in the mid-levels. This mean convergence is expected in the low levels, based on mass continuity, although the expected mid- to upper-level divergence is absent. However, weak mean convergence exists in the mid-levels. EOF-1, displayed in

Figure 53b, shows one profile of convergence that maximizes near the surface. The other profile is mostly convergent aside from some brief mid-level divergence, which is likely associated with the mid-level updraft weakening observed in Figure 43. These profiles represent 47% of the variance in inner rainband convective updraft divergence. Representing 22% of the variance and shown in Figure 53c, EOF-2 shows two profiles that are nearly identically convergent in the lower levels. One profile remains convergent throughout the column, while the other transitions to divergence in the mid-levels. Similar to EOF-1, these profiles suggest the presence of mid-level updraft weakening. For the third EOF, shown in Figure 53d, weaker mid-level vertical motion is also probable based on the location of divergence within the profile. The EOF-3 profiles represent 16% of the variance. From Figures 54a–c, EOFs 4-6 exhibit entirely convergent profiles, pointing to the absence of mid-level updraft weakening. These EOFs collectively explain 10% of the variance in inner rainband convective updraft divergence.

Aside from slight mean convergence at the lowest level, mean divergence exists in the inner rainband convective downdraft region, based on Figure 53a. The strongest divergence occurs in the lower levels, while the weakest divergence occurs in the upper levels. Expected based on mass continuity, mean convergence in the mid- to upper-levels is not evident, though the mean divergence does decrease with height in the upper levels. Therefore, mean convergence likely occurs above the vertical extent of this analysis. Shown in Figure 53b and explaining 60% of the variance in inner rainband convective downdraft divergence, EOF-1 shows two divergent profiles of varying magnitude, where one exhibits low-level and upper-level convergence. These profiles suggest downdraft weakening may be collocated with the upper-level convergence, which is

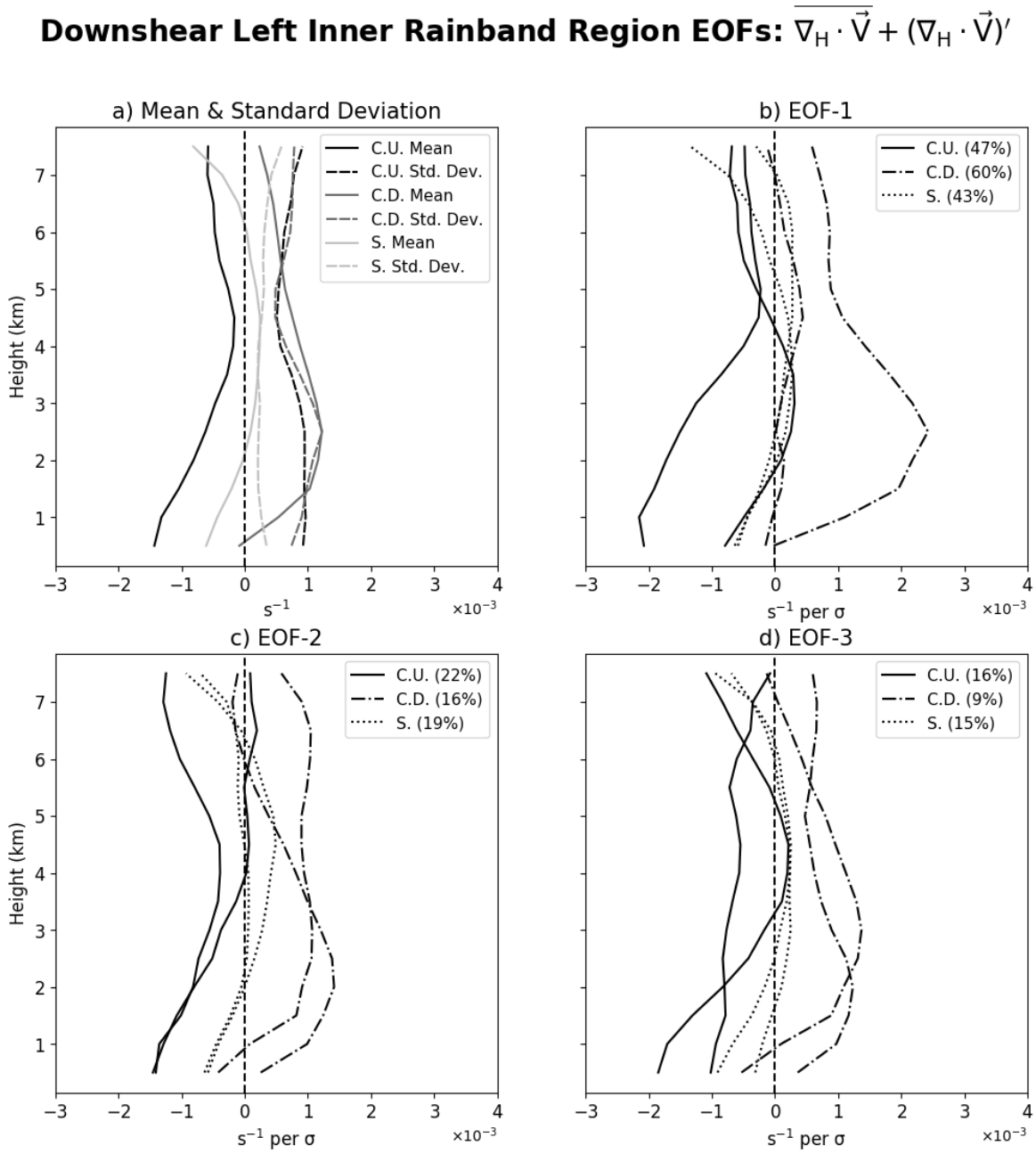

Figure 53: a) The mean (solid) and standard deviation (dashed) profiles for downshear left inner rainband divergence ($\nabla_H \cdot \vec{V}$) in the convective updraft (black; n=65), convective downdraft (gray; n=49), and stratiform (light gray; n=107) regions. **b)** EOF-1 profiles for downshear left inner rainband divergence in the convective updraft (solid), convective downdraft (dashed-dotted), and stratiform (dotted) regions. Corresponding variance explained percentages included in plot legend. **c)** As in b), except for EOF-2. **d)** As in b), except for EOF-3.

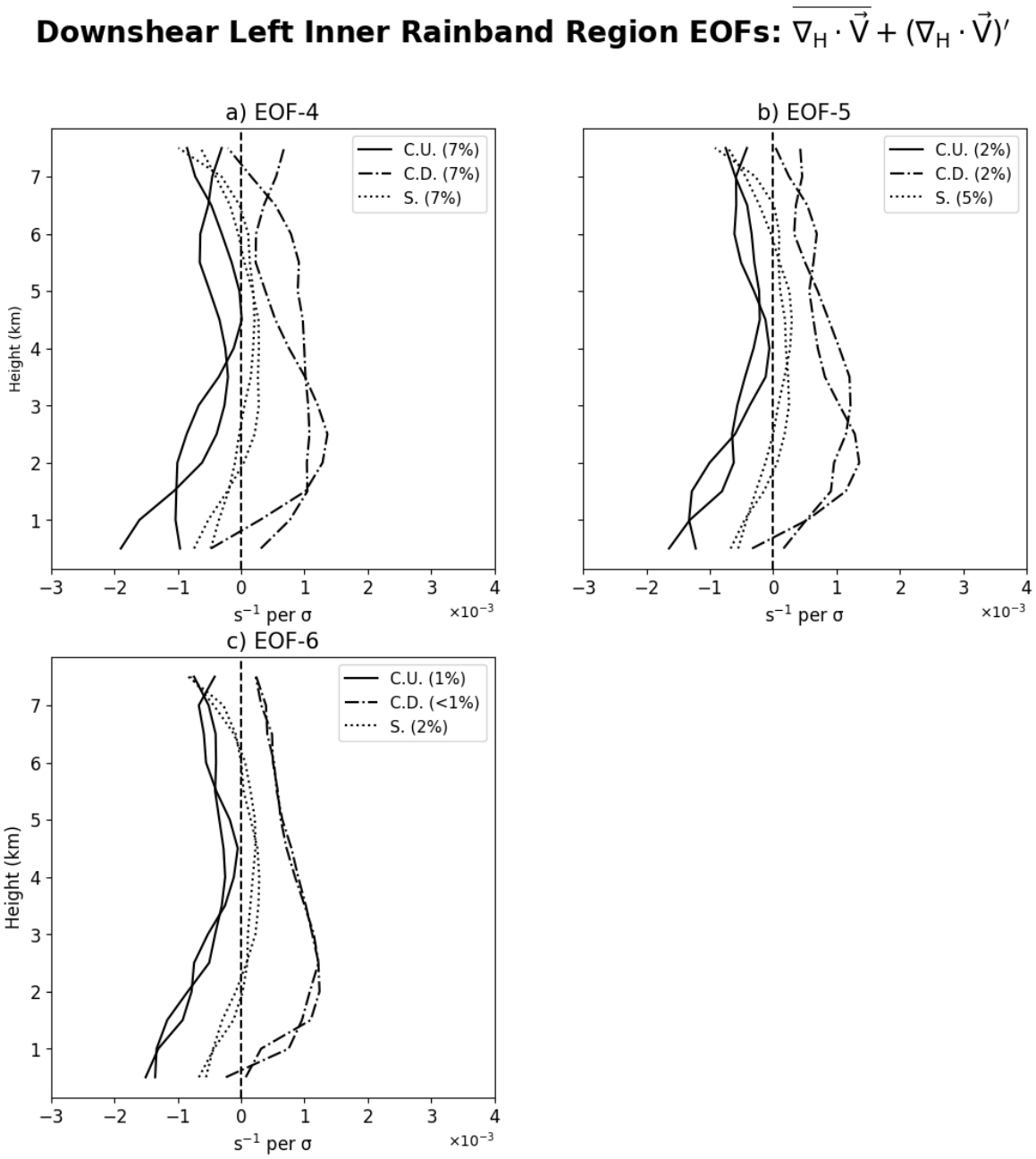

Figure 54: A continutation of the EOFs from Figure 53, where **a)** is EOF-4, **b)** is EOF-5, and **c)** is EOF-6.

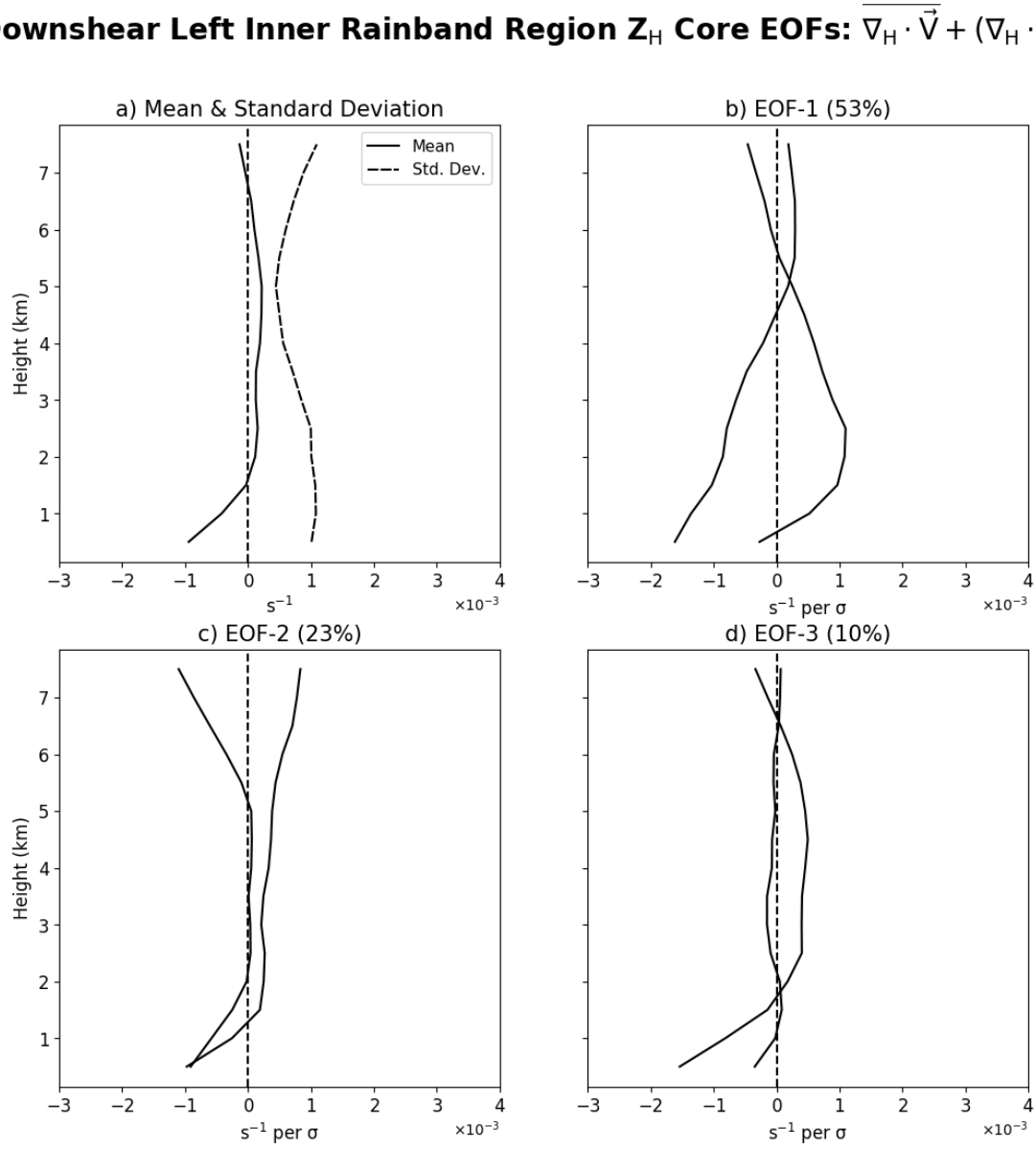

Figure 55: a) The mean (solid) and standard deviation (dashed) profiles for downshear left inner rainband divergence ($\nabla_H \cdot \vec{V}$) in the reflectivity cores (n=59). **b)** EOF-1 profiles for downshear left inner rainband divergence in the reflectivity cores. Corresponding variance explained percentages included in plot title. **c)** As in b), except for EOF-2. **d)** As in b), except for EOF-3.

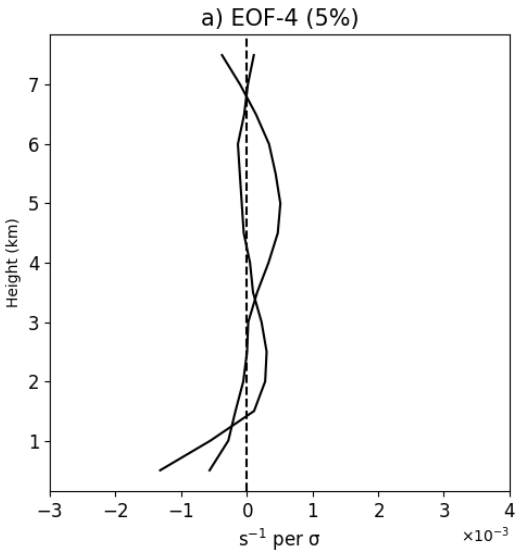

Figure 56: A continutation of the EOFs from Figure 55, where **a)** is EOF-4.

confirmed by Figure 43. The profiles offered by EOFs 2-6, displayed in Figures 49c–d and Figures 50a–c, are similar to those of EOF-1, as they are mostly divergent except for near-surface convergence and upper-level convergence in some.

From Figure 53a, the mean stratiform divergence profile shows low-level convergence, mid-level divergence, and upper-level convergence. Based on mass continuity, this profile points to either low- to mid-level mean upward motion and mid- to upper-level mean downward motion or mean updraft weakening in the mid-levels. From Figure 43, the latter case is consistent with the mean stratiform inner rainband vertical velocity structure. Shown in Figures 53b–d and Figures 54a–c, all EOF profiles show some form of low-level convergence, mid-level divergence, and upper-level convergence. Therefore, the stacked updraft-downdraft and mid-level updraft weakening structures prescribed by mass continuity are expected across all stratiform inner rainband EOFs. Sure enough, they are both evident in Figure 43.

For the inner rainband reflectivity cores, shown in Figure 55a, the mean profile depicts low- and upper-level convergence and mid-level divergence. This structure is indicative of either mid-level updraft weakening or a low- to mid-level updraft and mid- to upper-level downdraft. Indeed, the mean structure shown in Figure 44 is consistent with the latter option. From Figure 55b, EOF-1 explains 53% of the variance and shows a profile of low-level convergence (divergence) that transitions to divergence (convergence) in the mid- to upper levels. This likely corresponds to the weakening of drafts in the mid- to upper levels observed in Figure 44b. Both EOF-2 profiles, displayed in Figure 55c, are convergent in the low-levels before they transition to divergence. Above a height of 5 km, one profile reverts back to convergence while the other remains divergent. These profiles represent 23% of the variance. From Figure 55d, one of the EOF-3 profiles is weakly convergent and the other profile resembles the mean structure. Lastly, from Figure 56a, the EOF-4 profiles oscillate between convergence and divergence.

5.3 Outer Rainband Region

5.3.1 Radar Reflectivity

From Figure 57a, the mean reflectivity profiles for both convective regions are nearly identical, with slight differences in magnitude in the lower levels. In general, these profiles show relatively steady reflectivity up to a height of 5 km, where they begin to decrease with height more drastically. This drastic decrease marks the upper extent of convective cores. Shown in Figure 57b, EOF-1 explains 81% and 65% of the variance in outer rainband reflectivity for the convective updraft and downdraft regions, respectively. These profiles all resemble the shape of the mean, where one set of profiles has a

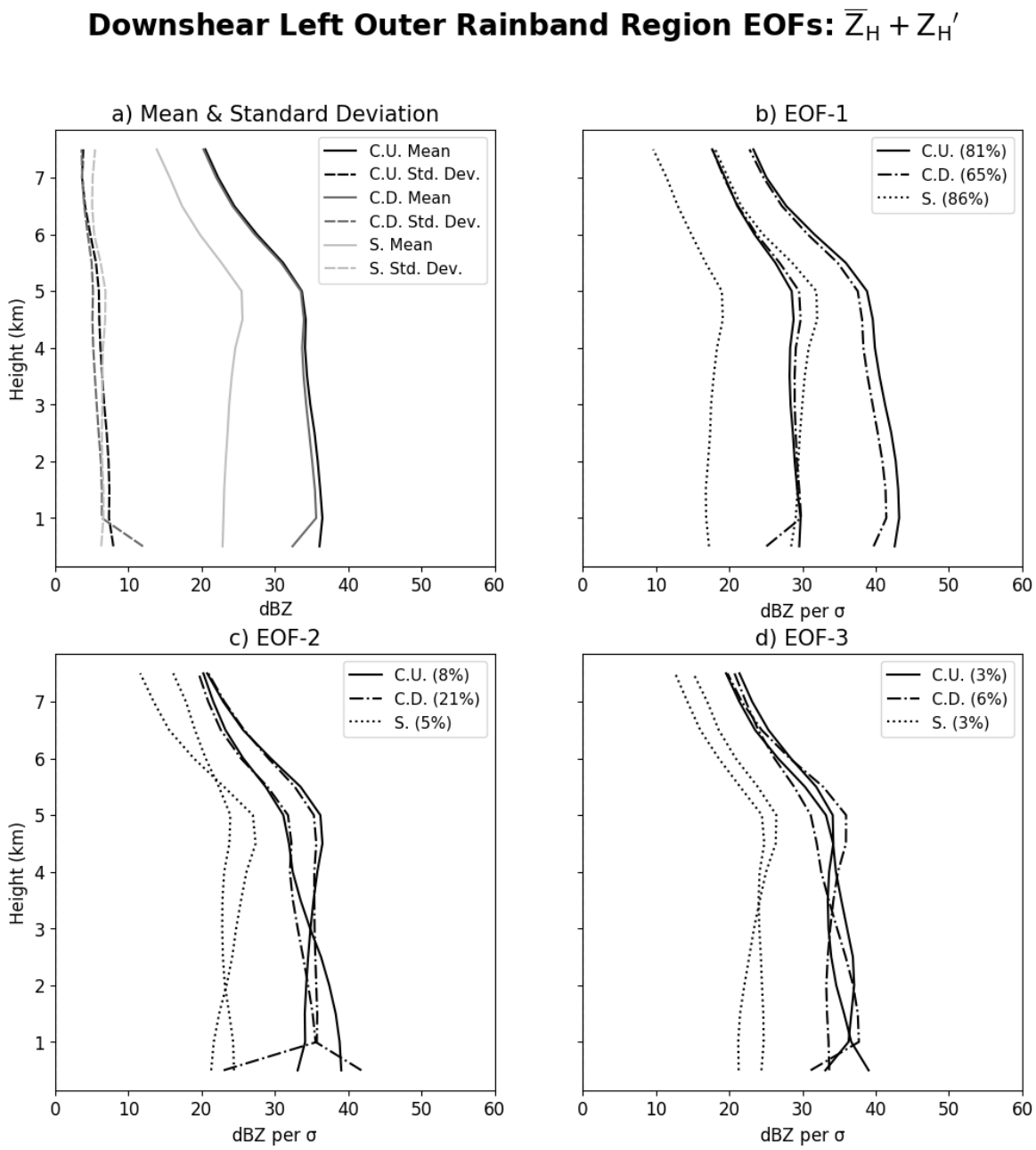

Figure 57: a) The mean (solid) and standard deviation (dashed) profiles for downshear left outer rainband radar reflectivity (Z_H) in the convective updraft (black; n=1824), convective downdraft (gray; n=2156), and stratiform (light gray; n=31421) regions. **b)** EOF-1 profiles for downshear left outer rainband radar reflectivity in the convective updraft (solid), convective downdraft (dashed-dotted), and stratiform (dotted) regions. Corresponding variance explained percentages included in plot legend. **c)** As in b), except for EOF-2. **d)** As in b), except for EOF-3.

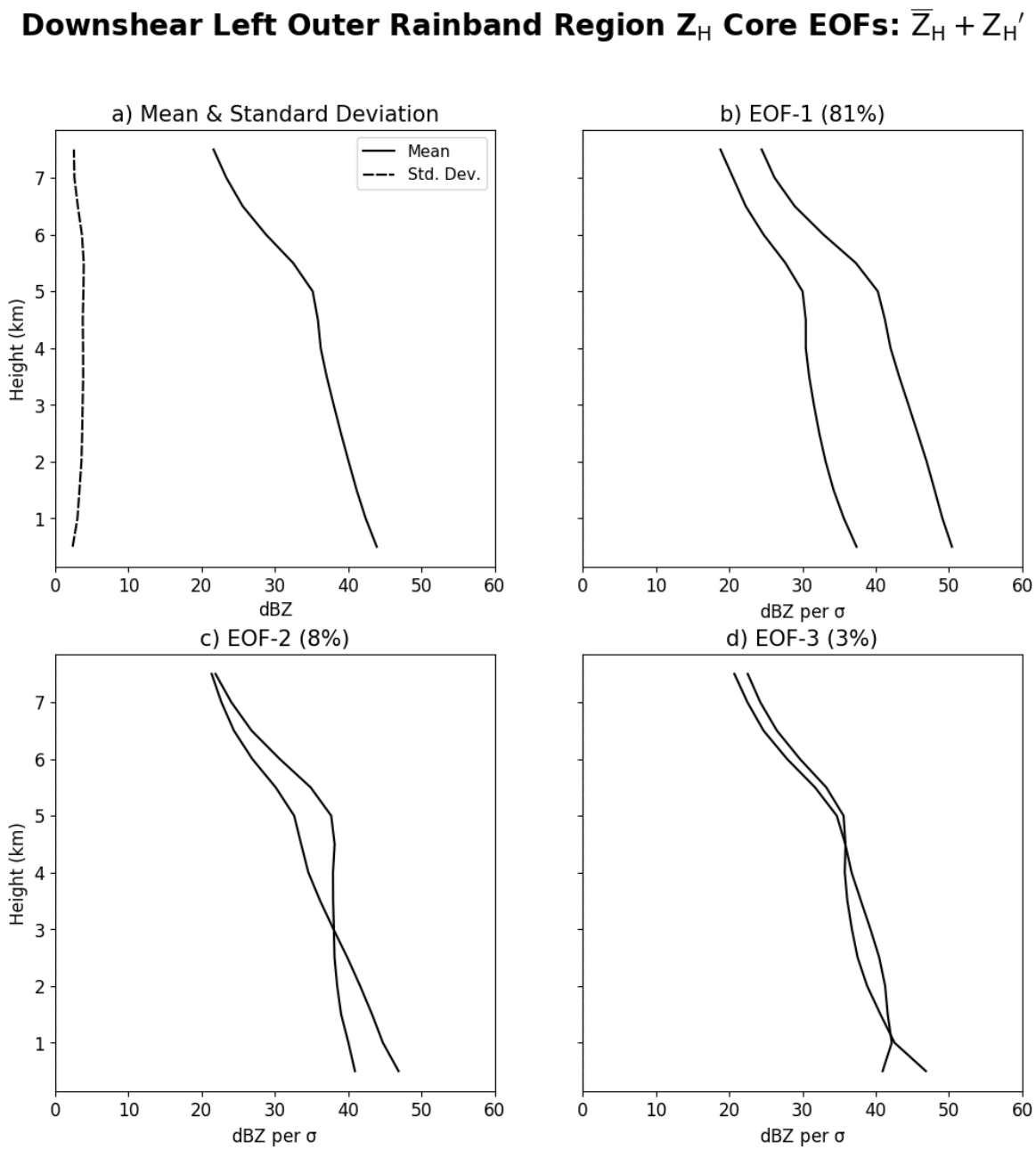

Figure 58: a) The mean (solid) and standard deviation (dashed) profiles for downshear left outer rainband radar reflectivity (Z_H) in the reflectivity cores (black; n=1824). **b)** EOF-1 profiles for downshear left outer rainband radar reflectivity in the reflectivity cores. Corresponding variance explained percentages included in plot title. **c)** As in b), except for EOF-2. **d)** As in b), except for EOF-3.

lower magnitude than the mean and the other set has a higher magnitude. For EOF-2, from Figure 57c, one of the convective profiles shows a slight increase in reflectivity with height up to 5 km, while the other shows a decrease in reflectivity with height. Above 5 km, these profiles resemble the mean. The increase in reflectivity points to the evaporation of hydrometeors at lower levels and/or melting of hydrometeors in the mid-levels. Meanwhile, the decrease in reflectivity points to a laminar reflectivity structure and/or a more shallow convective core, particularly in the convective updraft region. EOF-2 represents 8% (21%) of the variance in the convective updraft (downdraft) reflectivity. For the third EOF, displayed in Figure 57d, the convective updraft profiles are relatively upright below 5 km, while the convective downdraft profiles resemble the convective updraft profiles of EOF-2. The convective up- and downdraft EOF-3 profiles explain 3% and 6% of the variance, respectively. Because convective drafts and enhanced reflectivity are not always collocated, the convective EOFs could be influenced by stratiform-like reflectivity profiles.

Notably lower in magnitude compared to the convective mean reflectivity profiles and displayed in Figure 57a, the mean stratiform reflectivity increases in value up to 4.5-5 km before peaking and abruptly decreasing with height. This increase is likely from the evaporation of hydrometeors before they reach the lower levels, and the 5-km peak is likely the commonly observed stratiform bright band. Explaining 86% of the variance in stratiform outer rainband reflectivity and shown in Figure 57b, EOF-1 shows two profiles that share the shape of the mean but have different values. From Figures 57c–d, EOFs 2 and 3 both exhibit a profile that resembles the mean, while the other profile has a relatively upright reflectivity profile in the lower levels, which suggests a more uniform rainfall rate. These EOFs represent a collective 8% of the variance in stratiform outer rainband reflectivity. All stratiform EOFs exhibit a peak

in reflectivity near a height of 5 km, pointing to the location of the melting layer (i.e., bright banding).

Shown in Figure 58a, the mean reflectivity of the outer rainband reflectivity cores decreases with height in the low levels before decreasing more rapidly in the upper levels. This indicates the mean reflectivity field is somewhat laminar in this region. Explaining 81% of the variance and presented in Figure 58b, EOF-1 shows two profiles that resemble the mean with differing values. From Figure 58c, in addition to a profile that resembles the mean structure, EOF-2 shows a profile that is more upright in the low- to mid-levels. This points to a profile of deep convection. Lastly, from Figure 58d, EOF-3 shows variations of the mean reflectivity structure. Overall, like those of the inner rainband reflectivity cores, these EOF profiles show the outer rainband low-level >40 dBZ reflectivity maxima are not necessarily associated with convective towers.

5.3.2 Vertical Velocity

From Figure 59a, the mean convective updraft (downdraft) vertical velocity profiles show an updraft (downdraft) that increases in magnitude with height and maximizes between a height of 6-7 km. The first EOF, displayed in Figure 59b, explains 91% (94%) of the variance in the convective updraft (downdraft) vertical velocity. The two convective updraft (downdraft) profiles show both strong and weak drafts that maximize in the upper levels. From Figures 59c–d, EOFs 2 and 3 show variations of the EOF-1 profiles, where they collectively represent 7% (4%) of the variance in the convective updraft (downdraft) region.

From Figure 59a, the outer rainband stratiform mean vertical velocity is notably weaker than in the convective regions, as it is roughly 0 m s^{-1} for the entire column. EOF-1, displayed in Figure 59b, represents 64% of the variance in stratiform vertical

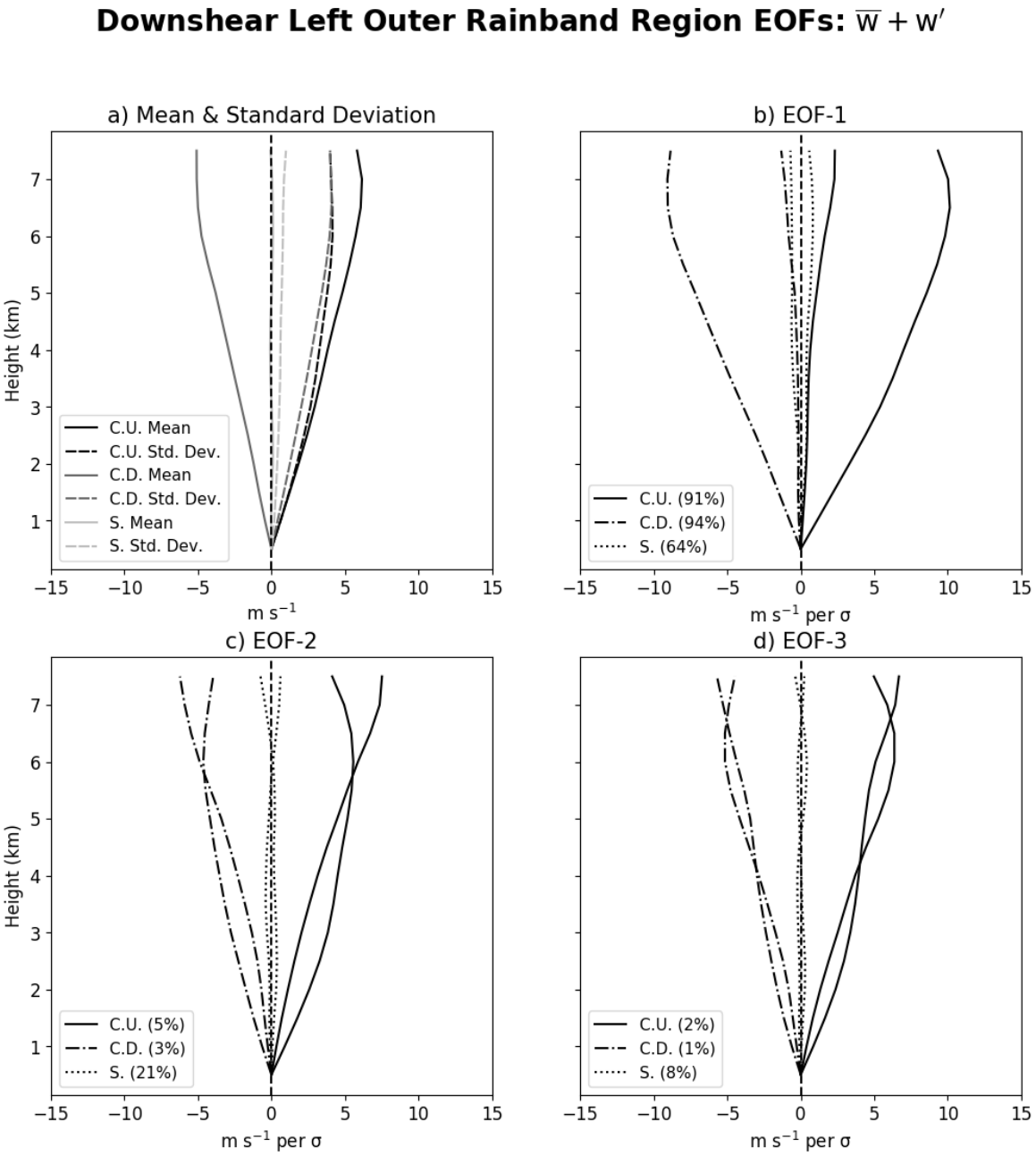

Figure 59: a) The mean (solid) and standard deviation (dashed) profiles for downshear left outer rainband vertical velocity (w) in the convective updraft (black; n=1260), convective downdraft (gray; n=1439), and stratiform (light gray; n=13706) regions. **b)** EOF-1 profiles for downshear left outer rainband vertical velocity in the convective updraft (solid), convective downdraft (dashed-dotted), and stratiform (dotted) regions. Corresponding variance explained percentages included in plot legend. **c)** As in b), except for EOF-2. **d)** As in b), except for EOF-3.

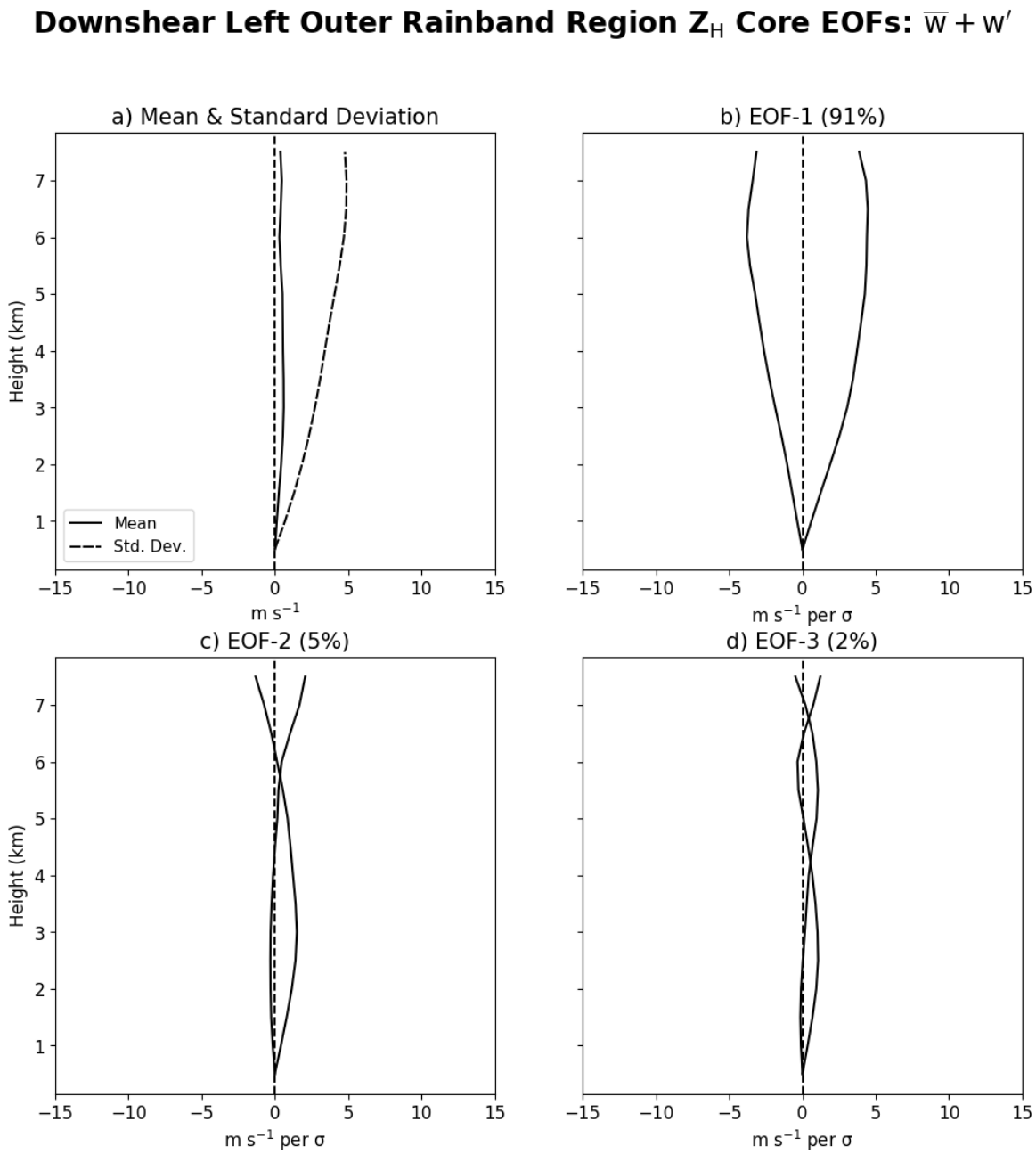

Figure 60: a) The mean (solid) and standard deviation (dashed) profiles for downshear left outer rainband vertical velocity (w) in the reflectivity cores (n=1260). **b)** EOF-1 profiles for downshear left outer rainband vertical velocity in the reflectivity cores. Corresponding variance explained percentages included in plot title. **c)** As in b), except for EOF-2. **d)** As in b), except for EOF-3.

velocity and shows a weak columnar updraft and weak columnar downdraft. This suggests that most of the vertical velocity profiles in the stratiform outer rainband region are solely updrafts or downdrafts. Supported by the broad area of weak low-level reflectivity in Figure 19, these stratiform downdrafts could be indicative of a feature like the squall line transition zone (Smull and Houze Jr 1985; Biggerstaff and Houze 1991). Explaining 21% of the variance in stratiform vertical velocity and shown in Figure 59c, EOF-2 shows an updraft (downdraft) that transitions to a downdraft (updraft) at a height of 6 km. Similarly, from Figure 59d, EOF-3 displays a low-level updraft (downdraft) that transitions to a downdraft (updraft) in the mid-levels, and then changes back to an updraft (downdraft) in the upper levels. EOFs 2 and 3 validate the stacked downdraft-updraft structure described by Didlake and Houze (2013b), but the EOF analysis reveals it is not the most commonly observed stratiform vertical velocity structure in this TC.

The mean vertical velocity in the outer rainband reflectivity cores is displayed in Figure 60a and shows mean weak upward motion that remains relatively constant with height. From Figure 60b, the EOF-1 profiles explain 91% of the variance and show both an updraft and a downdraft that increase in magnitude with height and maximize between 6-7 km. Representing 5% of the variance and displayed in Figure 60c, the EOF-2 profiles show low-level upward (downward) motion that transitions to downward (upward) motion in the upper levels. Lastly, from Figure 60d, the profiles for the third EOF alternate between upward and downward motion. In general, these EOFs show the outer rainband reflectivity cores are associated with updrafts as well as downdrafts.

5.3.3 Radial Velocity

From Figure 61a, the mean radial velocity profiles for the outer rainband convective regions are similar, depicting low-level radial inflow that transitions to radial outflow above a height of 4 km. Following the shape of the mean profile and shown in Figure 61b, the convective EOF-1 profiles show both shallow and deep inflow, which is similar to the findings for the inner rainband and eyewall regions. These profiles explain 70% (69%) of the variance in outer rainband convective updraft (downdraft) radial velocity. From Figures 61c–d, EOF-2 and EOF-3 show variations of the low-level inflow and upper-level outflow structure, where the inflow-outflow transition occurs between 3-5 km for every profile. These EOFs represent a combined 24% (25%) of the variance for the convective updraft (downdraft) region.

The mean stratiform radial velocity, shown in Figure 61a, is comparable to that of the convective regions, except the low-level inflow is slightly weaker. EOF-1, explaining 82% of the variance and presented in Figure 61b, exhibits profiles that range from shallow ($\sim$1 km) to deep ($\sim$6.5 km) radial inflow beneath radial outflow. From Figures 61c–d, the second and third EOFs show a similar structure, although the inflow-outflow transition ranges from 2-4.5 km in height. These EOFs represent a collective 14% of the variance.

The mean radial velocity structure in the outer rainband reflectivity cores, displayed in Figure 62a, shows low-level radial inflow that changes to radial outflow at a height of 3.5 km. Shown in Figure 62b, similar to the eyewall and inner rainband reflectivity cores, EOF-1 shows profiles with both deep and shallow inflow. In this case, the deep inflow is stronger than the shallow inflow. These profiles explain 67% of the variance. From Figures 62c–d, the inflow depth for EOFs 2 and 3 is contained between 2-4 km

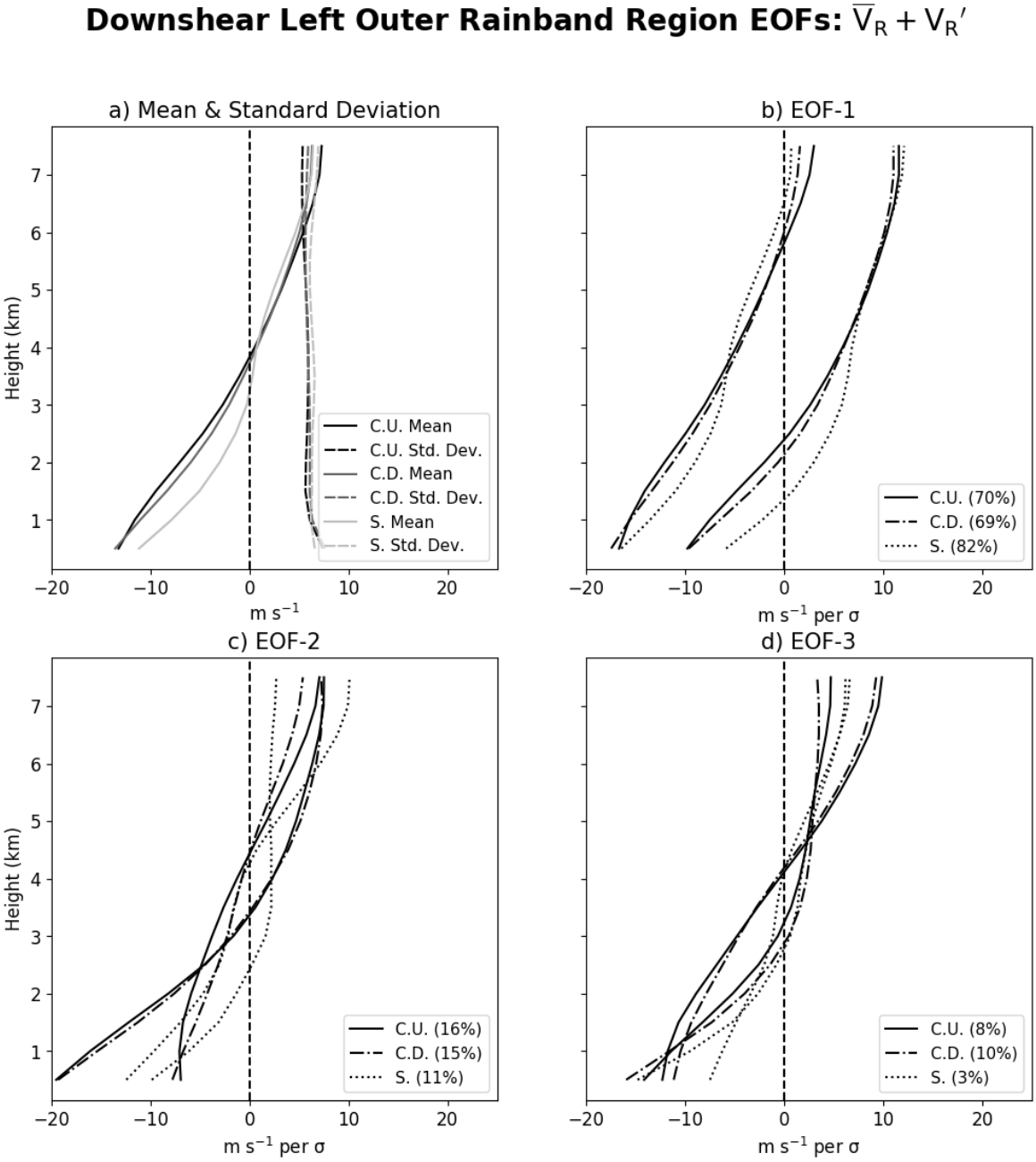

Figure 61: As in Figure 59, but for radial velocity.

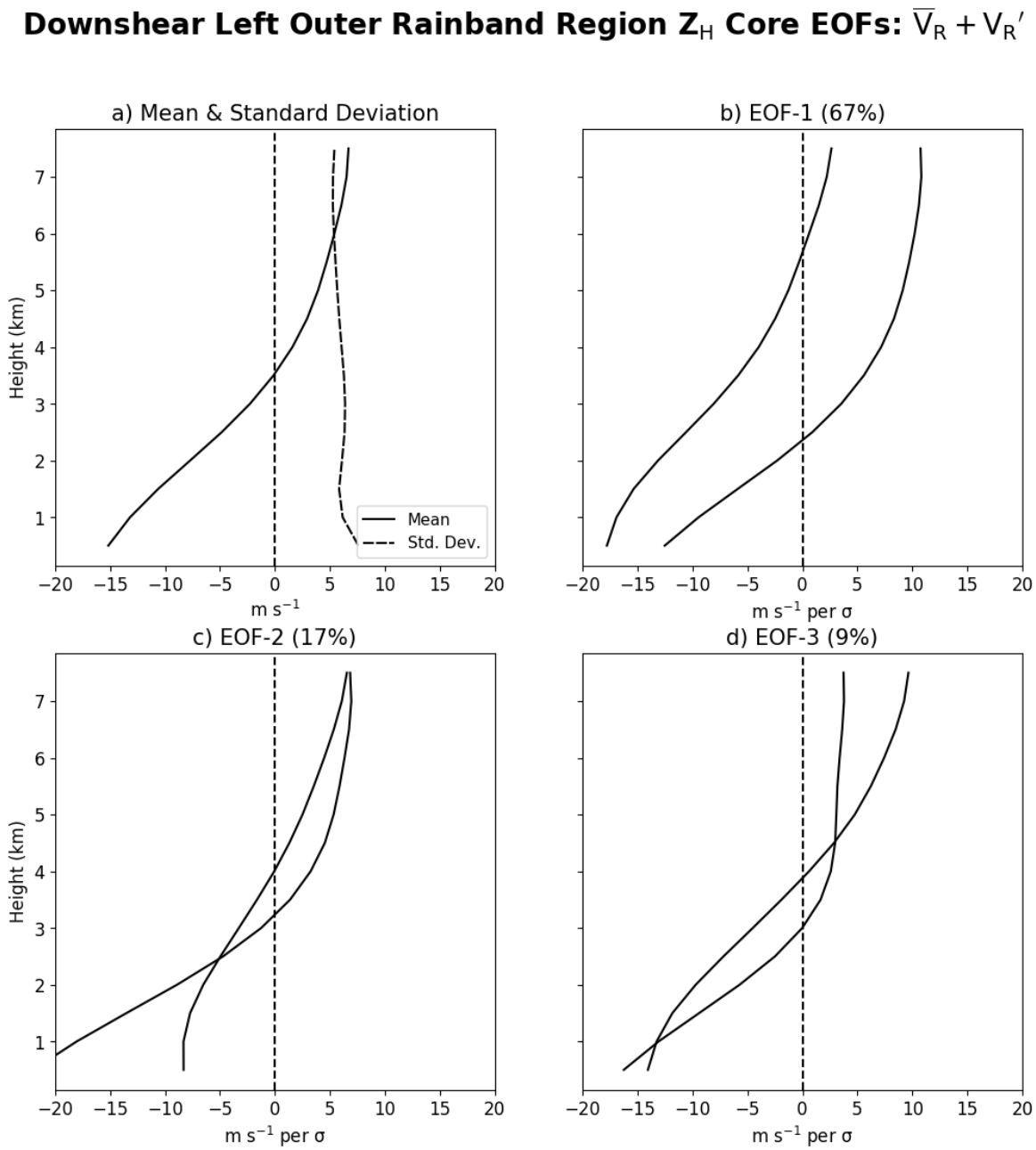

Figure 62: a) The mean (solid) and standard deviation (dashed) profiles for downshear left outer rainband radial velocity (w) in the reflectivity cores (n=1428). **b)** EOF-1 profiles for downshear left outer rainband radial velocity in the reflectivity cores. Corresponding variance explained percentages included in plot title. **c)** As in b), except for EOF-2. **d)** As in b), except for EOF-3.

and the variance in radial velocity strength is pronounced. These EOFs represent a combined 26% of the variance.

5.3.4 Azimuthal Velocity

From Figure 63a, the mean azimuthal velocity profiles for the convective regions are lower in magnitude than those of the eyewall and inner rainband regions, which is expected based on angular momentum arguments. The maximum mean azimuthal velocity occurs between a height of 1-3 km, pointing to the likelihood of a tangential jet. Compared to the eyewall and inner rainband regions, the vertical azimuthal velocity gradient is weaker in this region. The EOF-1 profiles for both convective regions, shown in Figure 63b, resemble the mean profiles, where one set of profiles is lower in value and the other is higher. These profiles explain 79% and 82% of the variance in the convective updraft and downdraft regions, respectively. Also resembling the mean and displayed in Figure 63c, all convective EOF-2 profiles are nearly identical above a height of 2 km, while the near-surface magnitudes vary. These profiles represent 11% (8%) of the variance in convective updraft (downdraft) azimuthal velocity. For the third EOF, shown in Figure 63d, the convective profiles look similar, except the tangential jet is more pronounced in one of them. These profiles explain 5% of the variance for each of the convective regions.

From Figure 63a, the mean shape of the stratiform azimuthal velocity profile is similar to that of the convective regions, but the overall magnitude is lower. This suggests the stratiform profile largely embodies the background azimuthal velocity of the TC and tangential jets are absent in the stratiform region. From Figure 63b, the shape of the stratiform EOF-1 profiles resembles that of the mean, where one profile is slightly lower in value and the other is slightly higher. EOF-1 represents 85% of the

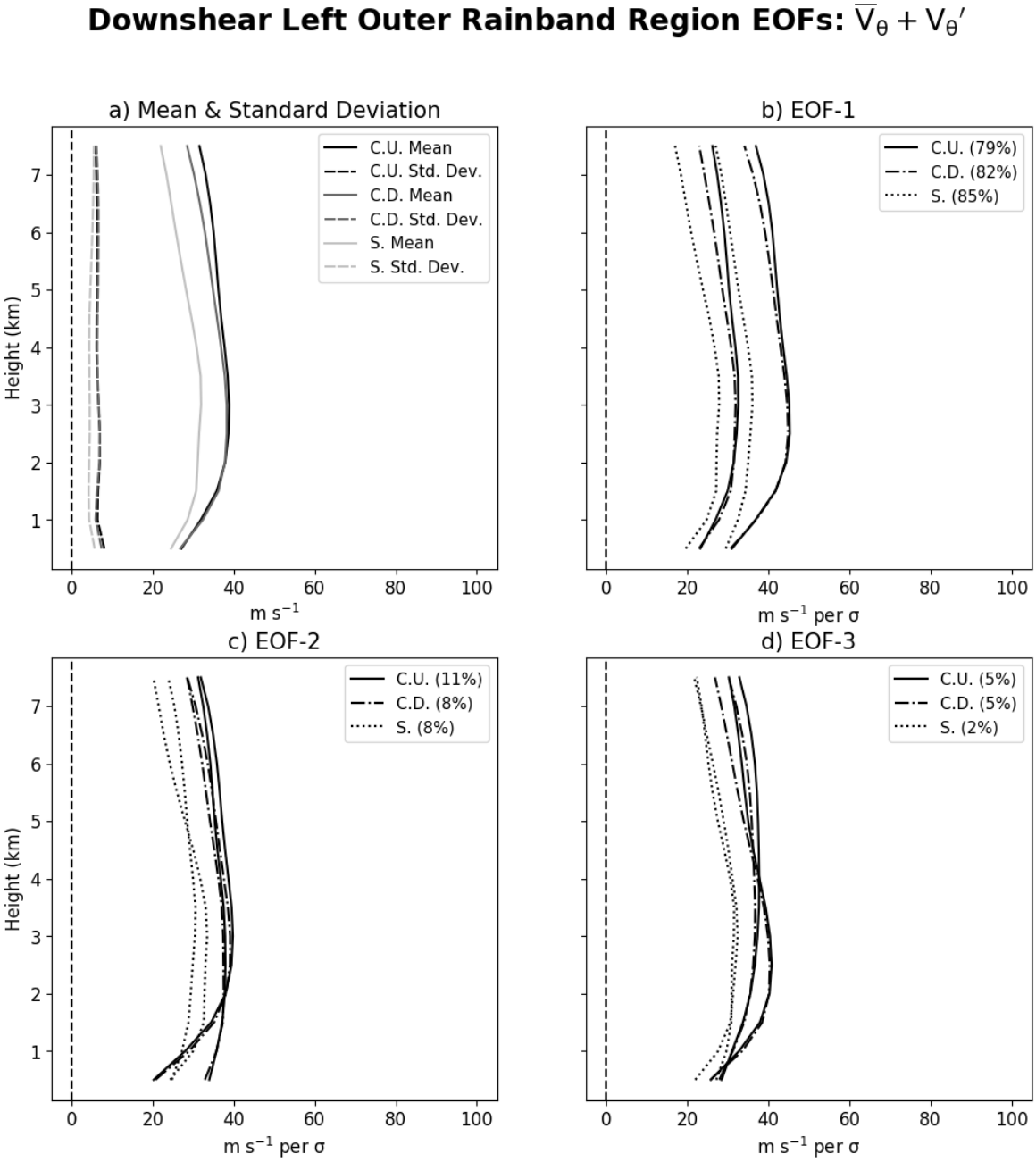

Figure 63: As in Figure 59, but for azimuthal velocity.

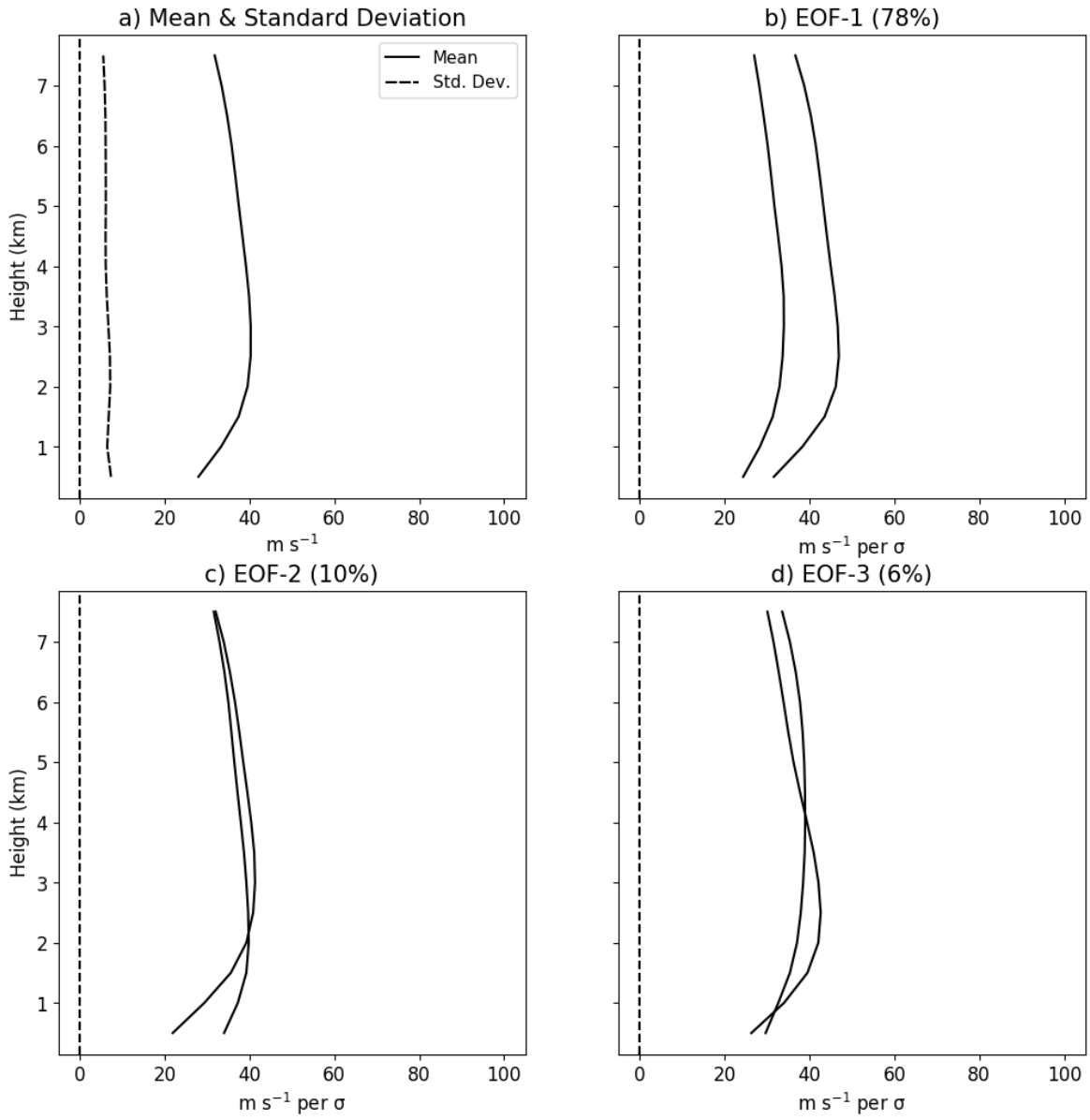

Figure 64: As in Figure 62, but for azimuthal velocity.

variance. Representing a combined 10% of the variance and displayed in Figures 63c–d, the EOF-2 and EOF-3 profiles are similar to the mean, except for some variations in the values.

The mean azimuthal velocity profile for the outer rainband reflectivity cores, shown in Figure 64a, resembles that of the outer rainband convective draft regions. That is, there exists a mean azimuthal velocity maximum in the lower levels and the azimuthal velocity magnitude decreases above that maximum. The EOFs, displayed in Figures 64b–d, all parallel those of the convective draft regions.

5.3.5 Relative Vorticity

The mean convective updraft vertical vorticity profile, displayed in Figure 65a, shows low-level cyclonic vorticity that briefly transitions to weak anticyclonic vorticity and ultimately changes back to weak cyclonic vorticity in the mid- to upper levels. Similarly, the mean convective downdraft vertical vorticity is positive in the low-levels and goes to zero with height. Shown in Figure 65b, EOF-1 for both convective regions displays both a cyclonic and anticyclonic vorticity profile that each near zero in the upper levels. These profiles each explain 36% (37%) of the variance in outer rainband convective updraft (downdraft) vertical vorticity. This EOF suggests the convective drafts in the outer rainbands both advect positive and negative vorticity. Explaining 30% and 26% of the variance for convective updraft and downdraft regions, respectively, and shown in Figure 65c, EOF-2 shows low-level cyclonic (anticyclonic) vorticity that transitions to anticyclonic (cyclonic) vorticity just below a height of 3 km. From Figure 65d, EOF-3 shows both a mostly cyclonic (anticyclonic) vorticity profile with a brief transition to anticyclonic (cyclonic) vorticity in the low- to mid-levels. These profiles represent 15% and 16% of the variance in convective updraft and downdraft vertical vorticity, respectively. As the EOFs increase in number, the oscillation between anticyclonic

and cyclonic vorticity with height increases as well. This is evident across EOFs 4-6, displayed in Figures 66a–c, which explain a combined 13% (15%) of the variance in outer rainband convective updraft (downdraft) relative vorticity.

From Figure 65a, at the lowest level, the stratiform mean relative vorticity is positive before briefly transitioning to anticyclonic vorticity. Above this, the vorticity is near-zero. Explaining 39% of the variance in outer rainband stratiform vertical vorticity and presented in Figure 65b, EOF-1 exhibits near-zero vorticity in the low- to mid-levels and either cyclonic or anticyclonic vorticity in the upper-levels, depending on the profile. In Figure 65c, near-zero low-level vorticity is also exhibited in EOF-2, where it changes to cyclonic (anticyclonic) vorticity in the mid-levels and changes again to anticyclonic (cyclonic) vorticity in the upper levels. These profiles represent 19% of the variance. Shown in Figure 65d, the third EOF shows low-level cyclonic or anticyclonic vorticity, depending on the profile, that goes to zero for the rest of the profile. These EOF profiles represent 17% of the variance. Like the convective EOFs and shown in Figures 66a–c, EOFs 4-6 for the stratiform region increase in oscillation between anticyclonic and cyclonic vorticity. These EOFs represent a combined 16% of the variance in stratiform outer rainband relative vorticity.

Shown in Figure 67a, the mean relative vorticity structure in the outer rainband reflectivity cores consists of columnar cyclonic vorticity that maximizes in the lower levels. Explaining 38% of the variance and displayed in Figure 67b, EOF-1 shows profiles of both columnar anticyclonic and columnar cyclonic vorticity. This suggests both anticyclonic and cyclonic vorticity are transported within reflectivity cores. From Figures 67c–d and Figures 68a–b, as the remaining EOFs increase in number, the number of times the profiles oscillate between anticyclonic and cyclonic vorticity increases.

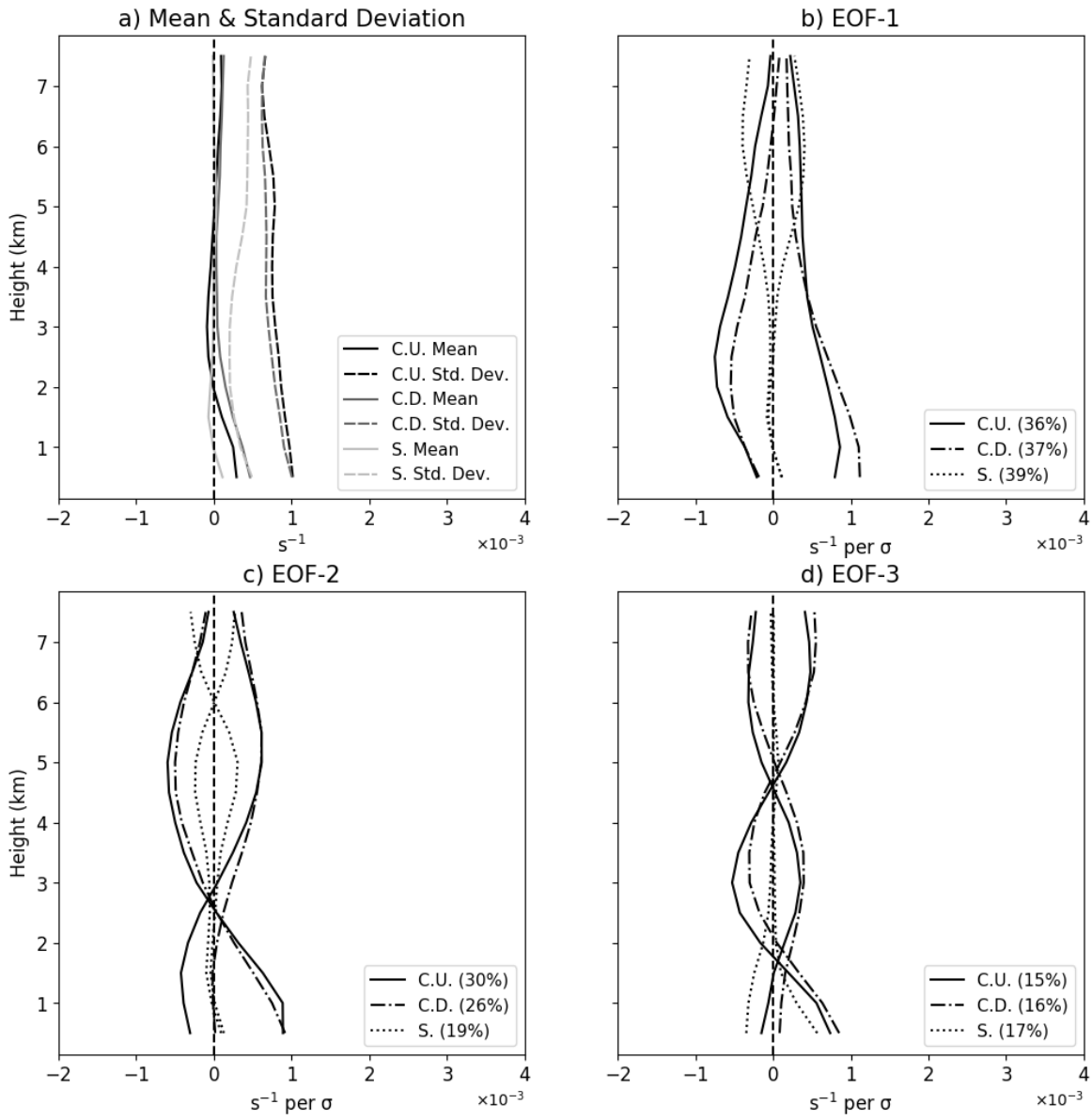

Figure 65: a) The mean (solid) and standard deviation (dashed) profiles for downshear left outer rainband relative vorticity (ζ) in the convective updraft (black; n=994), convective downdraft (gray; n=1172), and stratiform (light gray; n=9101) regions. **b)** EOF-1 profiles for downshear left outer rainband relative vorticity in the convective updraft (solid), convective downdraft (dashed-dotted), and stratiform (dotted) regions. Corresponding variance explained percentages included in plot legend. **c)** As in b), except for EOF-2. **d)** As in b), except for EOF-3.

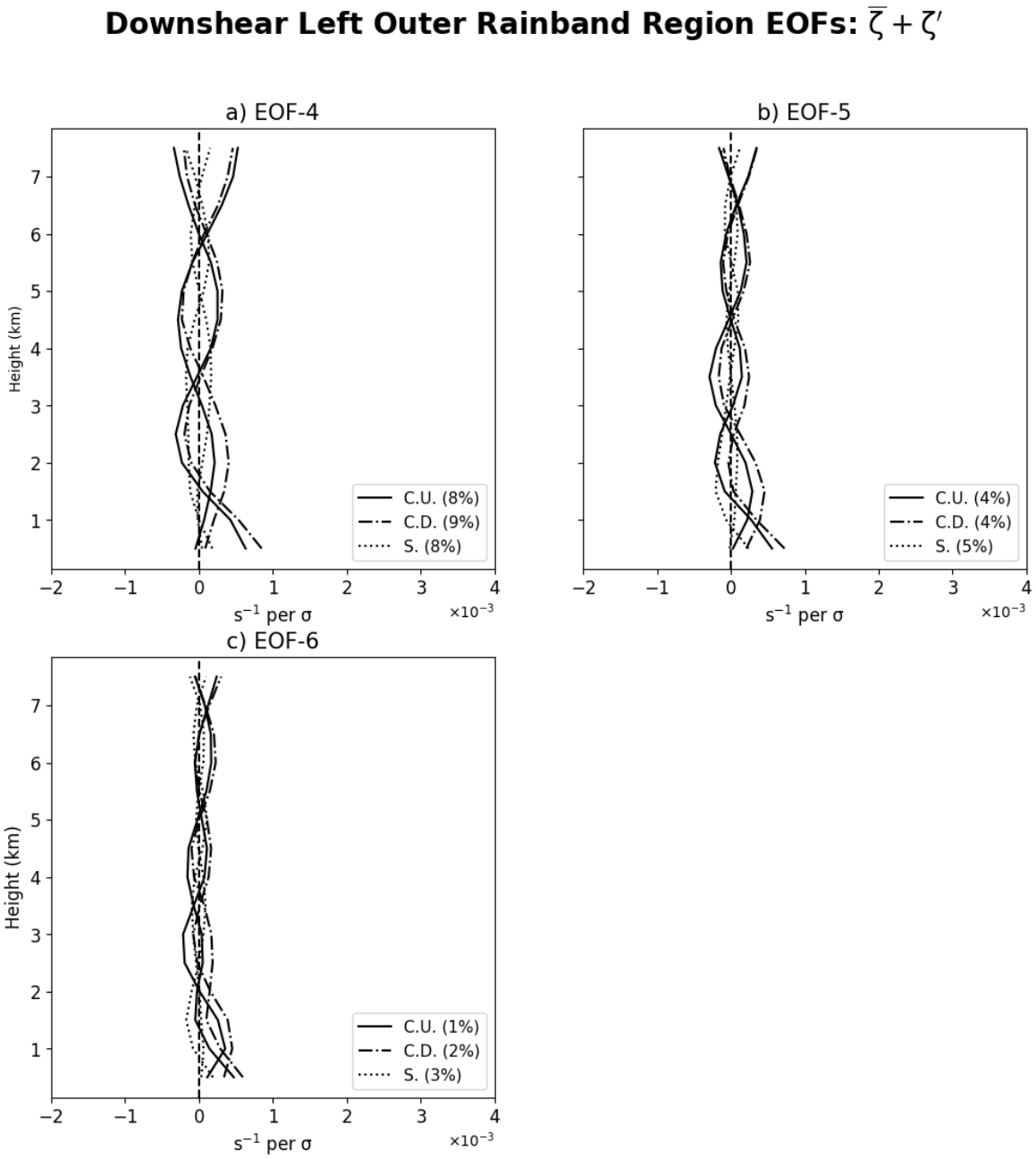

Figure 66: A continutation of the EOFs from Figure 65, where **a)** is EOF-4, **b)** is EOF-5, and **c)** is EOF-6.

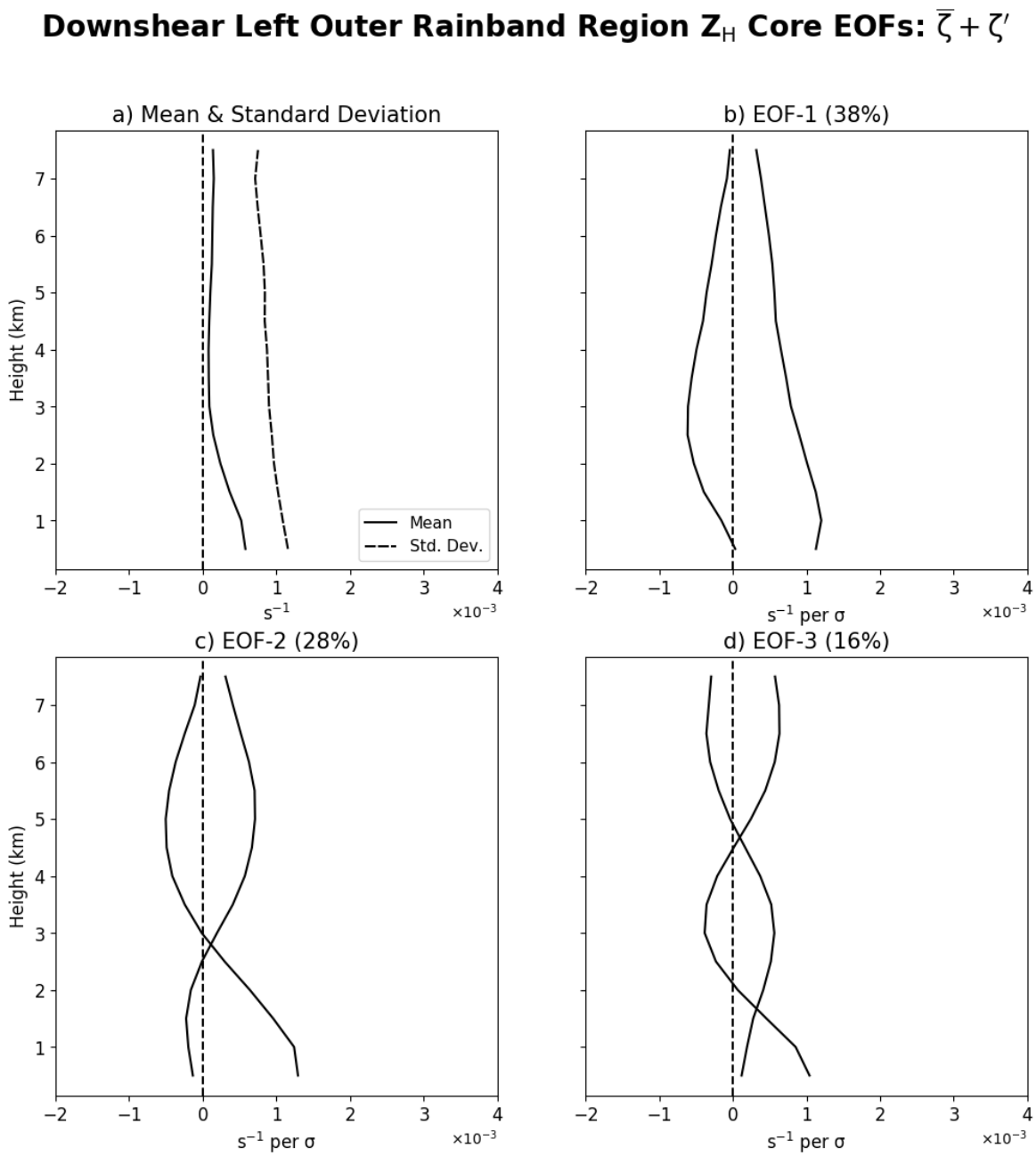

Figure 67: a) The mean (solid) and standard deviation (dashed) profiles for downshear left outer rainband relative vorticity (ζ) in the reflectivity cores (black; n=1182). **b)** EOF-1 profiles for downshear left outer rainband relative vorticity in the reflectivity cores. Corresponding variance explained percentages included in plot title. **c)** As in b), except for EOF-2. **d)** As in b), except for EOF-3.

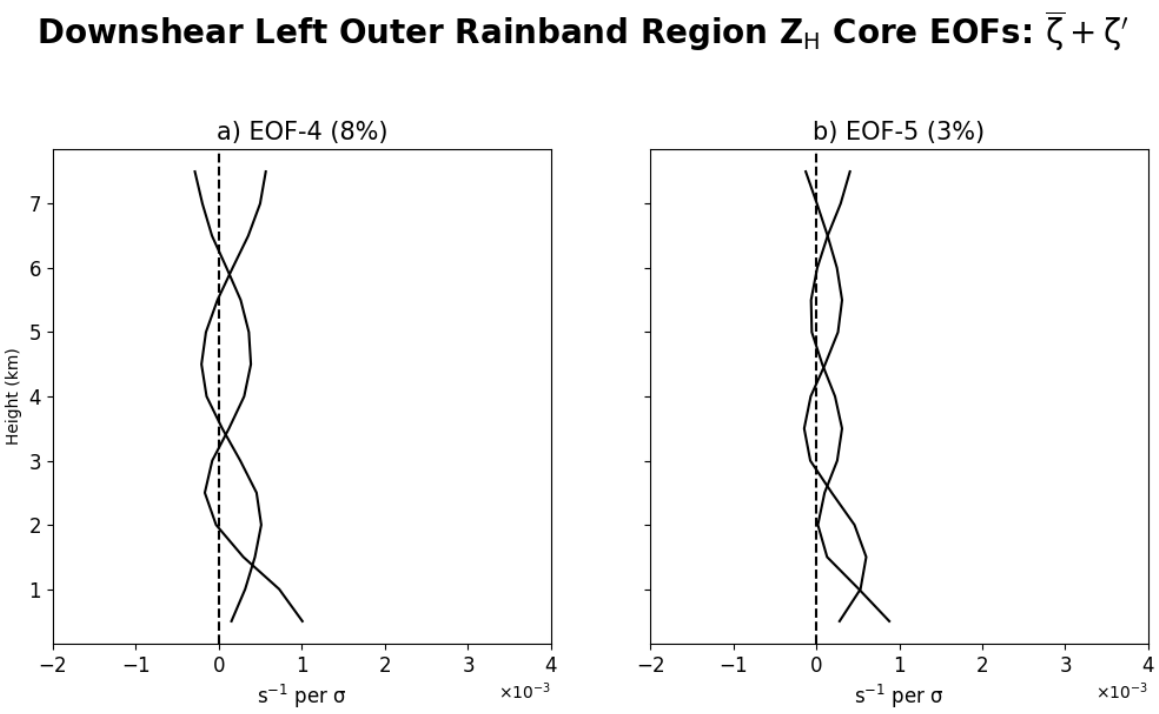

Figure 68: A continutation of the EOFs from Figure 67, where **a)** is EOF-4 and **b)** is EOF-5.

5.3.6 Divergence

From Figure 69a, mean convergence is observed for the convective updraft region, where the maximum occurs at the lowest level and decreases with height. While the mean profile does not feature divergence, as expected from mass continuity, it is likely above the maximum sampling height. EOF-1, displayed in Figure 69b, for the convective updraft region shows two variations of columnar convergence, where one profile becomes divergent in the upper levels and the other shows near-zero convergence in the low- to mid-levels. The upper-level divergence is consistent with the updraft weakening in Figure 59. The EOF-1 profiles represent 48% of the variance. Shown in Figure 69c and representing 22% of the variance, EOF-2 shows two profiles of low-level convergence that transition to divergence at heights of 3 km and 7 km, where updraft weakening is evident in Figure 59. Explaining 12% of the variance and presented in Figure 69d,

the EOF-3 profiles show convergence at the lower levels. One profile is convergent throughout the column, while the other profile transitions to divergence in the mid- to upper levels, representing notable updraft weakening. Similarly, explaining <13% of the variance and displayed in Figures 70a–c, EOFs 4-6 show profiles that either remain convergent throughout the whole profile or transition to divergence in the upper levels. Overall, the EOFs suggest that outer rainband convective updrafts have varying divergence, which impacts the relative strength of updrafts.

For the convective downdraft region, mean divergence exists throughout the profile in Figure 69a, where the maximum occurs in the lower levels and the minimum occurs in the upper levels. This mean profile is largely consistent with mass continuity requirements, as divergence occurs beneath the downdrafts and convergence likely occurs above the limits of these analyses. From Figure 69b, EOF-1 shows both a profile of deep divergence and a profile of low-level alternating divergence and convergence with upper-level divergence. These profiles represent 47% of the variance. EOF-2, explaining 18% of the variance and displayed in Figure 69c, shows one profile of divergence limited to the lowest 5 km, which marks where the downdraft begins weakening with height. The other EOF-2 profile shows deep divergence. Similarly, from Figure 69d, the third EOF shows both columnar divergence as well as divergence capped by convergence at a height of 6 km. These profiles represent 15% of the variance. From Figures 70a–c, EOFs 4-6 show profiles of either exclusive divergence or divergence with upper-level convergence. Explaining a combined 15% of the variance, these profiles point to the existence of downdrafts with uniform strength.

The mean stratiform profile, shown in Figure 69a, shows low- and upper-level convergence and mid-level divergence. Displayed in Figure 69b and representing 28%

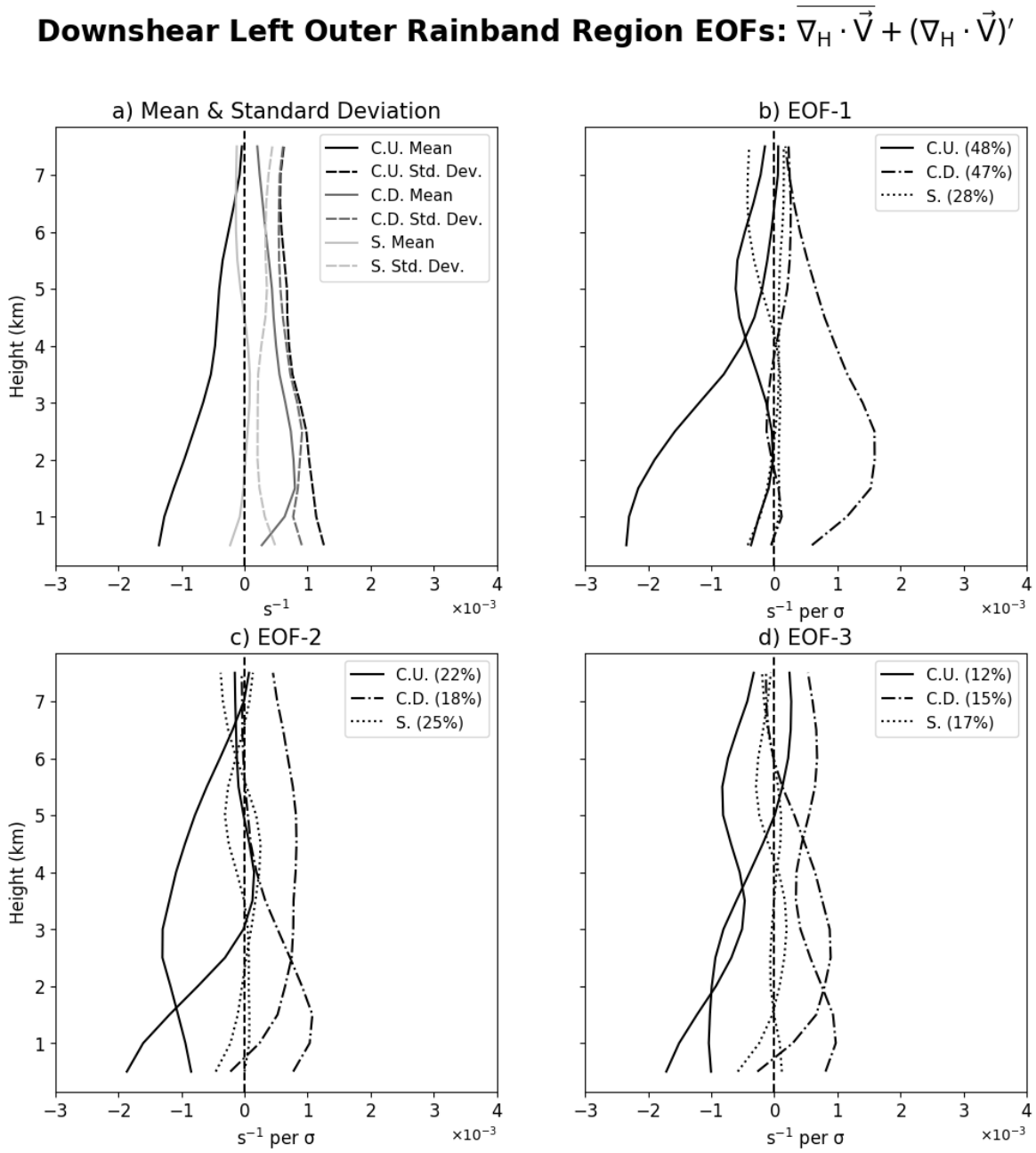

Figure 69: a) The mean (solid) and standard deviation (dashed) profiles for downshear left outer rainband divergence ($\nabla_H \cdot \vec{V}$) in the convective updraft (black; n=991), convective downdraft (gray; n=1168), and stratiform (light gray; n=9094) regions. **b)** EOF-1 profiles for downshear left outer rainband divergence in the convective updraft (solid), convective downdraft (dashed-dotted), and stratiform (dotted) regions. Corresponding variance explained percentages included in plot legend. **c)** As in b), except for EOF-2. **d)** As in b), except for EOF-3.

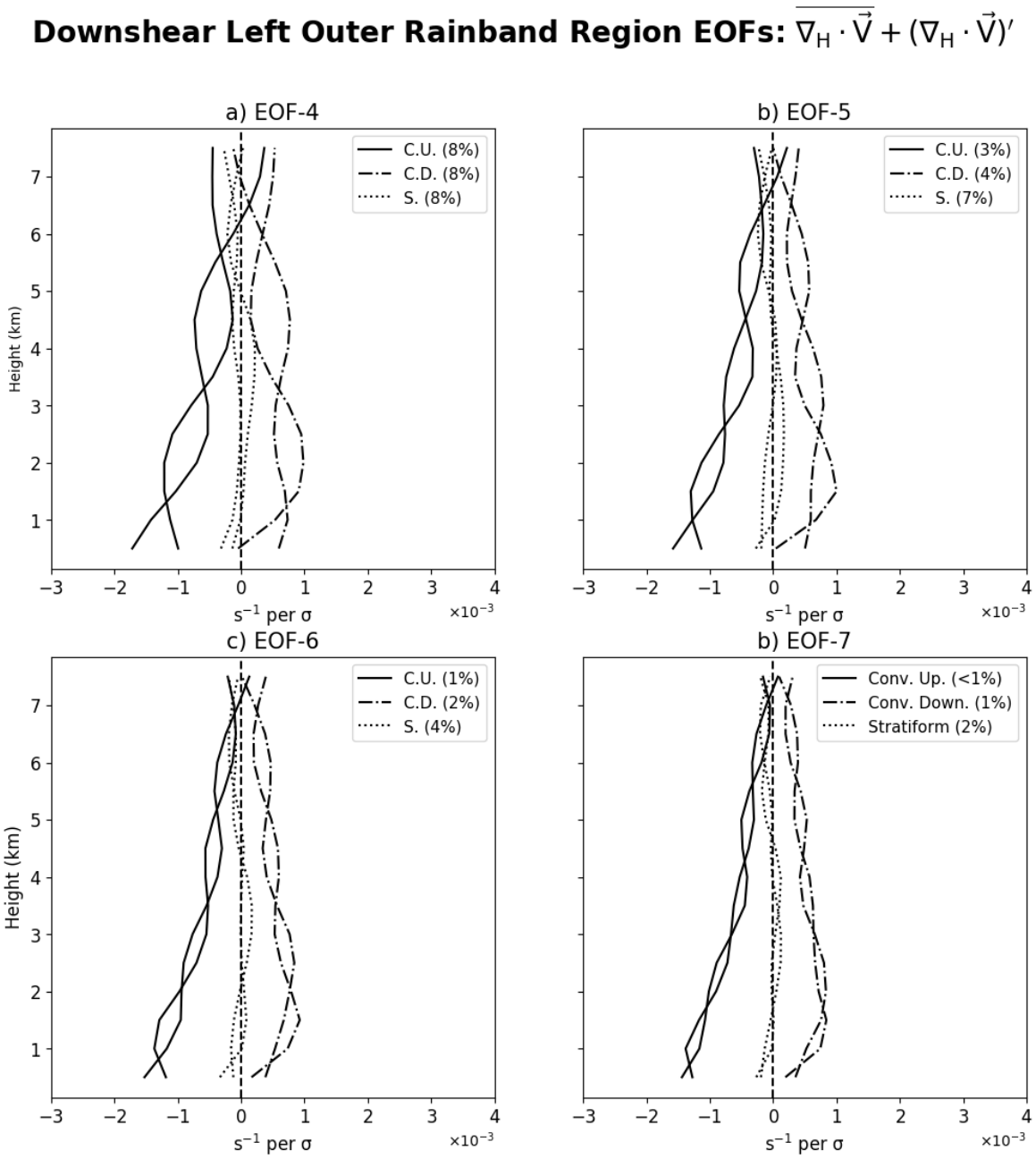

Figure 70: A continutation of the EOFs from Figure 69, where **a)** is EOF-4, **b)** is EOF-5, **c)** is EOF-6, and **d)** is EOF-7.

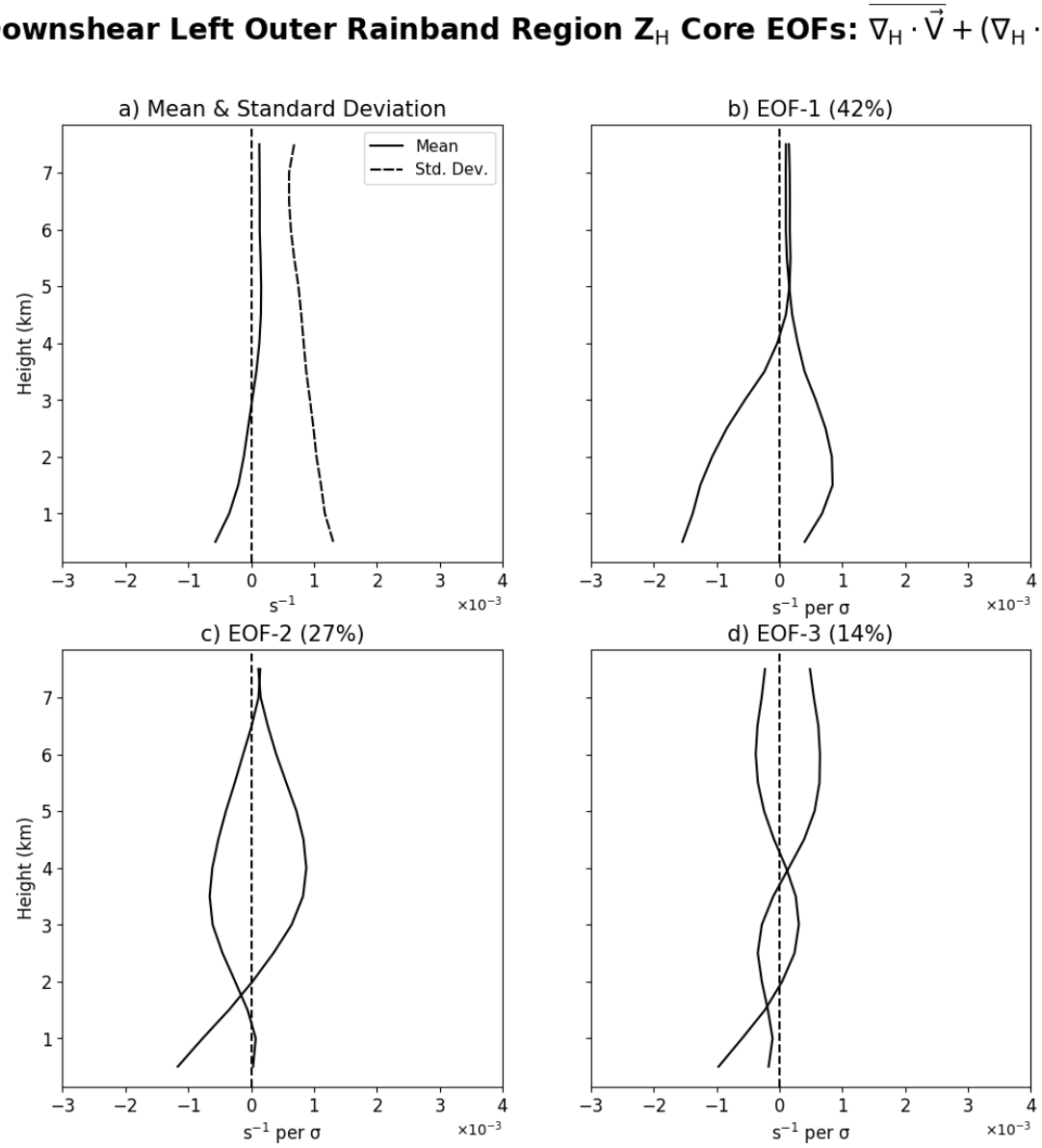

Figure 71: a) The mean (solid) and standard deviation (dashed) profiles for downshear left outer rainband divergence ($\nabla_H \cdot \vec{V}$) in the reflectivity cores (n=1183). **b)** EOF-1 profiles for downshear left outer rainband divergence in the reflectivity cores. Corresponding variance explained percentages included in plot title. **c)** As in b), except for EOF-2. **d)** As in b), except for EOF-3.

Downshear Left Outer Rainband Region Z_H Core EOFs: $\overline{\nabla_H \cdot \vec{V}} + (\nabla_H \cdot \vec{V})'$

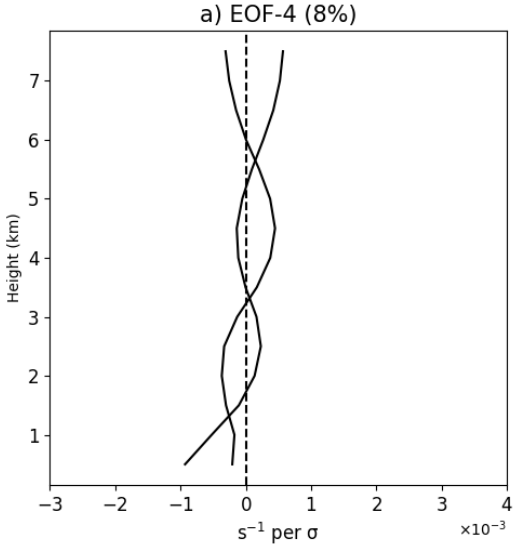

Figure 72: A continutation of the EOFs from Figure 71, where **a)** is EOF-4.

of the variance, one stratiform EOF-1 profile shows low-level convergence with divergence above it while the other profile shows weak low-level divergence that is capped by upper-level convergence. These profiles point to draft weakening, which is observed in Figure 59. Like the mean structure and shown in Figure 69c, EOF-2 displays a mostly convergent profile with mid-level divergence, and vice versa. These profiles explain 25% of the variance. EOF-3, displayed in Figure 69d, shows mid- to upper-level convergence (divergence) stacked over low- to mid-level divergence (convergence). EOF-3 represents 17% of the variance. From Figures 70a–c, EOFs 4-6 show variations of both low- to mid-level divergence and convergence in addition to upper-level convergence and represent a combined 21% of the variance in stratiform outer rainband divergence. Overall, the changes between convergence and divergence are consistent with the draft weakening and draft sign changes observed in Figure 59.

Figures 71a–d and Figure 72a show the mean, standard deviation, and EOF profiles for outer rainband reflectivity core divergence. The mean profile consists of convergence below a 3-km height that is capped by divergence, suggesting the outer rainband reflectivity core mean updrafts weaken in the low- to mid-levels. This is confirmed by Figure 60. The first EOF explains 42% of the variance and shows one profile of columnar divergence and another profile of low-level convergence that transitions to upper-level divergence. Low-level convergence and upper-level divergence are also present in EOF-2, although the divergence notably maximizes in the mid-levels. The other EOF-2 profile shows a mostly convergent profile with weak divergence in the lower and upper levels. Representing a collective 22% of the variance, EOF-3 and EOF-4 show profiles that oscillate between convergence and divergence.

Chapter 6

Discussion, Conclusions, and Future Work

6.1 Discussion

6.1.1 Eyewall Region

Detailed in Section 2.1.1, existing literature provides a general kinematic layout of the TC eyewall in the form of conceptual models. These models include an outwardly slanted reflectivity tower that is created in response to a secondary circulation (Jorgensen 1984; Marks and Houze 1987). This secondary circulation has been widely documented to have low-level radial inflow, a slanted updraft, and upper-level radial outflow (Jorgensen 1984; Marks and Houze 1987; Willoughby 1998). The RMW also occurs within the eyewall region, which has also been illustrated with an outward slant (Jorgensen 1984; Marks and Houze 1987). Downdrafts have also been observed to occur in the eye and below the slanted updraft (Jorgensen 1984; Marks and Houze 1987; Willoughby 1998). Lastly, a stratiform region radially outside of the eyewall convection has been identified, complete with downdrafts (updrafts) below (above) the melting layer (Marks and Houze 1987; Houze 2010).

DDA-mean azimuthal-mean eyewall vertical profiles, discussed in Section 4.1, were computed for comparison to the conceptual models, as the conceptual models were created from composite analyses. The outwardly slanted convective eyewall reflectivity

and azimuthal velocity structures, secondary circulation, and downdrafts are all evident in Figure 20. Therefore, the azimuthal-mean variables of Laura's eyewall largely agree with the conceptual models. While relative vorticity and divergence patterns are not specified in the conceptual models, Figure 20 shows enhanced cyclonic vorticity within the eyewall updraft, where divergence caps the strongest mean cyclonic vorticity. Despite the similarities between the conceptual models and this analysis, the stratiform reflectivity and vertical draft structures proposed by Marks and Houze (1987) are absent.

While the azimuthal-mean eyewall vertical profiles largely agree with the conceptual models, they do not reveal perturbations and, consequently, do not illustrate the full picture of TC eyewall kinematics. Therefore, EOF analyses are used to identify eyewall profiles that are not captured by mean-derived profiles. The deep, upright convective mean reflectivity structure is found to explain the majority of the variance in convective eyewall reflectivity, where the magnitude appears to vary more than the shape. However, the EOF analysis also identifies profiles where the convective reflectivity increases or decreases in value with height, suggesting the incidence of low-level hydrometeor evaporation and/or significant mid-level hydrometeor melting as well as laminar reflectivity structures in eyewall convection. While the stratiform reflectivity structure described by Marks and Houze (1987) is absent in the azimuthal-mean vertical profiles, it is evident in the EOF analysis. Two variations of convective drafts are found in the eyewall region, where they either increase rapidly (minimally) with height before weakening (strengthening). It is possible these drafts represent different regions of the eyewall (i.e., different radii of the slanted updraft), though further analysis would be required to confirm this. The stratiform vertical draft structure postulated by Marks and Houze (1987) is only evident in EOF-2, albeit misplaced. In fact, the mean and most of the variance are represented by the opposite structure. The low-level

radial inflow and upper-level radial outflow associated with the secondary circulation are consistent across the mean profile and all eyewall EOFs, although the EOFs suggest a range of inflow depths exist in the eyewall. Based on Figure 20c, this range likely depends on a profile's radial location. The azimuthal velocity structure depicted in the conceptual models is consistent across the mean profile and EOFs, indicating it explains most of the variance. However, another structure also exists with more of a muted vertical azimuthal velocity gradient. From the relative vorticity EOF profiles, it is evident the convective updrafts and stratiform drafts transport mostly cyclonic vorticity, while the convective downdrafts transport both. The relative vorticity for all regions is also shown to be highly variable with respect to both shape and magnitude. Lastly, as expected based on mass continuity, the eyewall convective updraft (downdraft) region is mostly convergent (divergent), while the stratiform eyewall profiles exhibit both convergence and divergence. Like the relative vorticity profiles, the eyewall divergence profiles vary substantially in shape and magnitude. Regarding the eyewall reflectivity cores, their EOF profiles largely resemble the shapes of those of the convective draft regions, though the values are different. The eyewall reflectivity core EOFs also reveal the presence of both downdrafts and updrafts, rather than exclusively updrafts.

6.1.2 Inner Rainband Region

The inner rainband conceptual models of Didlake and Houze (2013a) and Barron et al. (2022), shown in Section 2.1.2, are less detailed than those of the eyewall. These models highlight differences between the inner and outer rainbands as well as assign quadrant-dependent secondary circulation patterns to inner rainband convective updrafts. Specifically, at smaller radii, both low-level radial inflow and updrafts were found to be more shallow and tangential jets were found to be weaker (Didlake and

Houze 2013a). Based on findings from Barron et al. (2022), the inner rainband convective updrafts are expected to exhibit both "in-up-out" and "out-up-out" circulation patterns, as the downshear left quadrant is exclusively studied in this analysis.

To evaluate the validity of these conceptual model features, DDA-mean azimuthal-mean vertical profiles were created and analyzed in Section 4.2. Unlike in the conceptual models, convective cores are not distinguishable in Figure 21. Rather, the reflectivity field is relatively laminar and a broad updraft exists across the lower levels. However, this does not disprove the existence of convection in the inner rainband region. That is, inner rainbands (i.e., convectively-coupled VRWs) have been widely described as being transient and shallow, so they are likely muted within the mean profiles. Despite the lack of explicit convective cells in the vertical profiles, a layer of mean divergence is observed to cap mean low-level convergence in Figure 21f. This points to the existence of either shallow or mid-level weakening of convection in this region. Also, while the inner rainband conceptual models are convection-specific, and therefore most of the features cannot be resolved in Figure 21, the "in-up-out" secondary circulation pattern is evident. Therefore, these profiles partially verify the findings of Barron et al. (2022).

EOF analyses were then conducted to resolve the inner rainband perturbation structures that are not apparent in the azimuthal-mean vertical profiles. Aside from the mean laminar reflectivity structure, the convective regions show more of an upright reflectivity structure, pointing to the presence of convective cores. This structure is observed in larger numbered EOFs, though, indicating deep reflectivity cores are not widely observed in the inner rainband convection. The stratiform reflectivity structure, on the other hand, is relatively uniform across the inner rainbands, revealing increasing reflectivity up to the melting layer before decreasing with height. This structure

is indicative of either low-level hydrometeor evaporation, enhanced hydrometeor melting in the low- to mid-levels, or both and also resembles a squall line transition zone (Smull and Houze Jr 1985; Biggerstaff and Houze 1991). Despite the mean shallow updrafts shown in Figure 21, the inner rainband vertical velocity EOFs show rather strong drafts, particularly in the upper levels. The structure and magnitude are similar to those of the eyewall region, likely due to the proximity of the inner rainbands to the eyewall. The vertical draft structure described by Marks and Houze (1987) does appear in EOFs 2 and 3 for the stratiform inner rainband region. However, it is shown to cap a low-level updraft, has a higher vertical placement than described, and only explains 21% of the variance. This indicates that the vertical draft structure of Marks and Houze (1987) is not dominant in the eyewall or in the inner rainband regions. Similarly, the "out-up-out" secondary circulation structure documented by Barron et al. (2022) is not evident in the EOF analysis, as only variations of the "in-up-out" pattern are apparent. The vertical structure of the inner rainband azimuthal velocity, where it is either enhanced in the lower levels or the vertical gradient is weak, is similar to that of the eyewall. However, the overall magnitude is lower as required by the conservation of angular momentum. The relative vorticity of the inner rainband convective regions exhibits a variety of structures, suggesting convective vertical vorticity is not uniform in the inner rainbands. The relative vorticity EOFs also show that both cyclonic and anticyclonic vorticity are transported by convective updrafts and downdrafts. The stratiform inner rainbands, however, have less variant vertical vorticity structures and appear to mainly be associated with cyclonic vorticity, except for some cases in the upper levels. Aside from some divergence (convergence) in the mid- to upper levels, the inner rainband convective updraft (downdraft) divergence profiles are convergent (divergent). Following the mean structure, the stratiform inner rainband divergence EOFs all show variations of low- and upper-level convergence and

mid-level divergence. Like the eyewall reflectivity cores, the inner rainband reflectivity core EOFs resemble the shape of the inner rainband convective draft EOFs, except for differing values. These differing values, however, are likely a result of the existence of updrafts and downdrafts.

6.1.3 Outer Rainband Region

TC outer rainbands have been extensively studied, and resulting conceptual models are included in Section 2.1.3. In summary, these conceptual models show an outwardly tilted reflectivity tower, stratiform regions (i.e., bright bands) on either side of the reflectivity tower, the "in-up-out" secondary circulation, a low-level downdraft, an upper-level downdraft, and tangential jets (Barnes et al. 1983; Powell 1990; Hence and Houze 2008; Didlake and Houze 2009). Compared to the inner rainband region, the outer rainband region is expected to have deeper and stronger updrafts, a stronger tangential jet, and deeper inflow (Zhang et al. 2011; Didlake and Houze 2013a; Alford et al. 2020).

Section 4.3 includes the DDA-mean azimuthal-mean vertical profiles for the outer rainband region. Unlike in the inner rainband region, reflectivity towers can be distinguished in Figure 22, where the cell at a larger radius is deeper. The mean vertical velocity associated with these towers is also slightly stronger at larger radii. Compared to the inner rainbands, the convective towers are deeper and stronger in this region, which validates findings by Didlake and Houze (2013a). Outside of the convective cells, neither bright bands associated with the stratiform melting layer nor the stratiform draft structure described by Didlake and Houze (2013b) are evident, although they are likely outweighed by the convection. The secondary circulation is, however, shown in Figure 22 and exhibits varying depths of radial inflow. The inflow depth is either equal to or deeper than that of the inner rainband region, and the inflow magnitude is

stronger, which only partially supports the findings of Didlake and Houze (2013a). The upper-level downdraft appears to be present, although it is unclear whether there is a low-level downdraft. That is, downward motion is evident in the lower levels, but its source cannot be determined. There are no clear tangential jets in Figure 22, although the radially outwardly protruding azimuthal velocity contours between heights of 2-4 km point to their likely existence.

The EOF analysis results are now discussed, as some features from the outer rainband conceptual models are absent in the azimuthal-mean vertical profiles. Deep reflectivity cores are representative of outer rainband convection, though increases and decreases in low- to mid-level reflectivity are also evident. This indicates that, in some places, hydrometeors could be evaporating in the lower levels, enhanced hydrometeor melting could be occurring in the mid-levels, and/or a laminar reflectivity structure could exist. The stratiform melting layer is evident across the EOFs, which agrees with the conceptual models. Weak and strong drafts are observed in the outer rainband convective regions, where all convective drafts appear to maximize in the upper levels. While the stratiform draft structure proposed by Didlake and Houze (2013b) is evident in some of the EOFs, it does not represent the majority of the variance. Because robust downdrafts are observed to extend into the upper levels, the upper-level downdraft feature from the conceptual models is inferred. There are no downdraft profiles limited to the lower levels from the convective draft EOFs, however they are weakly evident in the reflectivity core EOFs. Though, this low-level downdraft does not explain the majority of the variance. The "out-up-out" circulation observed by Barron et al. (2022) is still absent in all analyzed regions of the outer rainbands, as only the "in-up-out" secondary circulation is present. The radial inflow varies in depth across the EOFs, where its depth range is comparable to that of the inner rainband region. The inflow magnitude is also stronger than that of the inner rainband region.

The presence of a tangential jet in the low levels is likely and the azimuthal velocity is exclusively lower in magnitude than it is in the inner rainband region, though this is expected according to angular momentum conservation. Cyclonic and anticyclonic vorticity are both observed in all outer rainband regions, indicating the outer rainband drafts transport both. The outer rainband convective updraft (downdraft) region is mostly convergent (divergent) except for some instances of divergence (convergence) in the mid- to upper levels. Based on the vertical velocity EOFs, these changes in the sign of divergence likely correspond to draft weakening. Like the other TC regions, the outer rainband reflectivity core EOFs largely resemble those of the outer rainband convective draft regions. However, the reflectivity field is more laminar and the overall magnitudes are reduced.

6.2 Conclusions

The DDA-mean azimuthal-mean vertical profiles validated several features seen in the conceptual models. For example, in the eyewall region, the slanted reflectivity structure, slanted azimuthal velocity, slanted updraft, secondary circulation, and downdrafts were all observed. In the inner rainband region, only the secondary circulation was captured, as convective features were mostly absent. Lastly, the outer rainband vertical profile confirmed the existence of convective towers and associated updrafts, the secondary circulation, and likely the upper-level downdraft. Despite these consistencies, many features from the conceptual models were not verified by the azimuthal-mean vertical profiles. Namely, the stratiform eyewall vertical draft and reflectivity structures from Marks and Houze (1987), inner rainband convection, the "out-up-out" secondary circulation from Barron et al. (2022), outer rainband stratiform features described by

Didlake and Houze (2013b), outer rainband low-level downdrafts, and outer rainband tangential jets were not evident.

The EOF analyses identified the kinematic variability of each variable in each region of Laura. One main finding from this analysis shows the stratiform vertical draft structure described by Marks and Houze (1987) and Didlake and Houze (2013b) does not explain the majority of the variance and therefore is not dominant in any of the TC regions. The "out-up-out" secondary circulation structure documented by Barron et al. (2022) was also not captured by any of the EOFs in this analysis. The findings of Didlake and Houze (2013a) also partially conflicted with this analysis, as the inner rainbands were shown to have weaker inflow and a relatively similar inflow depth compared to the outer rainbands. Beyond their disagreement with some of the previous literature, these EOF analyses document the general structure and magnitude of perturbations within different TC regions.

6.3 Limitations and Future Work

The results of this study provide useful insight regarding both the validity of previously developed TC conceptual models and the kinematic structure of Hurricane Laura. However, because this is a case study, these results cannot be assumed to represent all TCs. Another limitation regarding this project relates to the number of available profiles for the eyewall and inner rainband regions, as the downfall of KLCH restricted the number of available dual-Doppler volumes. The comparison between the conceptual models and EOF analyses was also limited to structure and magnitude, as the radial location of the EOF profiles could not be determined.

In future studies, the methods of this analysis should be applied to other TCs. Specifically, they should be applied to TCs of varying intensity as well as different TC

shear-relative quadrants to identify whether certain processes are unique to different intensity and shear conditions. Because much of the focus in TC modeling has been on TC track and intensity (e.g., Goerss 2000; Dong and Zhang 2016), future work should also focus on how well simulations represent TC vertical structure, as a limited number of studies compare real-case simulations to vertical structure observations from land-falling TCs. This work could be completed by comparing EOF analysis output from an observed TC to the simulated version of the observed TC (e.g., the NSSL Experimental Warn-on-Forecast System). Ideally, this output would confirm whether perturbations in TC vertical structure are accurately captured by numerical simulations.

Reference List

Abarca, S. F., and K. L. Corbosiero, 2011: Secondary eyewall formation in WRF simulations of Hurricanes Rita and Katrina (2005). *Geophys. Res. Lett.*, **38**, https://doi.org/10.1029/2011gl047015.

Abdi, H., and L. J. Williams, 2010: Principal component analysis. *Wiley Interdiscip. Rev.: Comput. Stat.*, **2**, 433–459, https://doi.org/10.1002/wics.101.

Alford, A. A., M. I. Biggerstaff, and G. D. Carrie, 2019: Mobile ground-based SMART radar observations and wind retrievals during the landfall of Hurricane Harvey (2017). *Geosci. Data J.*, **6**, 205–213, https://doi.org/10.1002/gdj3.82.

Alford, A. A., J. A. Zhang, M. I. Biggerstaff, P. Dodge, F. D. Marks, and D. J. Bodine, 2020: Transition of the hurricane boundary layer during the landfall of Hurricane Irene (2011). *J. Atmos. Sci.*, **77**, 3509–3531, https://doi.org/10.1175/JAS-D-19-0290.1.

Barnes, G. M., E. J. Zipser, D. Jorgensen, and F. Marks, 1983: Mesoscale and convective structure of a hurricane rainband. *J. Atmos. Sci.*, **40**, 2125–2137, https://doi.org/10.1175/1520-0469(1983)040⟨2125:macsoa⟩2.0.co;2.

Barron, N. R., A. C. Didlake, and P. D. Reasor, 2022: Statistical analysis of convective updrafts in tropical cyclone rainbands observed by airborne Doppler radar. *J. Geophys. Res.: Atmos.*, **127**, https://doi.org/10.1029/2021jd035718.

Biggerstaff, M. I., A. A. Alford, G. D. Carrie, and J. A. Stevenson, 2021: Hurricane Florence (2018): Long duration single- and dual-Doppler observations and wind retrievals during landfall. *Geosci. Data J.*, https://doi.org/10.1002/gdj3.137.

Biggerstaff, M. I., and R. Houze, 1991: Kinematic and precipitation structure of the 10–11 June 1985 squall line. *Mon. Wea. Rev.*, **119**, 3034–3065, https://doi.org/10.1175/1520-0493(1991)119%3C3034:KAPSOT%3E2.0.CO;2.

Biggerstaff, M. I., and E.-K. Seo, 2010: An EOF-based comparison and evaluation of simulated passive microwave signatures to observations over tropical oceans. *J. Geophys. Res.: Atmos.*, **115**, https://doi.org/10.1029/2009JD013029.

Biggerstaff, M. I., E.-K. Seo, S. M. Hristova-Veleva, and K.-Y. Kim, 2006: Impact of cloud model microphysics on passive microwave retrievals of cloud properties. Part I: Model comparison using EOF analyses. *J. Appl. Meteor. Climatol.*, **45**, 930–954, https://doi.org/10.1175/JAM2372.1.

Biggerstaff, M. I., and Coauthors, 2005: The shared mobile atmospheric research and teaching radar: A collaboration to enhance research and teaching. *Bull. Amer. Meteor. Soc.*, **86**, 1263–1274, https://doi.org/10.1175/bams-86-9-1263.

Bister, M., and K. A. Emanuel, 1997: The genesis of Hurricane Guillermo: TEXMEX analyses and a modeling study. *Mon. Wea. Rev.*, **125**, 2662–2682, https://doi.org/10.1175/1520-0493(1997)125%3C2662:TGOHGT%3E2.0.CO;2.

Bogner, P. B., G. M. Barnes, and J. L. Franklin, 2000: Conditional instability and shear for six hurricanes over the Atlantic Ocean. *Wea. Forecasting*, **15**, 192–207, https://doi.org/10.1175/1520-0434(2000)015%3C0192:CIASFS%3E2.0.CO;2.

Braun, S. A., M. T. Montgomery, and Z. Pu, 2006: High-resolution simulation of Hurricane Bonnie (1998). Part I: The organization of eyewall vertical motion. *J. Atmos. Sci.*, **63**, 19–42, https://doi.org/10.1175/jas3598.1.

Chen, S. S., J. A. Knaff, and F. D. Marks, 2006: Effects of vertical wind shear and storm motion on tropical cyclone rainfall asymmetries deduced from TRMM. *Mon. Wea. Rev.*, **134**, 3190–3208, https://doi.org/10.1175/MWR3245.1.

Chen, Y., and M. K. Yau, 2001a: Spiral bands in a simulated hurricane. Part I: Vortex Rossby wave verification. *J. Atmos. Sci.*, **58**, 2128–2145, https://doi.org/10.1175/1520-0469(2001)058⟨2128:sbiash⟩2.0.co;2.

Chen, Y., and M. K. Yau, 2003: Asymmetric structures in a simulated landfalling hurricane. *J. Atmos. Sci.*, **60**, 2294–2312, https://doi.org/10.1175/1520-0469(2003)060⟨2294:asiasl⟩2.0.co;2.

Corbosiero, K. L., J. Molinari, A. R. Aiyyer, and M. L. Black, 2006: The structure and evolution of Hurricane Elena (1985). Part II: Convective asymmetries and evidence for vortex Rossby waves. *Mon. Wea. Rev.*, **134**, 3073–3091, https://doi.org/10.1175/mwr3250.1.

Crum, T. D., and R. L. Alberty, 1993: The WSR-88D and the WSR-88D operational support facility. *Bull. Amer. Meteor. Soc.*, **74**, 1669–1688, https://doi.org/10.1175/1520-0477(1993)074%3C1669:TWATWO%3E2.0.CO;2.

DeMaria, M., and J. Kaplan, 1994: A statistical hurricane intensity prediction scheme (SHIPS) for the Atlantic basin. *Wea. Forecasting*, **9**, 209–220, https://doi.org/10.1175/1520-0434(1994)009%3C0209:ASHIPS%3E2.0.CO;2.

Didlake, A. C., and R. A. Houze, 2009: Convective-scale downdrafts in the principal rainband of Hurricane Katrina (2005). *Mon. Wea. Rev.*, **137**, 3269–3293, https://doi.org/10.1175/2009MWR2827.1.

Didlake, A. C., and R. A. Houze, 2013a: Convective-scale variations in the inner-core rainbands of a tropical cyclone. *J. Atmos. Sci.*, **70**, 504–523, https://doi.org/10.1175/JAS-D-12-0134.1.

Didlake, A. C., and R. A. Houze, 2013b: Dynamics of the stratiform sector of a tropical cyclone rainband. *J. Atmos. Sci.*, **70**, 1891–1911, https://doi.org/10.1175/JAS-D-12-0245.1.

Ditchek, S. D., K. L. Corbosiero, R. G. Fovell, and J. Molinari, 2020: Electrically active diurnal pulses in Hurricane Harvey (2017). *Mon. Wea. Rev.*, **148**, 2283–2305, https://doi.org/10.1175/MWR-D-20-0022.1.

Dong, L., and F. Zhang, 2016: OBEST: An observation-based ensemble subsetting technique for tropical cyclone track prediction. *Wea. Forecasting*, **31**, 57–70, https://doi.org/10.1175/WAF-D-15-0056.1.

Eastin, M. D., W. M. Gray, and P. G. Black, 2005: Buoyancy of convective vertical motions in the inner core of intense hurricanes. Part I: General statistics. *Mon. Wea. Rev.*, **133**, 188–208, https://doi.org/10.1175/MWR-2848.1.

Emanuel, K. A., 1986: An air-sea interaction theory for tropical cyclones. Part I: Steady-state maintenance. *J. Atmos. Sci.*, **43**, 585–605, https://doi.org/10.1175/1520-0469(1986)043%3C0585:AASITF%3E2.0.CO;2.

Goerss, J. S., 2000: Tropical cyclone track forecasts using an ensemble of dynamical models. *Mon. Wea. Rev.*, **128**, 1187–1193, https://doi.org/10.1175/1520-0493(2000)128%3C1187:TCTFUA%3E2.0.CO;2.

Gray, W. M., 1968: Global view of the origin of tropical disturbances and storms. *Mon. Wea. Rev.*, **96**, 669–700, https://doi.org/10.1175/1520-0493(1968)096%3C0669:GVOTOO%3E2.0.CO;2.

Griffin, J. S., R. W. Burpee, F. D. Marks Jr, and J. L. Franklin, 1992: Real-time airborne analysis of aircraft data supporting operational hurricane forecasting. *Wea. Forecasting*, **7**, 480–490, https://doi.org/10.1175/1520-0434(1992)007%3C0480:RTAAOA%3E2.0.CO;2.

Guimond, S. R., P. D. Reasor, G. M. Heymsfield, and M. M. McLinden, 2020: The dynamics of vortex Rossby waves and secondary eyewall development in Hurricane Matthew (2016): New insights from radar measurements. *J. Atmos. Sci.*, **77**, 2349–2374, https://doi.org/10.1175/jas-d-19-0284.1.

Guinn, T. A., and W. H. Schubert, 1993: Hurricane spiral bands. *J. Atmos. Sci.*, **50**, 3380–3403, https://doi.org/10.1175/1520-0469(1993)050⟨3380:hsb⟩2.0.co;2.

Helmus, J. J., and S. M. Collis, 2016: The Python ARM Radar Toolkit (Py-ART), a library for working with weather radar data in the Python programming language. *J. Open Res. Softw.*, **4**, https://doi.org/10.5334/jors.119.

Hence, D. A., and R. A. Houze, 2008: Kinematic structure of convective-scale elements in the rainbands of Hurricanes Katrina and Rita (2005). *J. Geophys. Res.*, **113**, https://doi.org/10.1029/2007jd009429.

Hence, D. A., and R. A. Houze, 2012: Vertical structure of tropical cyclone rainbands as seen by the TRMM Precipitation Radar. *J. Atmos. Sci.*, **69**, 2644–2661, https://doi.org/10.1175/JAS-D-11-0323.1.

Houze, R. A., 2010: Clouds in tropical cyclones. *Mon. Wea. Rev.*, **138**, 293–344, https://doi.org/10.1175/2009MWR2989.1.

Houze, R. A., F. D. Marks, and R. A. Black, 1992: Dual-aircraft investigation of the inner core of Hurricane Norbert. Part II: Mesoscale distribution of ice particles. *J. Atmos. Sci.*, **49**, 943–963, https://doi.org/10.1175/1520-0469(1992)049%3C0943:DAIOTI%3E2.0.CO;2.

Houze Jr, R. A., 1997: Stratiform precipitation in regions of convection: A meteorological paradox? *Bull. Amer. Meteor. Soc.*, **78**, 2179–2196, https://doi.org/10.1175/1520-0477(1997)078%3C2179:SPIROC%3E2.0.CO;2.

Jorgensen, D. P., 1984: Mesoscale and convective-scale characteristics of mature hurricanes. Part II. Inner core structure of Hurricane Allen (1980). *J. Atmos. Sci.*, **41**, 1287–1311, https://doi.org/10.1175/1520-0469(1984)041%3C1287:MACSCO%3E2.0.CO;2.

Kurihara, Y., and R. E. Tuleya, 1974: Structure of a tropical cyclone developed in a three-dimensional numerical simulation model. *J. Atmos. Sci.*, **31**, 893–919, https://doi.org/10.1175/1520-0469(1974)031%3C0893:SOATCD%3E2.0.CO;2.

Lee, W.-C., and F. D. Marks, 2000: Tropical cyclone kinematic structure retrieved from single-Doppler radar observations. Part II: The GBVTD-simplex center finding algorithm. *Mon. Wea. Rev.*, **128**, 1925–1936, https://doi.org/10.1175/1520-0493(2000)128⟨1925:tcksrf⟩2.0.co;2.

Li, Q., and Y. Wang, 2012a: Formation and quasi-periodic behavior of outer spiral rainbands in a numerically simulated tropical cyclone. *J. Atmos. Sci.*, **69**, 997–1020, https://doi.org/10.1175/2011JAS3690.1.

Li, Q., and Y. Wang, 2012b: A comparison of inner and outer spiral rainbands in a numerically simulated tropical cyclone. *Mon. Wea. Rev.*, **140**, 2782–2805, https://doi.org/10.1175/mwr-d-11-00237.1.

Li, Q., Y. Wang, and Y. Duan, 2017: A numerical study of outer rainband formation in a sheared tropical cyclone. *J. Atmos. Sci.*, **74**, 203–227, https://doi.org/10.1175/JAS-D-16-0123.1.

MacDonald, N. J., 1968: The evidence for the existence of Rossby-like waves in the hurricane vortex. *Tellus*, **20**, 138–150, https://doi.org/10.1111/j.2153-3490.1968.tb00358.x.

Marks, F. D., and R. A. Houze, 1987: Inner core structure of Hurricane Alicia from airborne Doppler radar observations. *J. Atmos. Sci.*, **44**, 1296–1317, https://doi.org/10.1175/1520-0469(1987)044%3C1296:ICSOHA%3E2.0.CO;2.

McBride, J. L., and R. Zehr, 1981: Observational analysis of tropical cyclone formation. Part II: Comparison of non-developing versus developing systems. *J. Atmos. Sci.*, **38**, 1132–1151, https://doi.org/10.1175/1520-0469(1981)038%3C1132:OAOTCF%3E2.0.CO;2.

McTaggart-Cowan, R., G. D. Deane, L. F. Bosart, C. A. Davis, and T. J. Galarneau, 2008: Climatology of tropical cyclogenesis in the North Atlantic (1948–2004). *Mon. Wea. Rev.*, **136**, 1284–1304, https://doi.org/10.1175/2007MWR2245.1.

Montgomery, M., M. Nicholls, T. Cram, and A. Saunders, 2006: A vortical hot tower route to tropical cyclogenesis. *J. Atmos. Sci.*, **63**, 355–386, https://doi.org/10.1175/JAS3604.1.

Montgomery, M. T., and R. J. Kallenbach, 1997: A theory for vortex rossby-waves and its application to spiral bands and intensity changes in hurricanes. *Quart. J. Roy. Meteor. Soc.*, **123**, 435–465, https://doi.org/10.1002/qj.49712353810.

Moon, Y., and D. S. Nolan, 2015: Spiral rainbands in a numerical simulation of Hurricane Bill (2009). Part II: Propagation of inner rainbands. *J. Atmos. Sci.*, **72**, 191–215, https://doi.org/10.1175/jas-d-14-0056.1.

Nguyen, L. T., J. Molinari, and D. Thomas, 2014: Evaluation of tropical cyclone center identification methods in numerical models. *Mon. Wea. Rev.*, **142**, 4326–4339, https://doi.org/10.1175/MWR-D-14-00044.1.

Oye, R., C. Mueller, and S. Smith, 1995: Software for radar translation, visualization, editing, and interpolation. *27th Conf. on Radar Meteorology*, Vail, CO, Amer. Meteor. Soc., 359–361.

Palmen, E., 1948: On the formation and structure of tropical hurricanes. *Geophys.*, **3**, 26–38.

Pasch, R. J., R. Berg, D. P. Roberts, and P. P. Papin, 2020: Hurricane Laura. AL132020, 1–75, https://www.nhc.noaa.gov/data/tcr/AL132020_Laura.pdf.

Pedregosa, F., and Coauthors, 2011: Scikit-learn: Machine Learning in Python. *J. Mach. Learn. Res.*, **12**, 2825–2830.

Potvin, C. K., A. Shapiro, and M. Xue, 2012: Impact of a vertical vorticity constraint in variational dual-Doppler wind analysis: Tests with real and simulated supercell data. *J. Atmos. Oceanic Technol.*, **29**, 32–49, https://doi.org/10.1175/JTECH-D-11-00019.1.

Powell, M. D., 1990: Boundary layer structure and dynamics in outer hurricane rainbands. Part I: Mesoscale rainfall and kinematic structure. *Mon. Wea. Rev.*, **118**, 891–917, https://doi.org/10.1175/1520-0493(1990)118⟨0891:blsadi⟩2.0.co;2.

Rappaport, E. N., 2014: Fatalities in the United States from Atlantic tropical cyclones: New data and interpretation. *Bull. Amer. Meteor. Soc.*, **95**, 341–346, https://doi.org/10.1175/BAMS-D-12-00074.1.

Reasor, P. D., M. T. Montgomery, F. D. Marks, and J. F. Gamache, 2000: Low-wavenumber structure and evolution of the hurricane inner core observed by airborne dual-Doppler radar. *Mon. Wea. Rev.*, **128**, 1653–1680, https://doi.org/10.1175/1520-0493(2000)128⟨1653:lwsaeo⟩2.0.co;2.

Ringnér, M., 2008: What is principal component analysis? *Nat. Biotechnol.*, **26**, 303–304.

Roundy, P. E., 2015: On the interpretation of EOF analysis of ENSO, atmospheric Kelvin waves, and the MJO. *J. Climate*, **28**, 1148–1165, https://doi.org/10.1175/JCLI-D-14-00398.1.

Sawada, M., and T. Iwasaki, 2010a: Impacts of evaporation from raindrops on tropical cyclones. Part I: Evolution and axisymmetric structure. *J. Atmos. Sci.*, **67**, 71–83, https://doi.org/10.1175/2009JAS3040.1.

Sawada, M., and T. Iwasaki, 2010b: Impacts of evaporation from raindrops on tropical cyclones. Part II: Features of rainbands and asymmetric structure. *J. Atmos. Sci.*, **67**, 84–96, https://doi.org/10.1175/2009JAS3195.1.

Shapiro, A., K. M. Willingham, and C. K. Potvin, 2010: Spatially variable advection correction of radar data. Part I: Theoretical considerations. *J. Atmos. Sci.*, **67**, 3445–3456, https://doi.org/10.1175/2010jas3465.1.

Sibson, R., 1981: A brief description of natural neighbour interpolation. *Interpreting multivariate data*, 21–36.

Smull, B. F., and R. A. Houze Jr, 1985: A midlatitude squall line with a trailing region of stratiform rain: Radar and satellite observations. *Mon. Wea. Rev.*, **113**, 117–133, https://doi.org/10.1175/1520-0493(1985)113%3C0117:AMSLWA%3E2.0.CO;2.

Steiner, M., R. A. Houze Jr, and S. E. Yuter, 1995: Climatological characterization of three-dimensional storm structure from operational radar and rain gauge data. *J. Appl. Meteor. Climatol.*, **34**, 1978–2007, https://doi.org/10.1175/1520-0450(1995)034%3C1978:CCOTDS%3E2.0.CO;2.

Wang, Y., 2002a: Vortex Rossby waves in a numerically simulated tropical cyclone. Part I: Overall structure, potential vorticity, and kinetic energy budgets. *J. Atmos. Sci.*, **59**, 1213–1238, https://doi.org/10.1175/1520-0469(2002)059⟨1213:vrwian⟩2.0.co;2.

Wang, Y., 2002b: Vortex Rossby waves in a numerically simulated tropical cyclone. Part II: The role in tropical cyclone structure and intensity changes. *J. Atmos. Sci.*, **59**, 1239–1262, https://doi.org/10.1175/1520-0469(2002)059⟨1239:vrwian⟩2.0.co;2.

Wang, Y., 2009: How do outer spiral rainbands affect tropical cyclone structure and intensity? *J. Atmos. Sci.*, **66**, 1250–1273, https://doi.org/10.1175/2008JAS2737.1.

Wilks, D. S., 2011: Principal component (EOF) analysis. *International Geophysics*, Vol. 100, Elsevier, 519–562.

Willoughby, H., 1998: Tropical cyclone eye thermodynamics. *Mon. Wea. Rev.*, **126**, 3053–3067, https://doi.org/10.1175/1520-0493(1998)126%3C3053:TCET%3E2.0.CO;2.

Willoughby, H. E., 1988: The dynamics of the tropical cyclone core. *Aust. Meteor. Mag.*, **36**, 183–191.

Willoughby, H. E., and M. B. Chelmow, 1982: Objective determination of hurricane tracks from aircraft observations. *Mon. Wea. Rev.*, **110**, 1298–1305, https://doi.org/10.1175/1520-0493(1982)110%3C1298:ODOHTF%3E2.0.CO;2.

You, Y., and J. C. Furtado, 2017: The role of South Pacific atmospheric variability in the development of different types of ENSO. *Geophys. Res. Lett.*, **44**, 7438–7446, https://doi.org/10.1002/2017GL073475.

Yuter, S. E., and R. A. Houze, 1997: Measurements of raindrop size distributions over the Pacific warm pool and implications for Z–R relations. *J. Appl. Meteor. Climatol.*, **36**, 847–867, https://doi.org/10.1175/1520-0450(1997)036%3C0847:MORSDO%3E2.0.CO;2.

Yuter, S. E., R. A. Houze, E. A. Smith, T. T. Wilheit, and E. Zipser, 2005: Physical characterization of tropical oceanic convection observed in KWAJEX. *J. Appl. Meteor. Climatol.*, **44**, 385–415, https://doi.org/10.1175/JAM2206.1.

Zhang, J. A., R. F. Rogers, D. S. Nolan, and F. D. Marks, 2011: On the characteristic height scales of the hurricane boundary layer. *Mon. Wea. Rev.*, **139**, 2523–2535, https://doi.org/10.1175/MWR-D-10-05017.1.

Zipser, E. J., 2003: Some views on "hot towers" after 50 years of tropical field programs and two years of TRMM data. *Cloud Systems, Hurricanes, and the Tropical Rainfall Measuring Mission (TRMM)–A Tribute to Dr. Joanne Simpson, Meteor. Monogr.*, **29**, 49–58, https://doi.org/10.1175/0065-9401(2003)029%3C0049:CSVOHT%3E2.0.CO;2.